Optimization and Application of Chemical Exchange Saturation Transfer Imaging

by

Zhuozhi Dai

A thesis submitted in partial fulfillment of the requirements for the degree of

Doctor of Philosophy

Medical Sciences - Shantou Biomedical Engineering
University of Alberta

Abstract

Magnetic resonance imaging (MRI) is a non-invasive method that can provide detailed anatomic images and has been widespread in clinical application. Novel MRI techniques are emerging from the development of MR theory and hardware. Among them, chemical exchange saturation transfer (CEST) provides a means to noninvasively measure a range of in-vivo metabolic and chemical biomarkers. By measuring the water signal and looking at indirect saturation by exchangeable protons, this new technique may provide valuable diagnostic information and early indicators of treatment effectiveness.

Because CEST imaging is sensitive to dilute CEST agents, local pH, and temperature, it can be applied in many different ways. Indeed, CEST MRI has been shown capable of detecting a host of biomolecules including glutamate, glycogen, glucose, and gene expression as well as pH and temperature, complementing conventional MRI, which is mainly structural. Compared with magnetic resonance spectroscopy, CEST has higher spatial resolution and superior sensitivity. The applications to disease are still being exploration. Moreover, current CEST techniques are varied and sometimes hardware incompatible. In this thesis, we addressed some of these problems, and applied our methods to animal models at Shantou University using 7.0T MRI and human brain at the University of Alberta using 4.7T and 3.0T MRI. The overall hypothesis is that CEST sequences can be optimized under standard criteria and improved CEST methods may provide noninvasive measures of pH, glutamate and intracellular protein in animal models and in human brain.

The thesis contains three major projects, including sequence development and optimization at 7T (Chapter 2), animal studies at 7T (Chapter 3), and human application at 3T (Chapter 4). A brief introduction of CEST will be presented in Chapter 1. A smaller project on pH imaging in CEST, including pH weighted imaging in a diabetic stroke model, and quantitative pH imaging, was compressed into another independent chapter (Chapter 5).

In project 1 (sequence development and optimization at 7T), we proposed a magnetization transfer (MT) prepared gradient echo (GRE) MRI sequence for CEST imaging. Routine CEST MRI includes a long RF saturation pulse followed by fast image readout, which is associated with high specific absorption rate and limited spatial resolution. In addition, echo planar imaging (EPI)-based fast image readout is prone to image distortion, particularly severe at high field. To address these limitations, we evaluated MT prepared GRE MRI for CEST imaging. We proved the feasibility using numerical simulations and experiments in vitro and in vivo. We then optimized the sequence and further demonstrated endogenous amide proton CEST imaging in rat brains that underwent permanent middle cerebral artery occlusion.

In project 2, we applied glutamate imaging in schizophrenia models at 7T, which may provide a powerful indicator of the diagnosis of schizophrenia prodrome. In this project, we examined glutamate variation in different brain regions in an early schizophrenia model using glutamate CEST imaging. Our results proved that the signal intensity of glutamate image was strictly related to glutamate concentration, and that other neuro metabolites contribute negligible

glutamate CEST effects except GABA. Compared to healthy controls, glutamate signals of schizophrenic models increased in the whole brain, especially in cerebral cortex, hippocampus, and thalamus. In addition, glutamate CEST image has excellent correlation with glutamate measured by spectroscopy.

In project 3, we detected changes of Amide Proton Transfer (APT) in the motor cortex and corticospinal tract of amyotrophic lateral sclerosis (ALS) patients, which has the potential to be an objective imaging biomarker for ALS diagnosis. There is a lack of objective imaging indicators for ALS diagnosis. This study aimed to explore the value of APT in ALS patients and the correlation between APT and diffusion tensor imaging (DTI). Compared with healthy controls, the APT signal intensities in ALS were significantly reduced in motor cortex and corticospinal tract, which was undetectable under routine imaging methods. In addition, APT was negatively correlated with FA and positively correlated with ADC. The combination of APT and DTI can simultaneously detect changes of metabolism and microstructure in ALS patients.

In summary, developments in CEST imaging have been made including sequence development, post processing, animal studies, and clinical translation to human subjects using a wide range of MRI strengths from 3T to 7T. The results make valuable contributions to the growing field of CEST imaging.

Preface

This thesis is an original work by Zhuozhi Dai. The second chapter of this thesis has been published: Dai Z, Ji J, Xiao G, Yan G, Li S, Zhang G, Lin Y, Shen Z, Wu R. Magnetization Transfer Prepared Gradient Echo MRI for CEST Imaging. PloS one. 2014;9(11):e112219. The method and writing were carried out by the author. Some of the research conducted for this thesis forms part of an international research collaboration, led by Professor Renhua Wu at the Shantou University Medical College, with Professor Alan H. Wilman being the lead collaborator at the University of Alberta.

The MRI method and data analysis referred to in chapter 2-5 were designed by the author, with the assistance of Professor Gen Yan, Professor Gang Xiao, Zhiwei Shen, Thomas MacIntyre, Jean-David Jutras, and Kelly McPhee. The sequence in chapter 4 was originally created by Professor Mark D Pagel and Edward A. Randtke. Chapter 4 is also a collaborative work, the patients and volunteers were recruited by Professor Sanjay Kalra, Dennell Mah and Peter Seres. The fifth chapter of this thesis is adapted from two published ISMRM abstracts: “Zhuozhi Dai , Phillip Zhe Sun , Gang Xiao , Gen Yan , Yanlong Jia , Zhiwei Shen , Alan H. Wilman , and Renhua Wu. Quantitative pH using chemical exchange saturation transfer and phosphorous spectroscopy. ISMRM 2016.” and “Zhuozhi Dai, Yanlong Jia, Gen Yan, Fei Duan, Gang Xiao, Zhiwei Shen, Hongfu Sun, Alan H. Wilman, and Renhua Wu, pH-weighted imaging in diabetes mellitus suffering acute cerebral ischemic stroke, ISMRM 2015.”

Of all the papers published, accepted and submitted, Professor Alan Wilman and Professor Renhua Wu shared unique ideas, helpful discussion and careful editing of the manuscripts. Ethical approvals were granted for all the in vivo and in situ experiments performed.

Acknowledgments

Grateful acknowledgment is made to Li Ka Shing Sino-Canadian Exchange Program, Li Ka Shing Foundation. This study was supported in part by grants from Canadian Institutes of Health, the ALS Society of Canada and Brain Canada, the Natural Science Foundation of China (NSFC 81471730, 31870981), MSF of Guangdong Province (B2013281), and the Natural Science Foundation of Guangdong Province (2018A030307057).

Table of contents

Contents

List of Figures

List of Tables

Chapter 1

Introduction

1.1 Overview

This thesis introductory chapter assumes that the reader already has a good understanding of magnetic resonance imaging (MRI). Only a very brief introduction to basic nuclear magnetic resonance (NMR) will be provided. The introduction will then focus on chemical exchange saturation transfer (CEST) imaging methods and applications, which make up the bulk of the thesis chapters.

Since the inception of MRI in the 1970s, it has grown into a versatile medical imaging technique in clinical application and basic research. MRI is a medical imaging technique that uses a magnetic field and radio waves to probe the anatomy and physiological processes in both health and disease. Advantages of MRI include that it is non-invasive, does not use ionizing radiation and has many contrast sensitivities. MRI is used extensively across the body and especially for the central nervous system (brain and spine).

Nikola Tesla, whose name has been honored with the unit of magnetic field strength, discovered the Rotating Magnetic Field in 1882. Then in 1973, Paul Lauterbur produced the first NMR image. After that, MRI has been exponentially increasing in medical use. There have been four

related Nobel Prizes in this field so far, beginning with Isidor I. Rabi in 1937 who observed the quantum phenomenon dubbed nuclear magnetic resonance. Later Nobel Prizes included: Felix Bloch + Edward Mills Purcell (1952, NMR development); Richard Ernst (1991, NMR spectroscopy); Lauterbur + Mansfield (2003, MRI development). The delay between the discovery of MRI in 1973 and the Nobel prize in 2003, illustrates that many contributors have played roles.

In one paragraph we give a brief classical description of the physics of MRI. In zero magnetic field, the hydrogen nuclei in the body are randomly oriented and produce no net magnetization. In the presence of a static magnetic field, some of the nuclei align with and some against the field. The imbalance in alignment, due to a difference in population for the different energy levels, leads to a net magnetization. The protons precess at a specific frequency called the Larmor frequency, which is determined by the gyro-magnetic ratio and the strength of the magnetic field. When an external radio frequency pulse is applied at the resonant frequency, the energy state of the protons will be changed, which is called excitation. If the frequency of this pulse is exactly at the Larmor frequency, it is called “on-resonance,” while “off-resonance” excitation means the frequency is far from the Larmor frequency. After excitation, the rotating magnetization produces an oscillating magnetic field that will induce a small current in the receiver coil that can be detected as measurable signal. At the same time, the protons will recover from the higher energy state back to the equilibrium state. These phenomena are described by relaxation, decomposed into longitudinal and transverse components in the orthogonal system. By introducing additional gradient magnetic fields and repeated experiments, magnetic resonance images can be reconstructed using the Fourier transform. Different types of MRI

sequences may be performed largely by varying the magnetic field gradients, the radiofrequency pulses and the timings. One of these methods is the CEST method to be studied.

Novel MRI techniques are emerging from the development of MR theory and hardware. Among them, CEST provides a means to noninvasively measure a range of in-vivo metabolic and chemical biomarkers. Chemical exchange represents the transfer of a nucleus from one molecular environment to another. Chemical exchange saturation transfer was first proposed by KM Ward et al. in 2000 (1). In 2003, Zhou et al first reported the amide proton transfer imaging, a sensitive diamagnetic chemical exchange saturation transfer technique capable of detecting pH (2, 3). In 2012, glutamate CEST was introduced by Cai et al (4). Other applications such as Glucose CEST (5), Myo-inositol CEST (6), γ-aminobutyric acid CEST (7), and paramagnetic CEST (8, 9) were also reported in recent years. Different CEST techniques are distinguished by different saturation frequencies and various scanning parameters.

Although metabolic information can also be obtained with MR Spectroscopy (MRS), it is limited by low metabolite concentrations. Instead, CEST measures the water signal and is sensitive to indirect saturation by exchangeable protons. This new area may provide valuable diagnostic information and early indicators of treatment effectiveness. However, current CEST techniques in use are varied, and evaluations need to be performed to determine the best methods. Moreover, the applications of CEST techniques are under exploited. In this program, we will address some of these problems that have potential to profoundly impact the field of CEST and apply our

methods to animal models at Shantou University using 7.0T MRI and human brain at University of Alberta using 4.7T and 3.0T MRI.

1.2 Theory of CEST

To understand CEST imaging in general, we can know the basic principles from its name, which contains two parts: chemical exchange and saturation transfer. Chemical exchange represents the transfer of a nucleus from one molecular environment to another, while saturation transfer means that the transfer carrier pool is saturated, which means its magnetization is destroyed. In this section, the theory of CEST is described, including magnetization, Bloch equations, and the classical analytical solution.

1.2.1 Magnetization

Magnetization is the vector field that represented the averaged angular momenta from all spins within a region. In MRI, the magnetization can be decomposed into longitudinal and transverse magnetization, with longitudinal aligning with the main magnetic field and transverse being perpendicular to the main field. The recovery of longitudinal magnetization (M_z) is due to spin-lattice interaction, while the decay of transverse magnetization (M_x and M_y) is due to spin-spin interaction. In order to describe how fast the magnetization returns to its equilibrium state, two constants r_1 and r_2 are introduced. Specifically, r_1 is the rate to reduce the difference

between the longitudinal magnetization and its equilibrium value by a factor of e. r_2 is the rate to reduce the transverse magnetization by a factor of e.

1.2.2 Bloch equations

Bloch equations are a set of equations that are used to calculate the magnetization as a function of time in the presence of external field effects. Without chemical exchange, the magnetization system can be described as follow:

$$\frac{dM_x}{dt} = -r_2 M_x + \Delta\omega M_y$$

$$\frac{dM_y}{dt} = -\Delta\omega M_x - r_2 M_y + \omega_1 M_z$$

$$\frac{dM_z}{dt} = -\omega_1 M_y - r_1 M_z + r_1 M_0$$

In which $\Delta\omega$ is the difference between Larmor frequency (ω_0) and the saturation frequency (ω), r_1 and r_2 are the longitudinal and transverse relaxation constant.

For a chemical exchange saturation transfer system, a simple 2-pool model can be used, including a bulk water pool (w) and a dilute labile proton pool (s)(10). This dilute proton pool is invisible in routine MRI because it has a very short T2 time constant and low concentration. However, because of the existence of chemical exchange, the protons in high energy state can transfer between these two pools. Based on this phenomenon, we can image specific components

that have chemical exchange effect indirectly by the water pool. Moreover, the signal is amplified since the huge contrast of concentration between pool w and pool s. The magnetization of each pool follows the rule of the Bloch equations. Due to the existence of the chemical exchange, we add exchange terms to describe the magnetization exchange, as listed below.

$$\frac{dM_{xs}}{dt} = -r_{2s}M_{xs} - \Delta\omega_s M_{ys} + k_{ws}M_{xw} - k_{sw}M_{xs}$$

$$\frac{dM_{ys}}{dt} = \Delta\omega_s M_{xs} - r_{2s}M_{ys} + \omega_1 M_{zs} + k_{ws}M_{yw} - k_{sw}M_{ys}$$

$$\frac{dM_{zs}}{dt} = -\omega_1 M_{ys} - r_{1s}M_{zs} + r_{1s}M_{0s} + k_{ws}M_{zw} - k_{sw}M_{zs}$$

$$\frac{dM_{xw}}{dt} = -r_{2w}M_{xw} + \Delta\omega_w M_{yw} + k_{sw}M_{xs} - k_{ws}M_{xw}$$

$$\frac{dM_{yw}}{dt} = \Delta\omega_w M_{xw} - r_{2w}M_{yw} + \omega_1 M_{zw} + k_{sw}M_{ys} - k_{ws}M_{yw}$$

$$\frac{dM_{zw}}{dt} = -\omega_1 M_{yw} - r_{1w}M_{zw} + r_{1w}M_{0w} + k_{sw}M_{zs} - k_{ws}M_{zw}$$

The term k_{ws} is the chemical exchange rate from bulk water pool (w) to dilute labile proton pool (s), and k_{sw} is the rate of opposite exchange.

1.2.3 Classical analytical solution

To simplify and quantify these Bloch equations, Zhou et al proposed several reasonable assumptions(10, 11). First, a steady state is reached instantly, in this case, the changes of the

magnetizations are zero. Second, the saturation is applied to pool s only, with bulk water protons unperturbed. Thus, the magnetization in the x-direction can be ignored since it will not disturb the magnetization in other direction. With these two assumptions, one can calculate the magnetization in the z-direction of pool s (m_{zs}). Then the dynamics for the water pool can be described as

$$\frac{dm_{zw}}{dt} = -r'_{1w}m_{zw} + k_{sw}m_{zs}$$

Where $r'_{1w} = r_{1w} + k_{ws}$, $m_{zw} = M_{zw} - M_{0w}$, M_{0w} is the equilibrium magnetization of water. Therefore, after solving the above equation, one has

$$m_{zw}(t) = \frac{k_{sw}m_{zs}}{r'_{1w}}[1 - e^{-r'_{1w}(t-t0)}]$$

Then the signal intensity of the water pool $M_{zw}(t)$ can be calculated. We usually use the proton exchange rate (PTR) to represent the CEST effect, where

$$PTR = 1 - \frac{M_{zw}(t)}{M_{0w}}$$

1.2.4 The steady-state and field strength

Steady-state is an unvarying condition in the exchange process. It is an important assumption for the solution of the Bloch equations. In order to reach steady-state, the exchange rate should be higher than the T1 relaxation rate. Moreover, the exchange rate should simultaneously be lower than the frequency difference between the exchangeable proton and water hydrogen protons. Otherwise, direct water saturation will occur when applying the saturation. Therefore, the CEST

effect is dependent on the magnetic field strength. Higher field strengths have greater chemical shift difference between the exchangeable proton and water hydrogen protons, and thus allow for higher exchange rates to reach steady state. It is particularly crucial for diamagnetic CEST, which has the saturation frequency close to water protons.

1.3 Sequence development

The CEST sequence is not a standard sequence configuration currently available on standard MRI scanners. Various CEST sequences have been created. In general, the sequences can be thought to be composed of two parts: saturation preparation and data acquisition. Saturation preparation contains a long, off-resonant pulse with the primary purpose to saturate the dilute protons and bring the 2-pool system into a steady state. The saturation pulse can be continuous wave or pulse wave. In this section, we will review CEST sequences in three categories, including continuous wave sequences, pulse wave sequences, and others.

1.3.1 Continuous wave sequence

The earliest CEST sequence is the spin echo (SE) sequence with continuous wave saturation before each segment of *k*-space acquisition (1). This standard SE CEST sequence ensures a stable CEST effect, but it is very time consuming, needing tens of minutes to obtain a full z

spectrum. To reduce scan time, fast acquisition methods can be used to obtain the whole *k*-space data in one shot after pre-saturation.

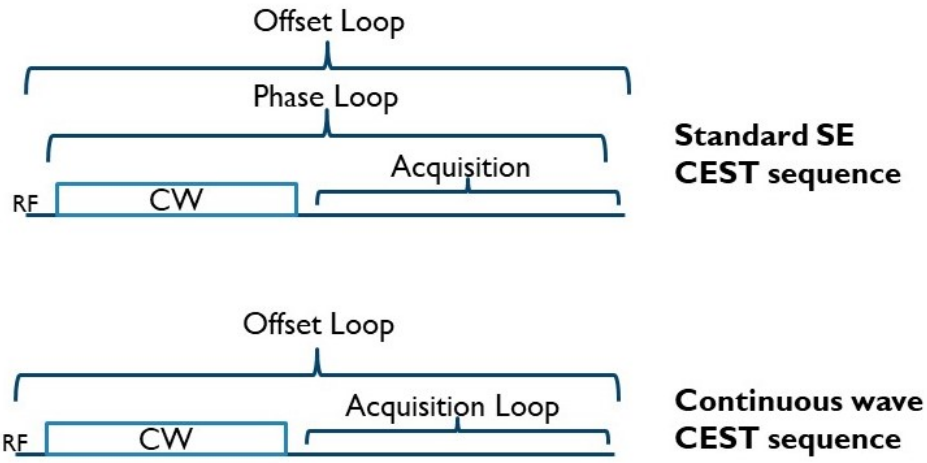

Figure 1. 1 The schematic of standard spin echo (SE) CEST sequence and other continuous wave (CW) CEST sequences. Standard SE CEST sequence use continuous wave for pre-saturation before each track of the k space. Pre-saturation should be applied repeatedly during phase encoding. For continuous wave CEST sequence, fast acquiring methods are used to obtain the whole k space data in one shot following saturation.

Continuous wave saturation has higher specificity and is easy to optimize for quantitative parameters, but there are hardware limitations and RF heating problems, which hinder the application in the human body. Therefore, most continuous wave CEST sequences are conducted in animal or phantom experiments. Schröder et al demonstrated a high-sensitivity, and high-contrast molecular imaging technique by exploiting xenon biosensors (12). Togao et al revealed that continuous wave APT imaging has the potential to provide a characterization test to

differentiate types or grade of lung cancer noninvasively, which may eventually reduce the need for invasive needle biopsy or resection for lung cancer (13). Later, Kunth et al further optimized the saturation amplitude and width of hyperpolarized Xe with chemical exchange saturation transfer and found an optimal saturation pulse strength corresponding to $\sqrt{2}$ times the Xe exchange rate (14).

1.3.2 Pulse wave sequence

The pulse wave sequence is effective in reducing the RF heating problem that arises with continuous wave methods, although it sacrifices simple quantification. More importantly, the pulse wave sequence is more compatible with the hardware constraints on clinical scanners such as duty cycle. Pulse wave sequences contain a series of shaped RF pulses and interleaves with delays and crusher gradients to eliminate spurious signals. Therefore, some parameters such as pulse shape, pulse flip angle and duty cycle need to be optimized.

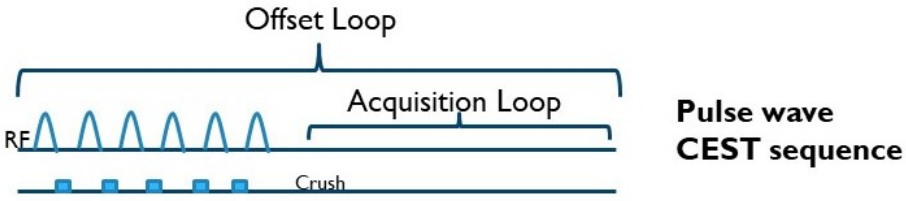

Figure 1. 2 The schematic of pulse wave (PW) CEST sequences. For pulse wave CEST sequence, pulse wave pre-saturation is used instead of continuous wave. The advantage of it is the proper duty cycle can reduce the specific absorption rate.

Sun et al found maximally obtainable pulsed CEST contrast is approximately 95% of CW CEST contrast, and their optimal RF irradiation powers are equal once take the duty cycle into account (15). Zu et al used an optimized pulsed CEST sequence and demonstrated that an irradiation flip angle of 180° is optimal or near optimal, independent of the other acquisition parameters and the sample properties. Moreover, higher duty cycles yield higher CEST contrast in pulsed CEST (16). Schmitt et al evaluated saturation efficiency of trains of Gaussian-shaped radiofrequency pulses at field strengths of 1.5T, 3T, and 7T and proved that the proposed saturation pulse train does not require hardware modifications, offers low specific absorption rate, and can be used in a standard clinical setup (17). Therefore, most clinical applications have used a pulse wave CEST sequence.

1.3.3 Comparison of CEST sequences

By introducing the signal to noise ratio (SNR) criteria for CEST images, one can compare the pros and cons of the sequences. The algorithm to calculate SNR of CEST was proposed by Sun et al (18).

$$SNR_{CESTR} = \frac{CESTR}{\sigma_{CESTR}} = \frac{CESTR}{\sqrt{2+CESTR^2}} \cdot \frac{I_0}{\sigma} = \frac{CESTR}{\sqrt{2+CESTR^2}} \cdot SNR_{I_0}$$

where CESTR is the CEST effect calculated by asymmetry analysis (see section 1.4.2), σ is the standard deviation, I_0 is the unsaturated image at thermal-equilibrium state (see details in post-processing section).

CEST images were obtained from iopamidol, a clinically approved X-ray contrast agent which can exhibit CEST effect at 4.2 ppm and 5.5 ppm (19). The formula of iopamidol is $C_{17}H_{22}I_3N_3O_8$ with molecular weight of 777.08 g/mol. We compared the CEST effect at 4.2 ppm using different CEST sequences (similar results at 5.5 ppm) and found the continuous wave (CW) pre-saturation is superior to pulse wave (PW) pre-saturation under the same acquisition time, the contrast of SNR_{CEST} is about 36 percent (Figure 1-4). However, we can only use pulse wave pre-saturation in human applications because of the RF heating limits. In pulse wave sequences, the highest SNR appeared in gradient echo.

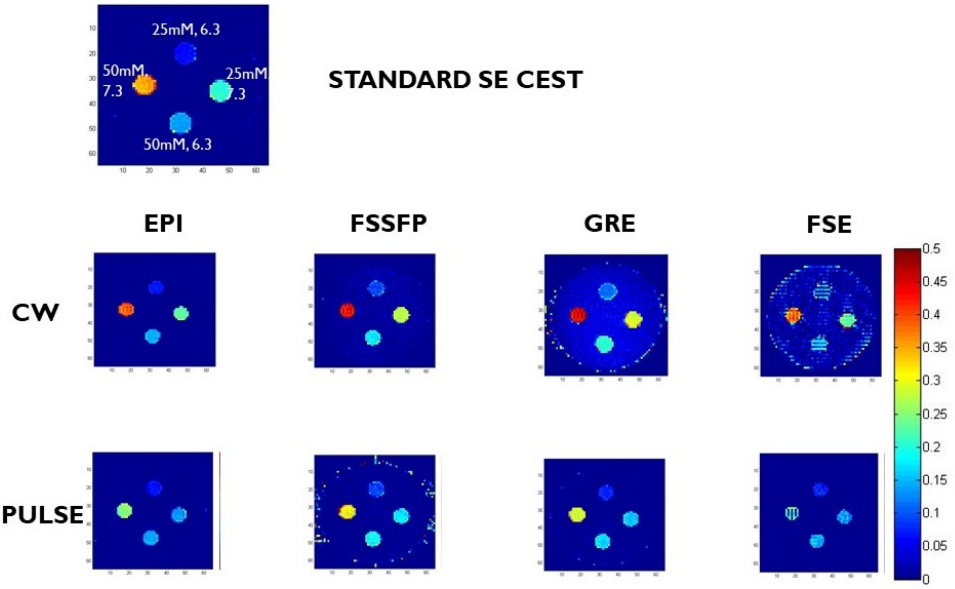

Figure 1. 3 *CEST images were obtained from iopamidol with different concentrations (25mM and 50 mM) and pH values (6.3 and 7.3). The CEST effect were shown at 4.2 ppm (similar results at 5.5 ppm) in different CEST sequences, including echo planar imaging (EPI), steady-state free precession (FSSFP), gradient echo (GRE), fast spin echo (FSE) and spin echo (SE) both with continuous wave (CW) and pulse wave (PW) pre-saturation. The signal intensities of CW pre-saturation sequence were superior to those of PW.*

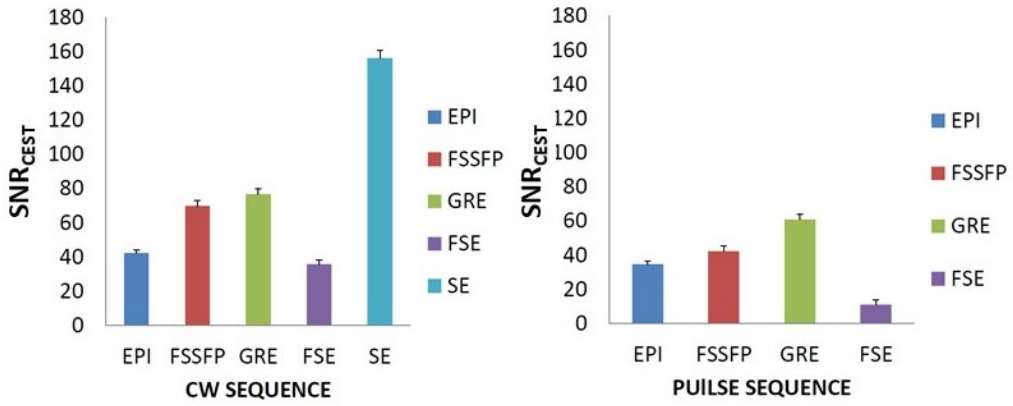

Figure 1. 4 *showed the SNRcest in different sequences. In CW sequences, we could see the standard spin echo (SE) sequence has the highest signal to noise ratio, followed by continuous wave gradient echo. In pulse sequences, the highest SNR appeared in gradient echo.*

1.3.4 Other sequences

Alternative sequences to obtain CEST effects have also been introduced. Zu et al introduced a new sequence called Chemical exchange rotation transfer (CERT) and demonstrated it provides an image contrast that is more specific to chemical exchange than conventional CEST by means of asymmetric Z-spectrum analysis (20-22). Another sequence called saturation with frequency alternating RF irradiation (SAFARI) that is robust against B0 inhomogeneities was proposed by Scheidegger et al (23). This method employed dual frequency saturation in combination with standard CEST saturation and proved to successfully suppress MT asymmetry effects as well as the influence of B0 inhomogeneities. In order to reduce scanning time, an ultrafast CEST sequence was proposed by Xu et al, which applies a gradient during irradiation to saturate

different frequency offsets at different spatial positions (24, 25). However, this technique requires a perfect B0 homogeneity and only applies in phantom experiments. Other similar sequences such as chemical exchange-sensitive spin-lock (CESL)(26), frequency labeled exchange (FLEX) (27), etc. are beyond the scope of this thesis.

1.4 Post-processing

Post-processing is critical in CEST experiments. Since it is a novel technique, no standard processing is supplied on clinical systems. Different research groups and companies have their own processing methods to interpret the CEST data. In this section, the essential parts of CEST post-processing are discussed.

1.4.1 Z-spectrum

The Z-spectrum contains almost all information required for CEST. To obtain the Z-spectrum, a series of images need to be acquired at different offset frequencies. Then the images will be normalized by an unsaturated image (S0) to reduce the T1 effect. The spectrum plot with saturation frequency (ppm) as the abscissa and normalized signal as the ordinate is called the Z-spectrum. In this spectrum, the water frequency is assigned to be 0 ppm. We can see the CEST effect at a specific frequency, such as the amide peak at 3.5 ppm. However, the biggest peak is

the water direct saturation around 0 ppm, which may interfere with the detection of the CEST effect. Therefore, the next processing method is needed to reduce this contamination.

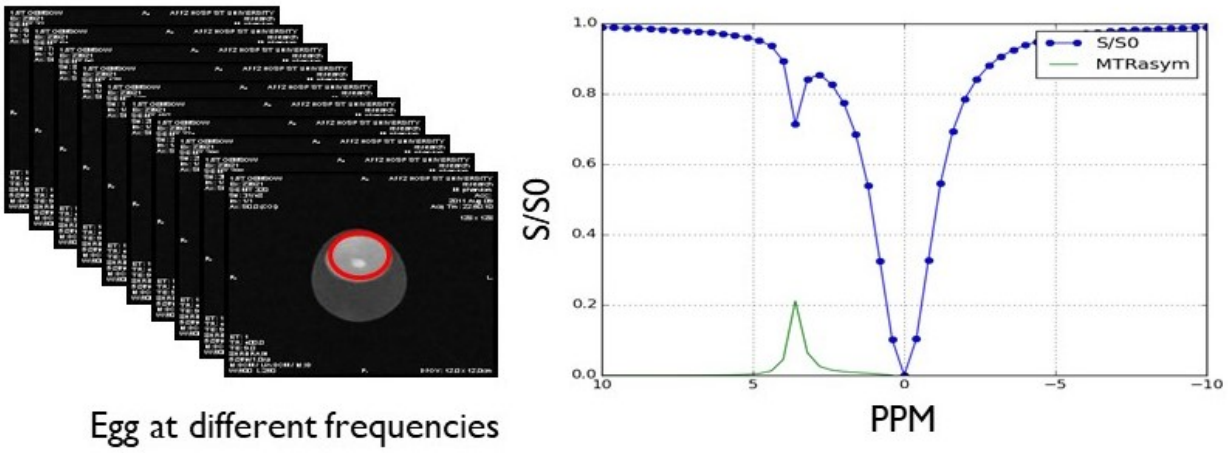

Figure 1. 5 *Raw data of CEST images (left) and the Z-spectrum (right). A clear CEST effect at 3.5 ppm was presented in the Z-spectrum using the saturation power of 1μT and saturation time of 4s.*

1.4.2 Magnetization transfer ratio asymmetry analysis

In order to reduce water direct saturation effect and traditional magnetization transfer (MT) effect, the magnetization transfer ratio asymmetry analysis (MTRasym) was introduced. Assuming these two effects are symmetric around the water frequency, they can be eliminated using the following equation.

$$\text{MTRasym} = \frac{S(ref) - S(sat)}{S0}$$

In which S(sat) is the image with saturation frequency at the CEST target, S(ref) is the image with saturation frequency at the opposite site of water, S0 is the image without saturation.

The MTR asymmetry analysis is commonly used in CEST experiments and works well in phantoms and simple systems (Figure 1.6). However, negative MTRasym is often observed in brain studies, presumably due to the underlying MT and NOE effects. The MT effect was reported to be asymmetric in the brain in previous studies (28). Another inherent assumption of MTRasym is the negligible contribution of other exchangeable pools. Another inherent assumption of MTRasym is the negligible contribution of other exchangeable pools, which is hardly accomplished in vivo. Therefore, more elaborate approaches are needed to further interpret the CEST effect.

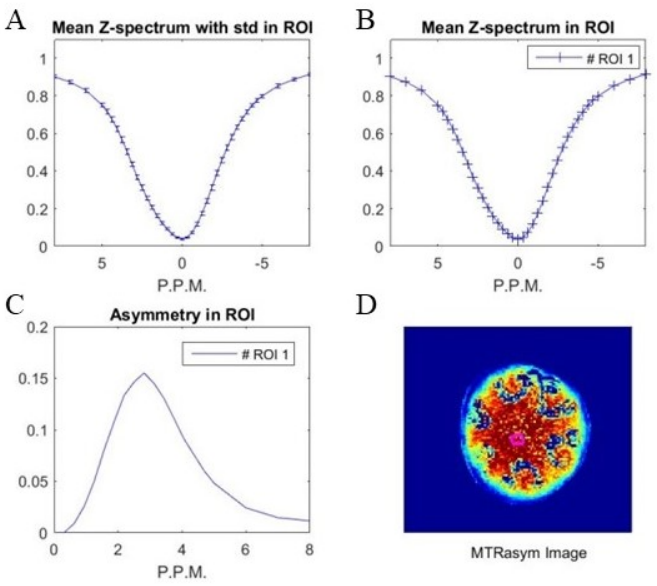

Figure 1. 6 *shows the Z spectrum and MTR asymmetry in the watermelon. A is the Z spectrum of mean value with standard deviation. B is the Z spectrum of mean value. C is the MTRasym result. D is the raw image of the watermelon. The CEST effect of watermelon is about 15 percent.*

1.4.3 Lorentz fitting

Recent studies prefer to use the fitting of Lorentzian lines to represent the CEST effect since the in vivo CEST data always contains multiple exchanging pools. In order to separate the CEST effect of each pool in the Z spectrum, each can be modeled with a Lorentzian line. Under steady state saturation, the Lorentzian line shape model can offer access to the ideal CEST feature (29). Therefore, if we know the approximate location of each pool, amplitude, and width, we can fit the CEST effect of each compound. Further research proved that the Z-spectrum could be fitted as a sum of four Lorentzian functions in vivo representing water, amide, amine, and nuclear Overhauser effect (NOE) peaks (30). Cai et al applied Lorentzian fitting to characterize the

multiple exchangeable components from an intracranial tumor mode and identified the 2ppm peak decreased with tumor progression(31).

Compared to MTR asymmetric analysis, the Lorentz fitting can isolate each exchangeable pool and minimize the interference in a system with multiple exchange pools. It can also separate the contribution from the MT asymmetry that contaminates the conventional MTR asymmetric analysis in vivo. Our result shows the Lorentzian fitting can identify five different peaks in the human brain, including water, MT, amide, amine, and NOE peaks. These peaks are considered to be the main contributors in the Z spectrum in the brain in low saturation power.

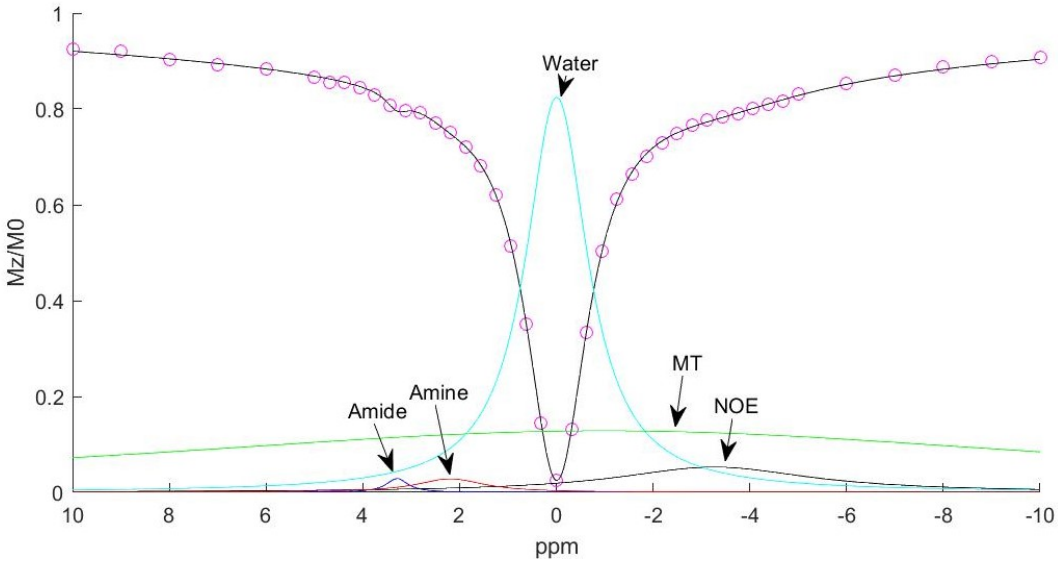

Figure 1. 7 *CEST spectrums from 1 pixel in grey matter. This illustrates that we can fit the amide, amine, NOE, MT and water peak well in the human brain. The saturation power is 0.8μT and saturation time is 3s.*

1.4.4 Omega plot

Dixon et al proposed the omega plot in 2010 and demonstrated that it could determine the chemical exchange rate (k) independent of the CEST agent concentration(32). In an omega plot, by taking the inverse of the saturation power, one creates a linear relationship as follows

$$\frac{M_z}{M_0 - M_z} = fkR_1(\frac{1}{k^2} + \frac{1}{\omega^2})$$

Where M_z is signal intensity in state steady, M_0 is the image without saturation, f is the concentration ratio between CEST agent and water, k is the exchange rate, R_1 is the longitudinal relaxation rate, ω is the saturation power.

In this linear equation, the x term is the reciprocal of ω square ($1/\omega^2$), and y term is $\frac{M_z}{M_0 - M_z}$. The x-intercept is equal to $-1/k^2$. Therefore, the exchange rate (k) is straightforward to be calculated if we have more than two ω. However, this relationship requires a steady state saturation, which is relatively easy to implement in paramagnetic agents since the chemical shift is large enough.

To extend this approach to diamagnetic agents, Sun et al introduced a crucial factor of RF spillover and demonstrated that it could simultaneously determine labile proton ratio and exchange rate in a relatively small chemical shift (33, 34). Compared to the traditional quantification methods, such as quantifying exchange using saturation time (QUEST)

dependence and quantifying exchange using saturation power (QUESP) dependence, the Omega plot related methods are simplified and credible. QUEST and QUESP methods fit the exponential term and require more saturation powers. In further consideration of the impact of the exchange rate, Randtke et al proposed a simplistic method called linear Hanes-Woolf plot to quantify the fast exchange rate agent (35).

1.4.5 B0 and B1 corrections

B0 and B1 corrections are important when their inhomogeneity is significant which is often the case at higher fields for human brain. The most stable method to correct B0 inhomogeneity is water saturation shift referencing (WASSR) method proposed by Kim in 2009(36). WASSR uses the acquisition of a narrow-range, low power Z-spectrum around water frequency to identify the minimum value and measure the absolute water frequency in each voxel. This method allows proper centering of Z-spectrum on a voxel-by-voxel basis independent of spatial B0 field variations. The limitation of this method is it is time-consuming.

An alternative way to correct B0 is to obtain an independent B0 map and shift the Z-spectrum accordingly. Sun et al have proposed an algorithm that can compensate for typical B0 and B1 field inhomogeneity-induced errors in CEST imaging(37). The simplest way is to interpolate the Z-spectrum directly, identify the minimum, and then re-align the zero frequency with the minimum(38). Recently, Schuenke et al proposed a new method called Simultaneous Mapping of Water Shift and B1 (WASABI) and successfully applied it to the human brain(39).

1.5 Application of CEST

The applications of CEST are still under-exploited. In this section, key applications of CEST will be discussed. Only the methods used in the thesis are included.

1.5.1 Amide proton transfer imaging

Amide proton transfer (APT) is a novel imaging technique that can detect amide metabolic changes in the microenvironment(2, 40). An amide is any organic compound containing the group -NH_2, which is widely found in various proteins in vivo. Amide proton typically has a chemical shift at 8.2 ppm, which is 3.5 ppm higher than water frequency and have an exchange rate of ~30 Hz (3). The disparity of amide can be a critical indicator for diverse diseases such as tumor and stroke (3, 41).

The theory of APT is dependent on chemical exchange saturation transfer, in which an off-resonance irradiation pulse is used to specifically saturate the amide hydrogen, then the saturation effect will transfer to the water molecule through chemical exchange phenomenon(42). Amide metabolism can then be imaged indirectly by examining the water proton signal. Based on the cascade amplification of chemical exchange, APT images usually have excellent sensitivity and spatial resolution compared to other metabolic methods such as MR spectroscopy (43-45). Moreover, the environmental homeostasis is not disturbed by contrast agent administration since APT relies on endogenous contrast (46).

Many studies indicated that the signal intensity of APT increased in solid tumors, which might attribute to the higher concentrations of mobile proteins and peptides in the tumor. Wen et al demonstrated that APT imaging might enhance non-invasive identification of tissue heterogeneity in high-grade brain tumors(47). Zhou et al further revealed that APT imaging could be used to differentiate tumor recurrence and radiation necrosis after brain tumor therapy, which was of significant in clinical diagnosis(40). Our previous study indicated that the signal intensity of APT increased as the tumor progresses (Figure 8) (48).

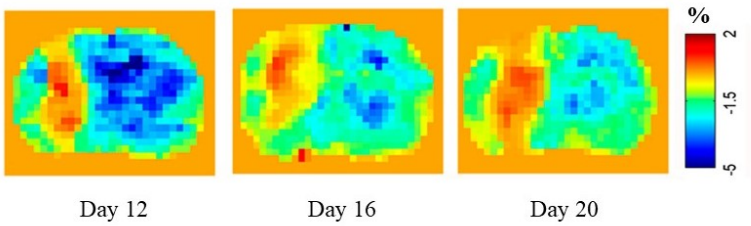

Figure 1. 8 *APT images of the tumor rat brain (From day 12 to day 20 after modeling). The* signal intensity of APT increased as the tumor progression.

In addition, APT imaging has been applied to other diseases such as lymphedema and Alzheimer's disease(49, 50). Lymphedema is swelling caused by a build-up of lymph fluid that is protein-rich. Donahue et al found an increase in APT contrast in the affected arms of the breast cancer treatment-related lymphedema patients and the variability among patients was consistent with documented damage to lymphatics as quantified by lymphedema stage(49). Recently, Wells et al indicated a decreased APT in the hippocampus in Alzheimer's disease models(50).

1.5.2 pH imaging

pH is a scale of acidity from 0 to 14. pH balance is part of the body homeostasis concerning the proper harmony between acids and bases (51). It is a very important biochemical property that has been known to be altered in many pathological states, such as tumor, stroke, etc. Monitoring pH is of significance in early diagnosis and treatment therapy. However, there is a lack of non-invasive methods to image pH in vivo effectively. The gold standard 31P MRS has poor spatial resolution and is unable to display elaborate anatomic structure. It has been reported that the CEST technique can solve this problem.

CEST-based pH technology can detect pH both intracellular and extracellular. Previous studies have demonstrated the close relationship between chemical exchange rate and pH values. Among them, the widely used technique is APT based, in which the exchange rate of amide can be calculated through multiple saturation powers. Sun et al demonstrated that pH image could subdivide the perfusion weighted image (PWI) – diffusion weighted image (DWI) mismatch and delineate the ischemic penumbra more precisely(52-54). By a series of optimization and corrections, they finally quantified the pH values of the contralateral normal tissue to be 7.03±0.05, and the ipsilateral ischemic tissue pH was 6.44±0.24(54-56). Another creative method to detect pH is amine/amide concentration independent detection (AACID) proposed by McVicar et al(57, 58). This method compares the ratio of CEST contrasts at 3.5 and 2.75 ppm to exploit the opposite pH dependencies of CEST signal amplitudes on the chemical exchange rates of amide and amine protons, which has shown promise for detecting changes in response to

antitumor treatment(59). Extracellular pH was usually measured by paramagnetic CEST(60) or other contrast agents(61, 62).

1.5.3 Glutamate imaging

Glutamate is an essential excitatory neurotransmitter in the brain and is widely involved in various functional activities of the central nervous system (63). Under physiological conditions, the release of glutamate is one of the critical factors that promotes neural remodeling, and it is closely related to cognitive functions such as learning and memory. However, in pathological conditions, the excessive release of glutamate leads to neurotoxic excitotoxicity, a pathogenesis of many neurological diseases. In the case of acute ischemic stroke, the release of glutamate to the extracellular space will cause cell apoptosis in the penumbra. Blocking the glutamate receptor can maximally rescue the ischemic penumbra region(64). In glioma, glutamate mediates the proliferation and infiltration of tumors(65), and it is also one of the important triggers of tumor initiated seizures(66).

Glutamate chemical exchange saturation transfer (GluCEST) was proposed by Kj Cai et al. and was derived from traditional chemical exchange saturation transfer(4). GluCEST uses high saturation power, usually higher than 3 μT, and relatively short saturation time to maximum the CEST effect and avoid direct water saturation. The saturation frequency of glutamate is at 3 ppm, and the exchange rate is about 4500 s^{-1}. GluCEST image is commonly calculated using the MTR asymmetry analysis equation.

Since the inception of GluCEST in 2012, Reddy's research team continued to explore its application in different diseases(67, 68) and proved its versatility. They used the technique to detect the alteration of glutamate in the striatum in a dopamine-deficient mouse model and to detect the expression of protease using polyglutamate as the molecular probe. In patients with schizophrenia, the signal intensity of subcortical glutamate imaging was lower than that of normal(69). In patients with epilepsy, glutamate imaging can show changes in the hippocampus which were associated with seizures(67). In addition, Pépin et al. performed GluCEST on a mouse model of Huntington's disease and found the abnormal deficit of signal intensity in the striatum and corpus callosum(70). In our previous studies, we also optimized the saturation power and preliminarily applied glutamate imaging in animal stroke models(71).

Other metabolites such as creatine, myoinositol, γ-aminobutyric acid, and glucose also have CEST effect. Since they all have different chemical exchange rate and chemical shift, it is possible to distinguish them with high magnetic field. Cai et al suggested that creatine CEST MRI may help differentiate gliomas with different aggressiveness(72). Walker-Samuel et al demonstrated that glucose CEST is sensitive to tumor glucose accumulation in colorectal tumor models and can distinguish tumor types with differing metabolic characteristics and pathophysiologies(73).

1.6 Summary

In summary, CEST provides a novel MRI technology that is able to detect and quantify specific components that are not imaged by routine MRI methods, enabling the detection of metabolic

changes, potentially in the early stages of the disease. However, the CEST sequence is not a standard sequence on clinical MRI scanners, so the implementation of CEST needs a special sequence and corresponding post-processing software, which require further optimization and improvement. In previous research, CEST MRI has been shown capable of detecting a host of biomolecules including amide, glutamate, glucose as well as pH and temperature, etc. It will have broad prospects with its application in different diseases to be explored.

This thesis contains three major projects, including sequence development and optimization at 7T, animal studies at 7T, and human application at 3T. In addition, a smaller project on pH imaging in CEST, including pH weighted imaging in a diabetic stroke model, and quantitative pH imaging, was compressed into another independent chapter.

Reference

1. K. M. Ward AHA, and R. S. Balaban. A New Class of Contrast Agents for MRI Based on Proton Chemical Exchange Dependent Saturation Transfer (CEST). Journal of Magnetic Resonance. 2000;143(1):79-87. doi: 10.1006/jmre.1999.1956.

2. Zhou J, Lal B, Wilson DA, Laterra J, van Zijl P. Amide proton transfer (APT) contrast for imaging of brain tumors. Magnetic Resonance in Medicine. 2003;50(6):1120-6.

3. Zhou J, Payen J-F, Wilson DA, Traystman RJ, van Zijl PC. Using the amide proton signals of intracellular proteins and peptides to detect pH effects in MRI. Nature medicine. 2003;9(8):1085-90.

4. Cai K, Haris M, Singh A, Kogan F, Greenberg JH, Hariharan H, Detre JA, Reddy R. Magnetic resonance imaging of glutamate. Nature Medicine. 2012;18(2):302-6. doi: 10.1038/nm.2615.

5. Nasrallah FA, Pagès G, Kuchel PW, Golay X, Chuang K-H. Imaging brain deoxyglucose uptake and metabolism by glucoCEST MRI. Journal of Cerebral Blood Flow & Metabolism. 2013;33(8):1270-8. doi: 10.1038/jcbfm.2013.79.

6. Haris M, Cai K, Singh A, Hariharan H, Reddy R. In vivo mapping of brain myo-inositol. NeuroImage. 2011;54(3):2079-85. doi: 10.1016/j.neuroimage.2010.10.017.

7. Dai Z, Zhang T, Jia Y, Yan G, Xiao G, Zhang G, Shen Z, Wu R. Glutamate and GABA Imaging at 7 Tesla. International Society of Magnetic Resonance in Medicine 22nd annual meeting. 2014.

8. Hancu I, Dixon WT, Woods M, Vinogradov E, Sherry AD, Lenkinski RE. CEST and PARACEST MR contrast agents. Acta Radiologica. 2010;51(8):910-23. doi: 10.3109/02841851.2010.502126.

9. Suchý M, Li AX, Liu Y, Feng Q, Bartha R, Hudson RH. Preliminary evaluation of PARACEST MRI agents for the detection of nitric oxide synthase. Canadian Journal of Chemistry. 2016;94(8):715-22.

10. Zhou J, Wilson DA, Sun PZ, Klaus JA, van Zijl PCM. Quantitative description of proton exchange processes between water and endogenous and exogenous agents for WEX, CEST, and APT experiments. Magnetic Resonance in Medicine. 2004;51(5):945-52. doi: 10.1002/mrm.20048.

11. Zhou J, Zijl PCMv. Chemical exchange saturation transfer imaging and spectroscopy. Progress in Nuclear

Magnetic Resonance Spectroscopy. 2006;48(2-3):109-36. doi: 10.1016/j.pnmrs.2006.01.001.

12. Schröder L, Lowery TJ, Hilty C, Wemmer DE, Pines A. Molecular imaging using a targeted magnetic resonance hyperpolarized biosensor. Science. 2006;314(5798):446-9.

13. Togao O, Kessinger CW, Huang G, Soesbe TC, Sagiyama K, Dimitrov I, Sherry AD, Gao J, Takahashi M. Characterization of Lung Cancer by Amide Proton Transfer (APT) Imaging: An In-Vivo Study in an Orthotopic Mouse Model. PloS one. 2013;8(10):e77019.

14. Kunth M, Witte C, Schröder L. Continuous-wave saturation considerations for efficient xenon depolarization. NMR in Biomedicine. 2015;28(6):601-6.

15. Sun PZ, Benner T, Kumar A, Sorensen AG. Investigation of optimizing and translating pH-sensitive pulsed-chemical exchange saturation transfer (CEST) imaging to a 3T clinical scanner. Magnetic Resonance in Medicine. 2008;60(4):834-41. doi: 10.1002/mrm.21714.

16. Zu Z, Li K, Janve VA, Does MD, Gochberg DF. Optimizing pulsed-chemical exchange saturation transfer imaging sequences. Magn Reson Med. 2011;66(4):1100-8. doi: 10.1002/mrm.22884. PubMed PMID: 21432903; PubMed Central PMCID: PMC3151337.

17. Schmitt B, Zaiß M, Zhou J, Bachert P. Optimization of pulse train presaturation for CEST imaging in clinical scanners. Magnetic Resonance in Medicine. 2011;65(6):1620-9. doi: 10.1002/mrm.22750.

18. Sun PZ, Lu J, Wu Y, Xiao G, Wu RH. Evaluation of the dependence of CEST-EPI measurement on repetition time, RF irradiation duty cycle and imaging flip angle for enhanced pH sensitivity. Physics in Medicine and Biology. 2013;58(17):N229-N40. doi: 10.1088/0031-9155/58/17/n229. PubMed PMID: WOS:000323517700001.

19. Longo DL, Dastrù W, Digilio G, Keupp J, Langereis S, Lanzardo S, Prestigio S, Steinbach O, Terreno E, Uggeri F, Aime S. Iopamidol as a responsive MRI-chemical exchange saturation transfer contrast agent for pH mapping of kidneys: In vivo studies in mice at 7 T. Magnetic Resonance in Medicine. 2010:n/a-n/a. doi: 10.1002/mrm.22608.

20. Zu Z, Janve VA, Xu J, Does MD, Gore JC, Gochberg DF. A new method for detecting exchanging amide protons using chemical exchange rotation transfer. Magnetic Resonance in Medicine. 2013;69(3):637-47. doi: 10.1002/mrm.24284.

21. Zu Z, Xu J, Li H, Chekmenev EY, Quarles CC, Does MD, Gore JC, Gochberg DF. Imaging amide proton transfer

and nuclear overhauser enhancement using chemical exchange rotation transfer (CERT). Magnetic resonance in medicine. 2014;72(2):471-6.

22. Lin EC, Li H, Zu Z, Louie EA, Lankford CL, Dortch RD, Does MD, Gore JC, Gochberg DF. Chemical exchange rotation transfer (CERT) on human brain at 3 Tesla. Magnetic resonance in medicine. 2018.

23. Scheidegger R, Vinogradov E, Alsop DC. Amide proton transfer imaging with improved robustness to magnetic field inhomogeneity and magnetization transfer asymmetry using saturation with frequency alternating RF irradiation. Magnetic Resonance in Medicine. 2011;66(5):1275-85. doi: 10.1002/mrm.22912.

24. Xu X, Lee J-S, Jerschow A. Ultrafast Scanning of Exchangeable Sites by NMR Spectroscopy. Angewandte Chemie International Edition. 2013;52(32):8281-4. doi: 10.1002/anie.201303255.

25. Xu X, Yadav NN, Song X, McMahon MT, Jerschow A, Van Zijl PC, Xu J. Screening CEST contrast agents using ultrafast CEST imaging. Journal of magnetic resonance. 2016;265:224-9.

26. Jin T, Autio J, Obata T, Kim SG. Spin-locking versus chemical exchange saturation transfer MRI for investigating chemical exchange process between water and labile metabolite protons. Magnetic Resonance in Medicine. 2011;65(5):1448-60.

27. Friedman JI, McMahon MT, Stivers JT, Van Zijl PCM. Indirect detection of labile solute proton spectra via the water signal using frequency-labeled exchange (FLEX) transfer. Journal of the American Chemical Society. 2010;132(6):1813-5.

28. Hua J, Jones CK, Blakeley J, Smith SA, Van Zijl PC, Zhou J. Quantitative description of the asymmetry in magnetization transfer effects around the water resonance in the human brain. Magnetic Resonance in Medicine: An Official Journal of the International Society for Magnetic Resonance in Medicine. 2007;58(4):786-93.

29. Zaiss M, Schmitt B, Bachert P. Quantitative separation of CEST effect from magnetization transfer and spillover effects by Lorentzian-line-fit analysis of z-spectra. Journal of magnetic resonance. 2011;211(2):149-55.

30. Desmond KL, Moosvi F, Stanisz GJ. Mapping of amide, amine, and aliphatic peaks in the CEST spectra of murine xenografts at 7 T. Magnetic resonance in medicine. 2014;71(5):1841-53.

31. Cai K, Singh A, Poptani H, Li W, Yang S, Lu Y, Hariharan H, Zhou XJ, Reddy R. CEST signal at 2 ppm (CEST@ 2ppm) from Z-spectral fitting correlates with creatine distribution in brain tumor. NMR in biomedicine. 2015;28(1):1-8.

32. Dixon WT, Ren J, Lubag AJ, Ratnakar J, Vinogradov E, Hancu I, Lenkinski RE, Sherry AD. A concentration-independent method to measure exchange rates in PARACEST agents. Magnetic Resonance in Medicine. 2010;63(3):625-32.

33. Wu RH, Xiao G, Zhou IY, Ran CZ, Sun PZ. Quantitative chemical exchange saturation transfer (qCEST) MRI - omega plot analysis of RF-spillover-corrected inverse CEST ratio asymmetry for simultaneous determination of labile proton ratio and exchange rate. Nmr in Biomedicine. 2015;28(3):376-83. doi: 10.1002/nbm.3257. PubMed PMID: WOS:000350139800011.

34. Sun PZ, Wang Y, Dai ZZ, Xiao G, Wu RH. Quantitative chemical exchange saturation transfer (qCEST) MRI - RF spillover effect-corrected omega plot for simultaneous determination of labile proton fraction ratio and exchange rate. Contrast Media & Molecular Imaging. 2014;9(4):268-75. doi: 10.1002/cmmi.1569. PubMed PMID: WOS:000333825300002.

35. Randtke EA, Chen LQ, Corrales LR, Pagel MD. The Hanes-Woolf linear QUESP method improves the measurements of fast chemical exchange rates with CEST MRI. Magnetic resonance in medicine. 2014;71(4):1603-12.

36. Kim M, Gillen J, Landman BA, Zhou J, van Zijl PCM. Water saturation shift referencing (WASSR) for chemical exchange saturation transfer (CEST) experiments. Magnetic Resonance in Medicine. 2009;61(6):1441-50. doi: 10.1002/mrm.21873.

37. Sun PZ, Farrar CT, Sorensen AG. Correction for artifacts induced by B0 and B1 field inhomogeneities in pH sensitive chemical exchange saturation transfer (CEST) imaging. Magnetic Resonance in Medicine. 2007;58(6):1207-15.

38. Stancanello J, Terreno E, Castelli DD, Cabella C, Uggeri F, Aime S. Development and validation of a smoothing-splines-based correction method for improving the analysis of CEST-MR images. Contrast Media & Molecular Imaging. 2008;3(4):136-49. doi: 10.1002/cmmi.240.

39. Schuenke P, Windschuh J, Roeloffs V, Ladd ME, Bachert P, Zaiss M. Simultaneous mapping of water shift and B1 (WASABI)—Application to field-Inhomogeneity correction of CEST MRI data. Magnetic resonance in medicine. 2017;77(2):571-80.

40. Zhou J, Tryggestad E, Wen Z, Lal B, Zhou T, Grossman R, Wang S, Yan K, Fu D-X, Ford E. Differentiation between glioma and radiation necrosis using molecular magnetic resonance imaging of endogenous proteins and peptides. Nature medicine. 2011;17(1):130-4.

41. Jones KM, Pollard AC, Pagel MD. Clinical applications of chemical exchange saturation transfer (CEST) MRI. Journal of Magnetic Resonance Imaging. 2018;47(1):11-27.

42. van Zijl PCM, Yadav NN. Chemical exchange saturation transfer (CEST): What is in a name and what isn't? Magnetic Resonance in Medicine. 2011;65(4):927-48. doi: 10.1002/mrm.22761.

43. Sun PZ, Xiao G, Zhou IY, Guo Y, Wu R. A method for accurate pH mapping with chemical exchange saturation transfer (CEST) MRI. Contrast Media Mol Imaging. 2016;11(3):195-202. doi: 10.1002/cmmi.1680. PubMed PMID: 26689424.

44. Wu R, Xiao G, Zhou IY, Ran C, Sun PZ. Quantitative chemical exchange saturation transfer (qCEST) MRI - omega plot analysis of RF-spillover-corrected inverse CEST ratio asymmetry for simultaneous determination of labile proton ratio and exchange rate. NMR Biomed. 2015;28(3):376-83. doi: 10.1002/nbm.3257. PubMed PMID: 25615718; PubMed Central PMCID: PMC4339459.

45. Dai Z, Ji J, Xiao G, Yan G, Li S, Zhang G, Lin Y, Shen Z, Wu R. Magnetization Transfer Prepared Gradient Echo MRI for CEST Imaging. PloS one. 2014;9(11):e112219.

46. Sun PZ, Xiao G, Zhou IY, Guo Y, Wu R. A method for accurate pH mapping with chemical exchange saturation transfer (CEST) MRI. Contrast media & molecular imaging. 2016;11(3):195-202.

47. Wen Z, Hu S, Huang F, Wang X, Guo L, Quan X, Wang S, Zhou J. MR imaging of high-grade brain tumors using endogenous protein and peptide-based contrast. NeuroImage. 2010;51(2):616-22. doi: 10.1016/j.neuroimage.2010.02.050.

48. Tang X, Dai Z, Xiao G, Yan G, Shen Z, Zhang T, Zhang G, Zhuang Z, Shen Y, Zhang Z, Hu W, Wu R. Nuclear Overhauser Enhancement-Mediated Magnetization Transfer Imaging in Glioma with Different Progression at 7 T. ACS chemical neuroscience. 2017;8(1):60-6.

49. Donahue MJ, Donahue PC, Rane S, Thompson CR, Strother MK, Scott AO, Smith SA. Assessment of lymphatic impairment and interstitial protein accumulation in patients with breast cancer treatment‐related lymphedema

using CEST MRI. Magnetic resonance in medicine. 2016;75(1):345-55.

50. Wells JA, O'Callaghan JM, Holmes HE, Powell NM, Johnson RA, Siow B, Torrealdea F, Ismail O, Walker-Samuel S, Golay X. In vivo imaging of tau pathology using multi-parametric quantitative MRI. Neuroimage. 2015;111:369-78.

51. Bates RG. Determination of pH: theory and practice. Determination of pH: theory and practice. 1964.

52. Sun PZ, Zhou J, Sun W, Huang J, van Zijl PCM. Detection of the ischemic penumbra using pH-weighted MRI. Journal of Cerebral Blood Flow & Metabolism. 2006;27(6):1129-36. doi: 10.1038/sj.jcbfm.9600424.

53. Sun PZ, Benner T, Copen WA, Sorensen AG. Early Experience of Translating pH-Weighted MRI to Image Human Subjects at 3 Tesla. Stroke. 2010;41(10, Supple 1):S147-S51. doi: 10.1161/strokeaha.110.595777.

54. Sun PZ, Wang E, Cheung JS. Imaging acute ischemic tissue acidosis with pH-sensitive endogenous amide proton transfer (APT) MRI—Correction of tissue relaxation and concomitant RF irradiation effects toward mapping quantitative cerebral tissue pH. NeuroImage. 2012;60(1):1-6. doi: 10.1016/j.neuroimage.2011.11.091.

55. Wu RH LC, Liu PK, Sun PZ. Improved measurement of labile proton concentration-weighted chemical exchange rate (kws) with experimental factor-compensated and T1-normalized quantitative chemical exchange saturation transfer (CEST) MRI. Contrast Media & Molecular Imaging. 2012;in press.

56. Phillip Zhe Sun YW, Gang Xiao, Renhua Wu. Simultaneous determination of labile proton fraction ratio and exchange rate with irradiation radio frequency (RF) power dependent quantitative CEST MRI analysis. Contrast Media and Molecular Imaging. 2012;Accepted.

57. McVicar N, Li AX, Goncalves DF, Bellyou M, Meakin SO, Prado MA, Bartha R. Quantitative tissue pH measurement during cerebral ischemia using amine and amide concentration-independent detection (AACID) with MRI. Journal of Cerebral Blood Flow & Metabolism. 2014;34(4):690-8.

58. Albatany M, Li A, Meakin S, Bartha R. Dichloroacetate induced intracellular acidification in glioblastoma: in vivo detection using AACID-CEST MRI at 9.4 Tesla. Journal of neuro-oncology. 2018;136(2):255-62.

59. Marathe K, McVicar N, Li A, Bellyou M, Meakin S, Bartha R. Topiramate induces acute intracellular acidification in glioblastoma. Journal of neuro-oncology. 2016;130(3):465-72.

60. Liu G, Li Y, Sheth VR, Pagel MD. Imaging in vivo extracellular pH with a single paramagnetic chemical exchange saturation transfer magnetic resonance imaging contrast agent. Molecular imaging. 2012;11(1):7290.2011. 00026.

61. Longo DL, Sun PZ, Consolino L, Michelotti FC, Uggeri F, Aime S. A general MRI-CEST ratiometric approach for

pH imaging: demonstration of in vivo pH mapping with iobitridol. Journal of the American Chemical Society. 2014;136(41):14333-6.

62. Chen LQ, Howison CM, Jeffery JJ, Robey IF, Kuo PH, Pagel MD. Evaluations of extracellular pH within in vivo tumors using acidoCEST MRI. Magnetic resonance in medicine. 2014;72(5):1408-17.

63. Javitt DC, Carter CS, Krystal JH, Kantrowitz JT, Girgis RR, Kegeles LS, Ragland JD, Maddock RJ, Lesh TA, Tanase C, Corlett PR, Rothman DL, Mason G, Qiu M, Robinson J, Potter WZ, Carlson M, Wall MM, Choo TH, Grinband J, Lieberman JA. Utility of Imaging-Based Biomarkers for Glutamate-Targeted Drug Development in Psychotic Disorders: A Randomized Clinical Trial. JAMA psychiatry. 2018;75(1):11-9. Epub 2017/11/24. doi: 10.1001/jamapsychiatry.2017.3572. PubMed PMID: 29167877; PubMed Central PMCID: PMCPmc5833531.

64. Andrabi SA, Kang HC, Haince JF, Lee YI, Zhang J, Chi Z, West AB, Koehler RC, Poirier GG, Dawson TM. Iduna protects the brain from glutamate excitotoxicity and stroke by interfering with poly (ADP-ribose) polymer-induced cell death. Nature Medicine. 2011;17(6):692-9.

65. Yu L, Wall BA, Wangari-Talbot J, Chen S. Metabotropic glutamate receptors in cancer. Neuropharmacology. 2017;115:193-202.

66. Huberfeld G, Vecht CJ. Seizures and gliomas [mdash] towards a single therapeutic approach. Nature Reviews Neurology. 2016;12(4):204-16.

67. Davis KA, Nanga RPR, Das S, Chen SH, Hadar PN, Pollard JR, Lucas TH, Shinohara RT, Litt B, Hariharan H. Glutamate imaging (GluCEST) lateralizes epileptic foci in nonlesional temporal lobe epilepsy. Science translational medicine. 2015;7(309):309ra161-309ra161.

68. Goryawala MZ, Sheriff S, Maudsley AA. Regional distributions of brain glutamate and glutamine in normal subjects. NMR in Biomedicine. 2016;29(8):1108-16.

69. Roalf DR, Nanga RPR, Rupert PE, Hariharan H, Quarmley M, Calkins ME, Dress E, Prabhakaran K, Elliott MA, Moberg PJ. Glutamate imaging (GluCEST) reveals lower brain GluCEST contrast in patients on the psychosis spectrum. Molecular psychiatry. 2017;22(9):1298.

70. Pépin J, Francelle L, Carrillo-de Sauvage M-A, de Longprez L, Gipchtein P, Cambon K, Valette J, Brouillet E, Flament J. In vivo imaging of brain glutamate defects in a knock-in mouse model of Huntington's disease. NeuroImage. 2016;139:53-64.

71. Dai Z, Zhang T, Yan G, Jia Y, Gen K, Xiao G, Zhang G, Shen Z, Wu R. Glutamate imaging. Contrast Media & Molecular Imaging. 2014;9(6):429.

72. Cai K, Tain R-W, Zhou XJ, Damen FC, Scotti AM, Hariharan H, Poptani H, Reddy R. Creatine CEST MRI for differentiating gliomas with different degrees of aggressiveness. Molecular Imaging and Biology. 2017;19(2):225-32.

73. Walker-Samuel S, Ramasawmy R, Torrealdea F, Rega M, Rajkumar V, Johnson SP, Richardson S, Gonçalves M, Parkes HG, Årstad E. In vivo imaging of glucose uptake and metabolism in tumors. Nature medicine. 2013;19(8):1067-72.

Chapter 2

Magnetization Transfer Prepared Gradient Echo MRI for CEST Imaging

This chapter is a version of the published manuscript" Dai Z, Ji J, Xiao G, Yan G, Li S, Zhang G, Lin Y, Shen Z, Wu R. Magnetization Transfer Prepared Gradient Echo MRI for CEST Imaging. PloS one. 2014;9(11):e112219."

Abstract

Chemical exchange saturation transfer (CEST) is an emerging MRI contrast mechanism that is capable of noninvasively imaging dilute CEST agents and local properties such as pH and temperature, augmenting routine MRI methods. However, routine CEST MRI includes a long RF saturation pulse followed by fast image readout, which is associated with high specific absorption rate and limited spatial resolution. In addition, echo planar imaging (EPI)-based fast image readout is prone to image distortion, particularly severe at high field. To address these limitations, we evaluated magnetization transfer (MT) prepared gradient echo (GRE) MRI for CEST imaging. We proved the feasibility using numerical simulations and experiments in vitro and in vivo. Then we optimized the sequence by serially evaluating the effects of the number of saturation steps, MT saturation power (B1), GRE readout flip angle (FA), and repetition time (TR) upon the CEST MRI, and further demonstrated the endogenous amide proton CEST imaging in rats brains (n=5) that underwent permanent middle cerebral artery occlusion. The CEST images can identify ischemic lesions in the first 3 hours after occlusion. In summary, our study demonstrated that the readily available MT-prepared GRE MRI, if optimized, is CEST-sensitive and remains promising for translational CEST imaging.

2.1 Introduction

Chemical exchange saturation transfer (CEST) imaging is a variant of magnetization transfer (MT) MRI contrast mechanism that probes the chemical exchange between dilute labile protons and bulk water (74). Specifically, a frequency selective off resonance radio frequency (RF) irradiation pulse is applied to preferentially saturate the exchangeable protons, and the bulk water signal is attenuated due to its exchange with saturated labile protons. Because CEST imaging is sensitive to dilute CEST agents, local pH and temperature, it can be applied in many different aspects (42). Indeed, CEST MRI has been shown capable of detecting a host of biomolecules including glutamate (4), glycogen (75), glucose (76), glycosaminoglycan (77), esterase enzymes (78) and gene expression (79) as well as pH and temperature (3, 54, 80-83), complementing conventional MRI.

For dilute CEST agents undergoing slow and intermediate chemical exchange, the magnitude of CEST effect is typically a few percent and therefore, it is important to improve its sensitivity by optimizing the acquisition and post-processing strategies (84-88). The conventional CEST MRI sequence includes a long irradiation pulse (e.g. continuous wave or RF pulse train) followed by fast image acquisition such as echo planar imaging (EPI), which is prone to image distortion, particularly severe at high field strength. In addition, CEST MRI using rapid acquisition with relaxation enhancement (RARE), fast low angle shot (FLASH) and steady-state free precession (FISP) readout have been proposed (53, 89-91). Importantly, it often requires extensive sequence development and experimental optimization in order to address the stringent requirements of CEST MRI on RF duty cycle, irradiation duration and specific absorption rate (SAR).

Dixon et al proposed interleaving short frequency-selective saturation and spatially selective excitation pulses for CEST imaging, and demonstrated that for short TR, CEST effect approaches its steady state over the saturation time (92). But only paramagnetic CEST (PARACEST) agent was used to show the CEST effect and no in-vivo data were reported. However, PARACEST is relatively straightforward for its negligence of RF spillover effect, which needs to be revised in vivo. In addition, because MT-prepared gradient echo (GRE) MRI is readily available, our study evaluated the dependence of its CEST MRI effect upon experimental parameters, including the number of saturation steps (Steps), MT saturation power (B1), GRE readout flip angle (FA) and repetition time (TR), for optimizing MTprepared CEST MRI both in vitro and in vivo.

We also translated the optimized sequence and demonstrated endogenous amide proton transfer (APT) MRI (3, 13), a variant of CEST imaging, in permanent middle cerebral artery occlusion rat brains. To summarize, our study confirmed and optimized the readily available MT-prepared GRE MRI for in vivo CEST imaging.

2.2 Materials and Methods

2.2.1. Tissue-like CEST phantom

Tissue-like CEST phantoms were prepared for optimizing CEST MRI (86). Briefly, 1% agarose was added to phosphate buffered saline (PBS) solution. The mixture was microwave heated, and immersed in a water bath at 45 °C. After the temperature stabilized, the solution was transferred into centrifuge tubes. Creatine was added to reach final concentrations of 50, 100 and 200 mM, and their pH was titrated to 7.0. Tubes were inserted into a phantom holder filled with 1% agarose to minimize the susceptibility mismatch. In addition, another phantom containing 50 and 100 mM creatine in 1% agarose gel was prepared for sequence optimization (i.e. Steps, B1, FA and TR). Both phantoms were solidified at room temperature prior to MRI.

2.2.2. Animal Preparation

All experimental protocols were approved by the Ethics Committee of Shantou University Medical College and all experiments were performed in accordance with guidelines from the Chinese Animal Welfare Agency. Five adult male Sprague Dawley (SD) rats (weighted about 200 g) underwent permanent middle cerebral artery occlusion (MCAO) by thread embolism. First, the rats were anesthetized with 3% pentobarbital, intraperitoneal injection, and immobilized in a standard rat table. Then, MCAO was initiated by inserting the 4-0 nylon suture into the lumen of internal carotid artery to block the origin of the middle cerebral artery. Animal core temperature, respiration and heart rates were monitored throughout the procedure. Another normal adult male SD rat was used for multi-slice CEST imaging. MCAO rats were euthanized with overdose of Phenobarbital by intravenous injection after scanning. All efforts were made to

minimize animal suffering and to reduce the number of animals used.

2.2.3. Simulation of MT-prepared GRE

CEST MRI The time-dependent CEST effect for the proposed MTprepared GRE CEST MRI sequence was analyzed by numerical simulation in Matlab (Mathworks, Natick MA). Specifically, we used Bloch-McConnell equations to simulate the two-pool proton exchange model (93) . We assumed representative relaxation parameters, with $T1_w$ = 1500 ms and $T2_w$ = 45 ms for bulk water, and $T1_s$ = 1000 ms and $T2_s$ = 15 ms for labile proton. A chemical offset of 1050 Hz was chosen for simulation as it represents the frequency offset of ensemble amide proton from endogenous proteins and peptides, observed at 7T. We examined two exchange rates of 30 Hz and 500 Hz respectively, with the same concentration ratio of 1:500 and RF irradiation power of 0.75 mT. We had TR=Tr+Ts+Ti and saturation time=n*TR. Where Tr is the relaxation delay time, Ts is the saturation time, Ti is the image acquisition time and n is the steps of TR. We had Tr=10 ms, Ts=10 ms, Ti=1 ms. In comparison, we simulated the conventional continuous wave pre-saturation with EPI acquisition sequence, with the same physicochemical parameters.

2.2.4. MRI Acquisitions

All MRI experiments were conducted using a horizontal bore (bore size 160 mm) Agilent 7T animal MRI scanner (Agilent, VNMRS, USA) with a 63 mm internal diameter standard ^{1}H volume coil (one-channel) for RF transmission and reception. Field gradients: 400 mT/m in maximum 200A. The B0 field was shimmed using 3D gradient shimming that adjusted high-order gradient shimming currents based on the derived B0 field map. The RF field and

center frequency were calibrated in pre-scan. MT-prepared GRE MRI sequence was used for CEST imaging. First, the CEST imaging and Z-spectrum were demonstrated by tissue-like phantoms and normal SD rat brain. Routine GRE MRI parameters were set: TR/TE=26/2.3 ms and FA=20°, unless specified otherwise. In addition, we had slice thickness=2 mm, field of view (FOV)=34×34 mm^2, imaging matrix=64×64, number of average (NA)=1, dummy scan=4, and bandwidth=50 kHz. Total scan time was about 1.6 s for one slice.

2.2.5. Phantom Optimization

CEST MRI was optimized as functions of the number of saturation steps (Steps), saturation power (B1), GRE readout FA and TR. Specifically, the steps was varied from 32, 64, 128, 192, 256, and 512 to 1024 while the saturation power and duration were set to 0.59 μT and 20 ms. In addition, the MT saturation power was varied from 0.16 μT to 1.12 μT. Specifically, the MT saturation pulse was chosen as a 20 ms duration gauss pulse, with flip angle varied from 50° to 350° with intervals of 50°, so their corresponding powers are from 0.16 μT to 1.12 μT with intervals of 0.16 μT (Steps=256, FA=15° and TR=26 ms). Moreover, FA was varied from 5° to 60° with intervals of 5° or 10° (B1=0.59 μT, Steps=256, and TR=26 ms) and TR was varied from 26 to 210 ms in five steps (B1=0.59 μT, Steps=256 and FA=5°).

2.2.6. In vivo Optimization and Application

In order to be better applied in vivo, the same key parameters (Steps, B1, FA and TR) were also evaluated in five adult male MCAO SD rats in the first three hours after occlusion. The rat was anesthesia and immobilized in a standard rat cradle. Images were averaged 64 times to improve its signal to noise ratio caused by the use of volume coil. First, the number of saturation steps

was varied from 64, 128, 256, 512, 1024 to 2048 while the saturation power and duration were set to 0.39 μT and 15 ms. In addition, the MT saturation power (gauss pulse, 15 ms pulse width) was varied from 0.39 μT to 1.57 μT with intervals of 0.19 μT with Step=4096, TR=21 ms, and FA=5°. Moreover, FA was varied from 5u to 20u with intervals of 5u (B1=0.39 μT, Step=4096 and TR=21 ms) and TR was varied from 21, 30 to 40 ms (B1=0.39 μT, Step=4096 and FA=5°). Regions of interest (ROI) were manually drawn on the ischemic lesions and contralateral normal regions by three expert radiologists. Optimized data were obtained in five MCAO SD rats brains based on the optimized parameters (saturation step=4096, B1=0.39 μT, FA=5°, TR=21 ms). Total scan time was about 1.4 minutes for one image. Other routine MRI sequences: T2-weighted imaging (TR/TE=2000/30 ms, NA=8) and ADC maps (TR/TE=2000/34 ms, NA=8) with b-value of 1000 s/ mm^2 were acquired for reference.

2.2.7. Data Processing

Images were processed using the VnmrJ 3.1A (Agilent, Santa Clara, USA) and Matlab (Mathworks, Natick MA). Z-spectrum were calculated from the normalized images for the ROIs outlined in each phantom compartment. The scatters were drawn with mean signals as ordinate and RF offset as abscissas, smoothed using a spline function (94). CEST images were calculated using the conventional MTR asymmetry analysis of three images: label (I_{label}) and reference (I_{ref}) images with RF saturation applied at the labile proton frequency (1.87 and 3.5 ppm for creatine and in vivo CEST MRI, respectively) and reference frequency (-1.87 and -3.5 ppm, respectively), in addition to a control scan without RF irradiation (I0). The MTRasym was calculated as (3): $MTRasym=(I_{ref} - I_{label})/I0$. Assessment of the contrast between the ischemic lesion and the contralateral normal region were performed via paired t-test. Values were presented as mean ±

SD, and $p < 0.05$ was considered as statistically significant.

2.3 Results

Fig. 2.1 shows the CEST effect as a function of RF saturation time for representative exchange rates and sequences. Specifically, for short TR, the CEST effect increases during the MT duration. Although it may decrease slightly while the MT pulse is off, the CEST effect accumulates and approaches its steady state, similar to that obtainable using the conventional continuous wave saturation pulse sequence. About 4000 TR intervals are required to reach the steady-state CEST effect.

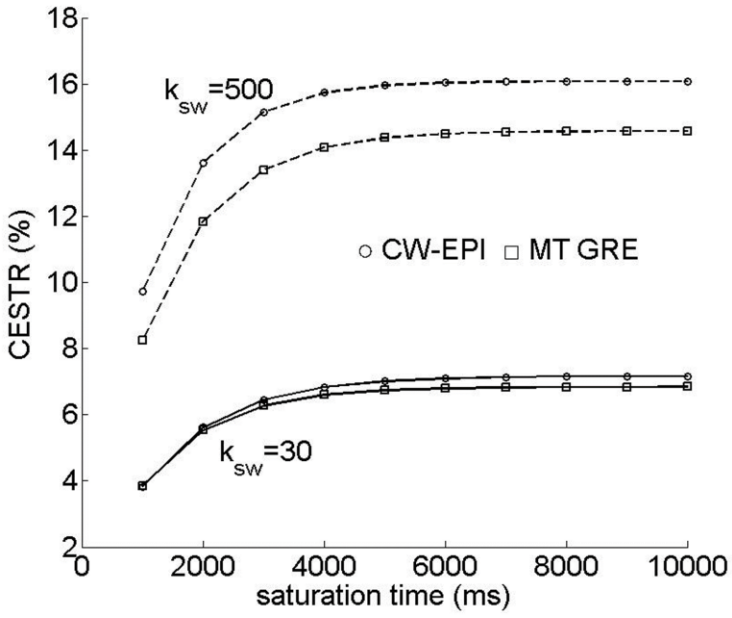

Figure 2. 1 *The figure shows the time-dependent CEST effect for the proposed MT-prepared GRE CEST MRI sequence and compares with that of the conventional continuous wave sequence.*

Fig. 2.2 (A) shows Z-spectrum from compartments of varied creatine concentration of the tissue-like CEST phantom. CEST induced MRI effect can be observed at the labile amine proton chemical shift of 1.87 ppm. Fig. 2.2 (B) shows the CEST-weighted image of the triple-compartment CEST phantom, where the CEST effect was 7.3 ± 3.4%, 16.7 ± 3.2%, and 28.4 ± 3.2% for 50, 100 and 200 mM creatine-gel compartment, respectively.

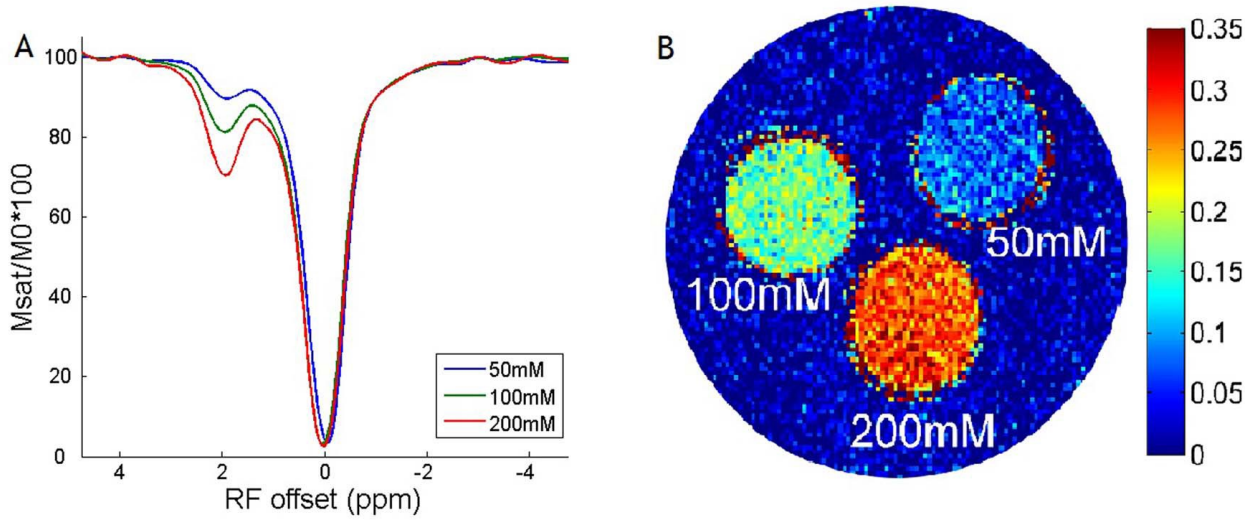

Figure 2. 2 *The figure shows that CEST effect can be observed at the labile amine proton chemical shift of 1.87 ppm.*

Fig. 2.3 shows the phantom optimizations. We evaluate the CEST effect as functions of steps, B1, FA and TR in phantoms. Specifically, CEST effect approached its steady state exponentially with steps (Fig. 2.3A), indicating that CEST effect accumulated as a function of saturation step duration, consistent with the simulation result. Fig. 2.3B shows CEST effects as a function of MT saturation power increasing with B1 up to a peak at about 0.65– 0.98 μT. Fig. 2.3C–D evaluates FA and TR dependence of CEST imaging. CEST effect decreased monotonically with FA (Fig. 2.3C). In addition, CEST effect decreased with TR (Fig. 2.3D), suggesting less effective accumulation of CEST effect at long TR due to competitive T1 relaxation. The data

suggest that for the MTprepared GRE CEST sequence, it is necessary to use small FA and short TR in order to measure CEST effect with adequate sensitivity. We propose using 5° and minimum TR at 7 T.

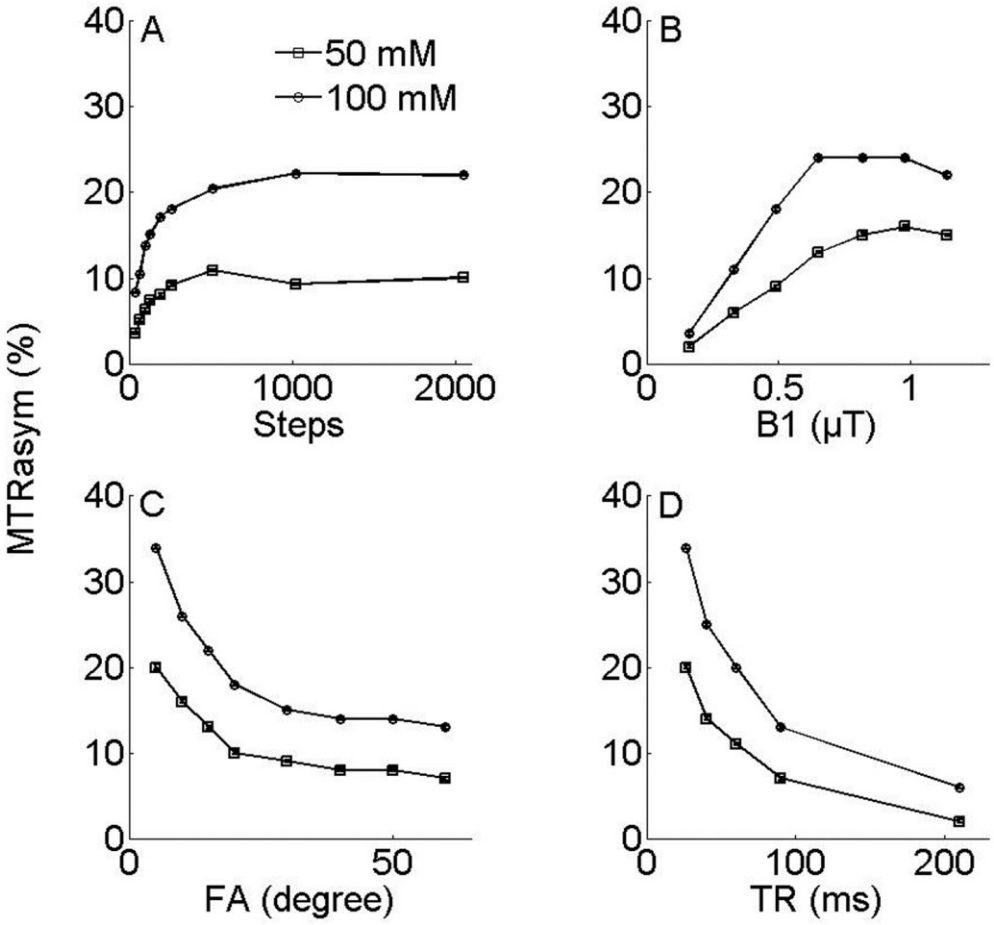

Figure 2. 3 *The figure shows the phantom optimizations. CEST effect approached its steady state exponentially with Steps (Fig. 2.3A). Whereas the CEST effect (Fig. 2.3B) increased with B1 and peaked at about 0.65–0.98μT. The CEST effect decreased monotonically with FA (Fig. 2.3C). In addition, CEST effect decreased with TR (Fig. 2.3D).*

Fig. 2.4 shows the in vivo optimizations in MCAO SD rat brain in the first three hours after occlusion. The same four key parameters, including steps, B1, FA and TR were evaluated. Unlike the results of the phantom experiments, The CEST effects in vivo were negative owning to interference with nuclear overhauser effects (NOE). We could not distinguish them in the CEST imaging with the existing technology, so we used the MTRasym contrast between ischemic lesion and normal region as the assessment index for optimization. Specifically, Fig. 2.4A indicates that CEST effect approached its steady state exponentially with steps in both normal and ischemic regions. Fig. 2.4B shows CEST effect as functions of B1. The CEST effect increased with B1, whereas the contrasts between the normal and ischemic regions were getting smaller. The contrasts peaked at about 0.39,0.78 μT and disappeared at 1.57 μT. Fig. 2.4C–D evaluates FA and TR dependence of CEST imaging. The contrasts between the normal and ischemic regions were decreased both with FA (Fig. 2.4C) and TR (Fig. 2.4D). The data also suggest that for the MT prepared GRE CEST sequence, the optimized parameters in vivo for MCAO are as following: Steps=2000, B1=0.39,0.78 μT, FA=5°, TR=21 ms.

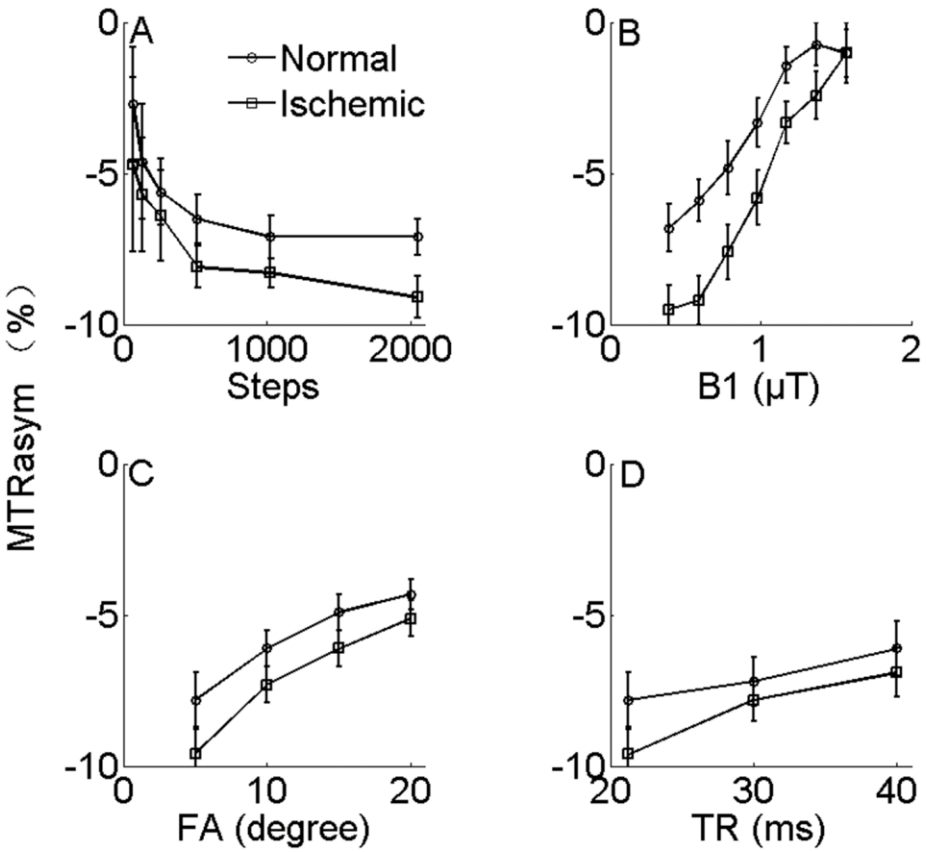

Figure 2. 4 *The figure shows the in vivo optimizations in MCAO SD rat brain in the first three hours after occlusion. Fig. 2. 4A indicates that CEST effect approached its steady state exponentially with Steps in both normal and ischemic regions. Fig. 2.4B shows CEST effect as functions of MT saturation power (B1). The contrasts were decreasing both with increasing FA (Fig. 2.4C) and TR (Fig. 2.4D).*

Fig. 2.5 shows the CEST imaging and Z-spectrum of MCAO SD rat brains (n=5) using optimized MT-prepared GRE MRI sequence, and compare them with other routine imaging. The ischemic region was not seen in the normal T2-weighted images in the first 3 hours after occlusion. However, it could be identified in CEST images and ADC images. The CEST effect calculated from the asymmetry analysis was 29.6%, 60.9%, and 27.0%, 60.8% for the ischemic and the contralateral normal region ($p < 0.05$), which was verified by the Z-spectrum (lower left corner). Amide proton shows a relatively clear CEST effect at about 3.5 ppm in Z spectrum.

Moreover, the CEST effect was reduced due to the decrease of pH in the ischemic lesion, which was the mechanism of the contrast between the ischemic and normal region. Note that because of the interference of the NOE, there was a signal decrease on the negative axis, whereas the NOE was almost identical between the ischemic and normal region.

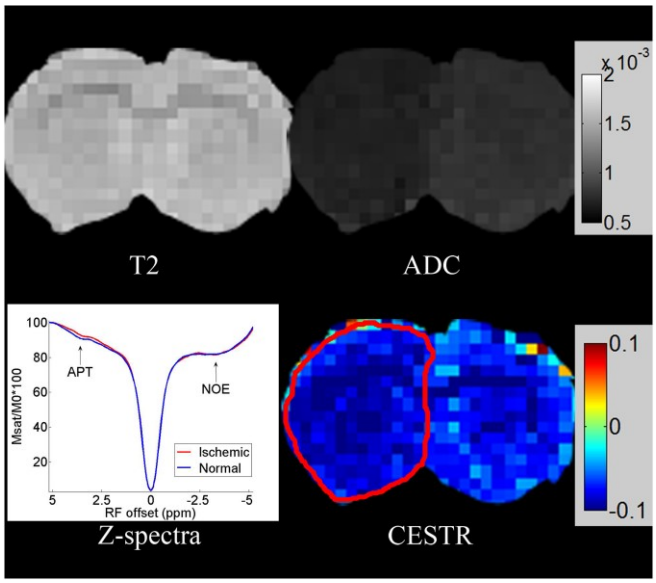

Figure 2. 5 *The figure shows the CEST image and Z-spectrum of one MCAO SD rat brain using the optimized MT-prepared GRE MRI sequence (saturation step=4096, B1=0.39 μT, FA=5°, TR=21 ms), and compares them with other routine images. The CEST effect was verified by the Z-spectrum (lower left corner). The CEST effect was reduced due to the decrease of pH in the ischemic lesion, whereas the NOE was almost the same as in the normal region.*

2.4 Discussion

Our study found that although each brief MT pulse generates a small increase of CEST effect, it cumulates effectively for short TR over the number of saturation steps, consistent with the conclusion of Dixon et al (92). In addition, we assessed the CEST effect for a number of experimental parameters that should help guide the experimental optimization of CEST imaging. Because the center of the k-space determines the image intensity and signal to noise ratio (SNR), initial high k-space data could be acquired during the transient period to improve the acquisition efficiency. Besides, because GRE-based image readout at short echo time is little susceptible to image distortion, it is suitable for applications at high field strength. Moreover, the interleaved MT saturation and GRE readout spread the RF energy deposition throughout the scan when compared to the conventional CEST imaging with fast image readout, which is significant in clinical application because SAR is strictly restricted. In addition, it will be very useful for metabolite CEST like glutamate, glycosaminoglycan etc., which requires high saturation B1 that SAR can be an issue. Furthermore, because the proposed CEST imaging scheme requires little hardware modification and sequence development, it can be implemented on routine scanners and remains promising for clinical translation (95, 96).

Our study showed that CEST effects strongly depend on TR and FA both in vitro and in vivo. Short TR reduces T1 relaxation induced loss of CEST effect for more efficient cumulative effect toward the steady state CEST MRI (97). Because CEST effect decreases with FA, the appropriate FA appears to be 5° at 7 Tesla. In addition, we observed strong dependence of CEST effects on MT saturation power. In creatine agarose CEST phantoms, in which the protons

chemical exchange rate is about 500 Hz at pH 7, the CEST effect increases with saturation power and peaked about 0.65–0.98 μT, similar to that found with pulsed-CEST imaging (16, 85). In vivo, the amide protons chemical exchange rate is about 30 Hz, and we found that the saturation power may range from 0.39 μT to 0.78 μT for optimal contrast between the normal and ischemic regions. In addition, the B1 sensitivity for CEST imaging is relatively small around the optimal RF amplitude (54), consistent with the study of Jokivarsi et al. (98) Moreover, the spatial resolution and sensitivity were sufficient so that the apparent CEST contrast between the ischemic region and normal region could be well delineated.

It is important to note that throughout all the experiments we used a standard one channel volume coil, which allowed us to have better B0 homogeneity than that in smaller coil. The full width at half maximum were about 15 Hz in phantoms and 30 Hz in rat brains. Moreover, although the direct saturation effect makes CEST imaging very sensitive to B0 inhomogeneity, it can be neglected in the APT imaging due to the small saturation B1. However, for large saturation B1, it is necessary to have B0 correction. More importantly, the signal to noise ratio can be improved significantly if the coil is upgraded, and the CEST effects can be easier to be observed. In summary, our study demonstrated that optimized MT-prepared GRE MRI is suitable for in vivo CEST imaging.

In conclusion, our study optimized MT-prepared GRE MRI for CEST imaging by evaluating the effects of the number of saturation steps, MT saturation power, GRE readout FA and TR in tissue-like phantoms. We have also demonstrated the endogenous amide proton CEST MRI both in healthy and in MACO SD rat brains on a 7 T scanner. In conclusion, this method can provide

an alternative, straightforward, and effective way to obtain CEST images on clinic MR scanners without hardware or software modifications.

2.5 Acknowledgments

We thank Julien Poublanc for language checking.

References

1. Ward K, Balaban R. Determination of pH using water protons and chemical exchange dependent saturation transfer (CEST). Magnetic Resonance in Medicine. 2000;44(5):799-802.

2. van Zijl PCM, Yadav NN. Chemical exchange saturation transfer (CEST): What is in a name and what isn't? Magnetic Resonance in Medicine. 2011;65(4):927-48. doi: 10.1002/mrm.22761.

3. Cai K, Haris M, Singh A, Kogan F, Greenberg JH, Hariharan H, Detre JA, Reddy R. Magnetic resonance imaging of glutamate. Nature Medicine. 2012;18(2):302-6. doi: 10.1038/nm.2615.

4. van Zijl PCM, Jones CK, Ren J, Malloy CR, Sherry AD. MRI detection of glycogen in vivo by using chemical exchange saturation transfer imaging (glycoCEST). Proceedings of the National Academy of Sciences. 2007;104(11):4359-64. doi: 10.1073/pnas.0700281104.

5. Zhang S, Trokowski R, Sherry AD. A paramagnetic CEST agent for imaging glucose by MRI. Journal of the American Chemical Society. 2003;125(50):15288-9.

6. Ling W, Regatte RR, Navon G, Jerschow A. Assessment of glycosaminoglycan concentration in vivo by chemical exchange-dependent saturation transfer (gagCEST). Proceedings of the National Academy of Sciences. 2008;105(7):2266-70. doi: 10.1073/pnas.0707666105.

7. Li Y, Sheth VR, Liu G, Pagel MD. A self-calibrating PARACEST MRI contrast agent that detects esterase enzyme activity. Contrast Media Mol Imaging. 2011;6(4):219-28. Epub 2011/08/24. doi: 10.1002/cmmi.421. PubMed PMID: 21861282; PubMed Central PMCID: PMCPmc4879975.

8. Gilad AA, McMahon MT, Walczak P, Winnard PT, Raman V, van Laarhoven HWM, Skoglund CM, Bulte JWM, van Zijl PCM. Artificial reporter gene providing MRI contrast based on proton exchange. Nature biotechnology. 2007;25(2):217-9. doi: 10.1038/nbt1277.

9. Zhou J, Payen J-F, Wilson DA, Traystman RJ, van Zijl PC. Using the amide proton signals of intracellular proteins and peptides to detect pH effects in MRI. Nature medicine. 2003;9(8):1085-90.

10. Sun PZ, Wang E, Cheung JS. Imaging acute ischemic tissue acidosis with pH-sensitive endogenous amide proton transfer (APT) MRI—Correction of tissue relaxation and concomitant RF irradiation effects toward mapping quantitative cerebral tissue pH. NeuroImage. 2012;60(1):1-6. doi: 10.1016/j.neuroimage.2011.11.091.

11. MB Wei ZS, G Xiao, QC Qiu, YW Chen, RH Wu. Imaging pH Phantoms Using Magnetization Transfer Technology at 1.5 Tesla. The 4th International Conference on Biomedical Engineering and Informatics (BMEI)2011. p. 329-32.

12. Sun PZ, Cheung JS, Wang E, Lo EH. Association between pH-weighted endogenous amide proton chemical exchange saturation transfer MRI and tissue lactic acidosis during acute ischemic stroke. Journal of Cerebral Blood Flow & Metabolism. 2011.

13. Longo DL, Dastru W, Digilio G, Keupp J, Langereis S, Lanzardo S, Prestigio S, Steinbach O, Terreno E, Uggeri F, Aime S. Iopamidol as a Responsive MRI-Chemical Exchange Saturation Transfer Contrast Agent for pH Mapping of Kidneys: In Vivo Studies in Mice at 7 T. Magnetic Resonance in Medicine. 2011;65(1):202-11. doi: 10.1002/mrm.22608. PubMed PMID: WOS:000285963500023.

14. Opina ACL, Ghaghada KB, Zhao P, Kiefer G, Annapragada A, Sherry AD. TmDOTA-tetraglycinate encapsulated liposomes as pH-sensitive lipoCEST agents. PloS one. 2011;6(11):e27370.

15. Terreno E, Castelli DD, Viale A, Aime S. Challenges for molecular magnetic resonance imaging. Chem Rev. 2010;110(5):3019-42.

16. Sun PZ, Wang E, Cheung JS, Zhang X, Benner T, Sorensen AG. Simulation and optimization of pulsed radio frequency irradiation scheme for chemical exchange saturation transfer (CEST) MRI-demonstration of pH-weighted pulsed-amide proton CEST MRI in an animal model of acute cerebral ischemia. Magnetic Resonance in Medicine. 2011:n/a-n/a. doi: 10.1002/mrm.22894.

17. Wu R, Liu CM, Liu PK, Sun PZ. Improved measurement of labile proton concentration-weighted chemical exchange rate (kws) with experimental factor-compensated and T1-normalized quantitative chemical exchange saturation transfer (CEST) MRI. Contrast Media & Molecular Imaging. 2012;7(4):384-9.

18. Sun PZ, Wang Y, Xiao G, Wu R. Simultaneous experimental determination of labile proton fraction ratio and exchange rate with irradiation radio frequency power-dependent quantitative CEST MRI analysis. Contrast Media & Molecular Imaging. 2013;8(3):246-51.

19. Sun PZ, Lu J, Wu Y, Xiao G, Wu R. Evaluation of the dependence of CEST-EPI measurement on repetition time, RF irradiation duty cycle and imaging flip angle for enhanced pH sensitivity. Physics in Medicine and Biology. 2013;58(17):N229-N40. doi: 10.1088/0031-9155/58/17/n229.

20. Zhou J, Blakeley JO, Hua J, Kim M, Laterra J, Pomper MG, van Zijl PCM. Practical data acquisition method for human brain tumor amide proton transfer (APT) imaging. Magnetic Resonance in Medicine. 2008;60(4):842-9. doi: 10.1002/mrm.21712.

21. Sun PZ, Benner T, Copen WA, Sorensen AG. Early Experience of Translating pH-Weighted MRI to Image Human Subjects at 3 Tesla. Stroke. 2010;41(10, Supple 1):S147-S51. doi: 10.1161/strokeaha.110.595777.

22. Shah T, Lu L, Dell KM, Pagel MD, Griswold MA, Flask CA. CEST-FISP: A novel technique for rapid chemical exchange saturation transfer MRI at 7 T. Magnetic Resonance in Medicine. 2011;65(2):432-7. doi: 10.1002/mrm.22637.

23. Jones CK, Polders D, Hua J, Zhu H, Hoogduin HJ, Zhou J, Luijten P, van Zijl PC. In vivo three-dimensional whole-brain pulsed steady-state chemical exchange saturation transfer at 7 T. Magn Reson Med. 2012;67(6):1579-89. Epub 2011/11/16. doi: 10.1002/mrm.23141. PubMed PMID: 22083645; PubMed Central PMCID: PMCPmc3291747.

24. Dixon WT, Hancu I, Ratnakar SJ, Sherry AD, Lenkinski RE, Alsop DC. A multislice gradient echo pulse sequence for CEST imaging. Magnetic Resonance in Medicine. 2009:NA-NA. doi: 10.1002/mrm.22193.

25. Togao O, Kessinger CW, Huang G, Soesbe TC, Sagiyama K, Dimitrov I, Sherry AD, Gao J, Takahashi M. Characterization of Lung Cancer by Amide Proton Transfer (APT) Imaging: An In-Vivo Study in an Orthotopic Mouse Model. PloS one. 2013;8(10):e77019.

26. Sun PZ, Zhou J, Huang J, van Zijl P. Simplified quantitative description of amide proton transfer (APT) imaging during acute ischemia. Magnetic Resonance in Medicine. 2007;57(2):405-10. doi: 10.1002/mrm.21151.

27. Terreno E, Stancanello J, Longo D, Castelli DD, Milone L, Sanders HM, Kok MB, Uggeri F, Aime S. Methods for an improved detection of the MRI-CEST effect. Contrast Media Mol Imaging. 2009;4(5):237-47. Epub 2009/10/20. doi: 10.1002/cmmi.290. PubMed PMID: 19839029.

28. Singh A, Haris M, Cai K, Kassey VB, Kogan F, Reddy D, Hariharan H, Reddy R. Chemical exchange saturation transfer magnetic resonance imaging of human knee cartilage at 3 T and 7 T. Magn Reson Med. 2012;68(2):588-94. Epub 2012/01/04. doi: 10.1002/mrm.23250. PubMed PMID: 22213239; PubMed Central PMCID: PMCPmc4067761.

29. Dula AN, Asche EM, Landman BA, Welch EB, Pawate S, Sriram S, Gore JC, Smith SA. Development of chemical exchange saturation transfer at 7T. Magnetic Resonance in Medicine. 2011;66(3):831-8. doi: 10.1002/mrm.22862.

30. Sun PZ, Murata Y, Lu J, Wang X, Lo EH, Sorensen AG. Relaxation-compensated fast multislice amide proton transfer (APT) imaging of acute ischemic stroke. Magnetic Resonance in Medicine. 2008;59(5):1175-82. doi: 10.1002/mrm.21591.

31. Zu Z, Li K, Janve VA, Does MD, Gochberg DF. Optimizing pulsed-chemical exchange saturation transfer imaging sequences. Magn Reson Med. 2011;66(4):1100-8. doi: 10.1002/mrm.22884. PubMed PMID: 21432903; PubMed Central PMCID: PMC3151337.

32. Jokivarsi KT, Gröhn HI, Gröhn OH, Kauppinen RA. Proton transfer ratio, lactate, and intracellular pH in acute cerebral ischemia. Magnetic Resonance in Medicine. 2007;57(4):647-53. doi: 10.1002/mrm.21181.

Chapter 3

Glutamate imaging in cuprizone-exposed C57BL/6 mouse at 7 T: potential diagnosis of schizophrenia prodrome

Abstract

The diagnosis of schizophrenia prodrome is of significance since early intervention may prevent the development of full-blown schizophrenia. Increasing evidence indicates that glutamate is involved in the incidence of schizophrenia. Our previous studies demonstrated that the cuprizone-exposed C57BL/6 mouse showed behavioral changes and has been employed to examine the brain metabolite alterations in various stages of schizophrenia. In this article, we further examine glutamate variation in different brain regions in an early schizophrenia model using a novel glutamate imaging technique. Glutamate imaging was conducted at 7T using an in-house chemical exchange saturation transfer sequence, followed by standard proton spectroscopy. Methods were first verified using glutamate and other metabolite phantoms, prepared into different concentrations in phosphate-buffered saline solution. Cuprizone (0.2%) was infiltrated in rodent chow for 2 weeks to induce schizophrenia models in C57BL/6 mice. Open-field and Y-maze tests were performed to measure the emotional and cognitive behaviors of the models. Our results proved that the signal intensity of the glutamate image was strictly related to glutamate concentration, and that other neuro metabolites contribute negligible glutamate CEST effects except for GABA. Compared to controls, glutamate signals of schizophrenic models increased in the whole brain, especially in the cerebral cortex,

hippocampus, and thalamus. In addition, the glutamate CEST image has excellent correlation with spectroscopy. In conclusion, our study applies a glutamate imaging technique in schizophrenic models and demonstrates that glutamate changes in different regions of the brain at an early stage, which may provide a powerful indicator of the diagnosis of schizophrenia prodrome.

3.1 Introduction

Schizophrenia is a chronic and severe mental illness characterized by the breakdown in the relation between thought, emotion, and behavior. There are three phases of schizophrenia: prodromal, active, and residual. Prodromal schizophrenia refers to the period of deterioration in heterogeneous subjective and behavioral symptoms that precede the onset of clinical psychotic symptoms (99). The diagnosis of schizophrenia prodrome is of significance since the early intervention may prevent the development of full-blown schizophrenia (100). However, it is difficult to diagnose prodromal schizophrenia since patients may only exhibit minor behavioral changes or just anxiety(101). Moreover, about 70% of individuals who fulfill prodromal criteria defined in the fifth edition of the Diagnostic and Statistical Manual of Mental Disorders (DSM-5) do not develop schizophrenia, which leads to unwarranted treatment and stigma (102). Therefore, it is critical to explore and improve the diagnostic technology of prodromal schizophrenia.

Glutamate imaging is a novel technique based on chemical exchange saturation transfer, which has shown potential for diagnosis of neuropsychiatric diseases in recent studies(4). In patients with epilepsy, glutamate imaging can show changes in the hippocampus associated with seizures (67). Pépin et al. performed glutamate imaging on a mouse model of Huntington's disease and found an abnormal deficit of signal intensity on striatum and corpus callosum(70). Reddy et al. used the technique to detect the alteration of glutamate in the striatum in a dopamine-deficient mouse model and to detect the expression of protease using polyglutamate as the molecular probe(103, 104).

With increasing evidence indicating that glutamate is involved in the incidence of schizophrenia (105, 106), we hypothesize that glutamate could be an imaging biomarker in the diagnosis of prodromal schizophrenia. This hypothesis is supported by Roalf et al. who suggest that neurochemical profiles of glutamate across cortex and subcortex may be considered markers of early psychosis (69). Our previous studies also demonstrate that cuprizone-induced C57BL/6 mice show behavioral and pathophysiological changes at about 1 week, which have specific relevance to prodromal schizophrenia (107). When the exposure period is prolonged to 6 weeks, our results indicate metabolite changes in subcortical regions in magnetic resonance spectroscopy (MRS) and provide neurochemical evidence for the impairment of neuronal functions of schizophrenia (108). In this study, we will further image the glutamate variation in different brain regions in a prodromal schizophrenia model using the novel glutamate imaging technique and verify the correlation between glutamate imaging and MRS.

3.2 Materials and Methods

3.2.1 Phantom preparation

All glutamate and other neuro metabolites phantoms were prepared in phosphate buffer saline (PBS) solutions with pH titration to 7.0. All tubes were emerged in 1% agarose gel to minimize the susceptibility inhomogeneity. To verify the relationship between the signal intensity of the glutamate image and the glutamate concentration, the concentration was set to 10, 20, 30, 40, 50 mMol/L, respectively. Other common neuro metabolites, including γ-aminobutyric acid, myoinositol, choline, and creatine, were evaluated with the concentration of 50 mMol/L.

3.2.2 Schizophrenia model

All animal experiments were approved by the Ethics Committee of Shantou University Medical College and conducted according to the guidelines of the Chinese Animal Welfare Agency. Twenty male C57BL/6 mice (Vital River Laboratories, Beijing, China) at 6 weeks of age were randomly assigned into the normal control (Nor) and cuprizone-exposed (CPZ) groups (10 mice per group). In the CPZ group, cuprizone (0.2%, Sigma-Aldrich, St. Louis, MO, USA) was infiltrated in rodent chow for 2 weeks to induce the early stage of schizophrenia models in C57BL/6 mice. During the same period, mice in the control group had the standard chow without cuprizone.

3.2.3 Behavioral tests

Open-field, Y-maze, and social interaction tests were performed to measure the emotional and cognitive behaviors of the models. For the open-field test, each mouse was placed in the center of an open-field box with an area of 50 cm * 50 cm for 5 minutes. The moving trajectory of each subject was recorded and analyzed by a video tracking program (Mobiledatum Information Technology, Shanghai, China). Social interaction test was also measured in this open-field by introducing a social target animal (an unfamiliar C57BL/6 male mouse). An 8-minute Y-maze was performed in each subject to measure the exploring behavior and spatial working memory.

3.2.4 Glutamate image and MRS

All MRI experiments were conducted using a horizontal bore (bore size 160 mm) Agilent 7T animal MRI scanner (Agilent Technologies, Santa Clara, CA). Field gradients: 400 mT/m in maximum 200A. Body temperature was recorded and maintained at 36–37 °C using a water-heated animal blanket in in vivo experiments. Glutamate imaging, MRS, and conventional T2 weighted imaging were performed using the ^{1}H proton volume and surface coil. The B0 field was shimmed using 3D gradient shimming that adjusted high-order gradient shimming currents based on the derived B0 field map. The full width at half maximum were about 15 Hz in phantoms and 20 Hz in rat brains. The RF field and center frequency were calibrated in pre-scan.

Glutamate imaging was obtained using an in-house chemical exchange saturation transfer sequence with a gradient echo (GRE) readout. A rectangular continuous wave with saturation power of 3 μT and duration of 1000 ms was used for pre-saturation of glutamate in the brain. The saturation frequencies were 3 ppm and -3 ppm. Other parameters were: TR/TE = 6.2/2.5 ms,

FA=5°, slice thickness = 2 mm, NEX = 1, FOV = 34 × 34 mm^2, imaging matrix = 64 × 64, and bandwidth = 50 kHz. Total scan time was about 1.4 s for one slice. Z-spectrum was acquired with RF offsets ranging from 1680 Hz to −1680 Hz (5.6 ppm to −5.6 ppm) with an interval of 0.2 ppm. For phantom experiments, the saturation power was varied from 1.5 μT to 6 μT with an interval of 0.5 μT. Other parameters were kept constant. GRE images at two echo times (TE1 = 3.0 ms; TE2 = 4.0 ms) were collected to compute the B0 map. A B1 map was generated by the double-angle method with flip angles of 30° and 60°. An ultra-short echo time stimulated echo acquisition (STEAM) pulse sequence was used for acquisition of proton MRS (TR/TM/TE = 5 000/12.72/2.35 ms; the spectral width = 5 000 Hz; NEX = 320; scan time = 26 min). The single voxel was of dimensions 3 mm × 3 mm × 3 mm and was located to include most of the central thalamus (Fig 3. 1). Water suppression was performed with variable pulse power and optimized relaxation delays. T2-weighted imaging (TR/TE = 2 000/30 ms, NA = 8) was acquired for reference.

The glutamate CEST data was processed using MATLAB 2017a (Mathworks, Natick MA, USA) using in-house software. B0 and B1 inhomogeneity were corrected using B0 and B1 maps generated from the same slice as described in our previous studies(34, 44). The GluCEST contrast was calculated by the following equation(4):

$$\text{GluCEST contrast} = (\text{Mref}(-3\text{ ppm}) - \text{Msat}(+3\text{ ppm})) / \text{Mref}(-3\text{ ppm}).$$

Where Mref (−3 ppm) was the reference images with RF saturation applied at -3 ppm and Msat (+3 ppm) was the label images with RF saturation applied at 3 ppm. In addition, the MRS data was quantified in the magnetic resonance user interface (MRUI) and LCModel. LCModel used

the unsuppressed water peak obtained from the region of interest (ROI) as an internal reference for quantification. Post-processing included phase correction, frequency correction, and metabolite quantification, as described in our previous studies(109, 110).

3.2.5 Statistical analysis

All statistical analyses were performed with SPSS software (Version 22, Chicago, IL). The results were reported as mean ± standard deviation and P values less than 0.05 were considered statistically significant. One-way analysis of variance (ANOVA) and Student's t-test were applied to compare between groups. The correlation between the glutamate image and MRS was measured using Pearson correlation.

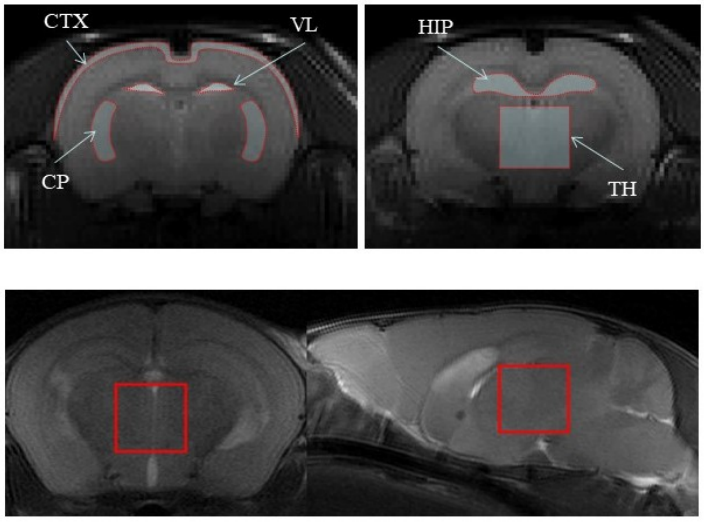

Figure 3. 1 The anatomic structures were identified in T2-weighted images, including the cerebral cortex (CTX), hippocampus (HIP) and thalamus (TH), caudoputamen (CP), lateral ventricle (VL). The red outlines indicate the regions-of-interest used for measurements. In the bottom images, the dimensions of the MRS experiment within the thalamus are shown in the rectangular box in both the coronal and sagittal plane. The area of the thalamus region-of-interest for CEST measures was within the area where MRS was measured.

3.3 Results

3.3.1 Behavioral results of schizophrenia models

In the open-field test, the distance traveled in the central zone (DC) in CPZ group is significantly shorter than that of control (Fig3. 2a) ($P < 0.05$). The total distance traveled (TD) is almost the same between the two groups ($P = 0.48$). The ratio of DC/TD is significantly smaller in the cuprizone-exposed mice than in the controls (Fig3. 2b) ($P < 0.05$). In the Y-maze, the CPZ group present a lower percentage of alternation (PA) than the control (Fig3. 2c) ($P < 0.05$) but not significantly different in the time of arm entrance (AE) (Fig3. 2d) ($P = 0.22$). There is no difference between the two groups in the time in the interaction zone (TI) (Fig3. 2e) ($P = 0.30$).

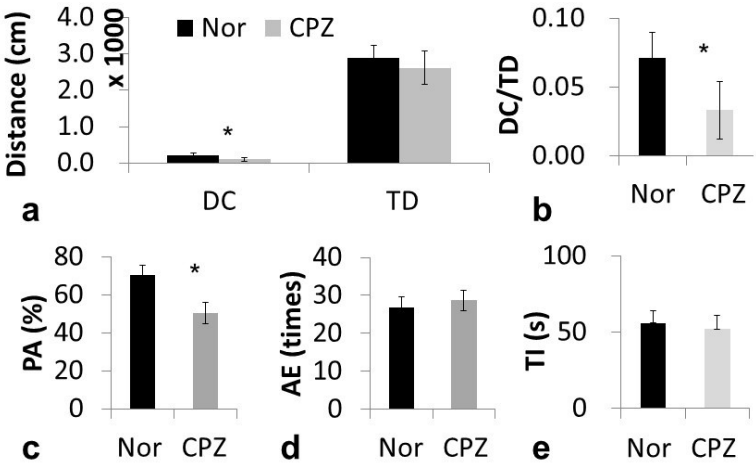

Figure 3. 2 Behavioral results of schizophrenia models. In the open-field test, the distance traveled in the central zone (DC) in CPZ group is significantly shorter than that of control (a) ($P < 0.05$). The total distance traveled (TD) is almost the same between the two groups ($P = 0.48$). The ratio of DC/TD is significantly smaller in the cuprizone-exposed mice than in the controls (b) ($P < 0.05$). In the Y-maze, the CPZ group present a lower percentage

of alternation (PA) than the control (c) ($P < 0.05$) but not significantly different in the time of arm entrance (AE) (d) ($P = 0.22$). There is no difference between the two groups in the time in the interaction zone (TI) (e) ($P = 0.30$).

3.3.2 Glutamate technique

Phantom Z-spectrum and MTR asymmetry plots showed a pronounced glutamate effect at 3 ppm, which was positively correlated with saturation power (Fig. 3.3). The increase rate first rises linearly and slows down after more than 3 μT. Glutamate images of phantoms proved that the signal intensity of the glutamate image is strictly related to glutamate concentration, and linear regression analysis of the glutamate CEST effect versus the concentration shows $R^2 = 0.98$ (Fig. 3.4). Meanwhile, most of the other common neuro metabolites, including MI, Cr, and Cho, contribute negligible glutamate CEST effects. At the same concentration, the signal intensity of GABA is approximately half that of Glutamate.

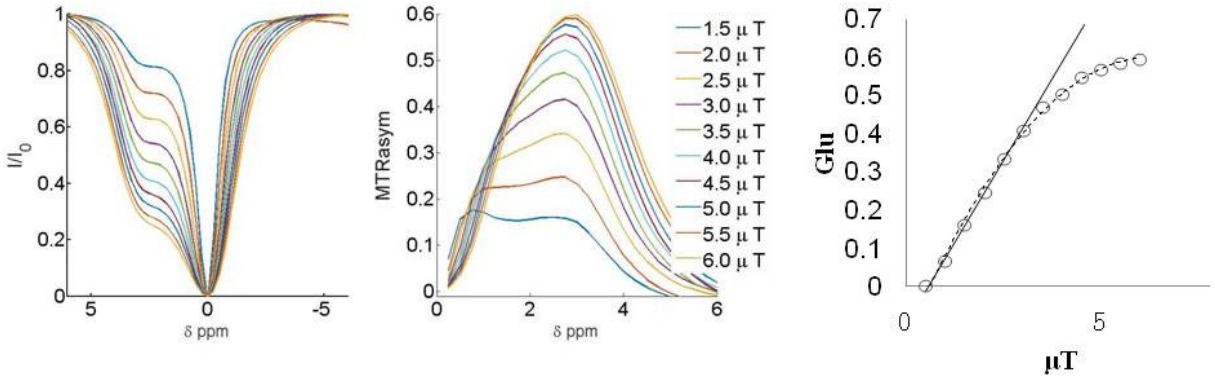

Figure 3. 3 Phantom Z-spectrum (Left) and MTR asymmetry plots (Middle) of Glutamate at different saturation powers. Z-spectrum and MTR asymmetry plots show a pronounced glutamate effect at 3 ppm, which is positively correlated with saturation power. The increased rate first rises linearly and slows down after more than 3 μT (Right).

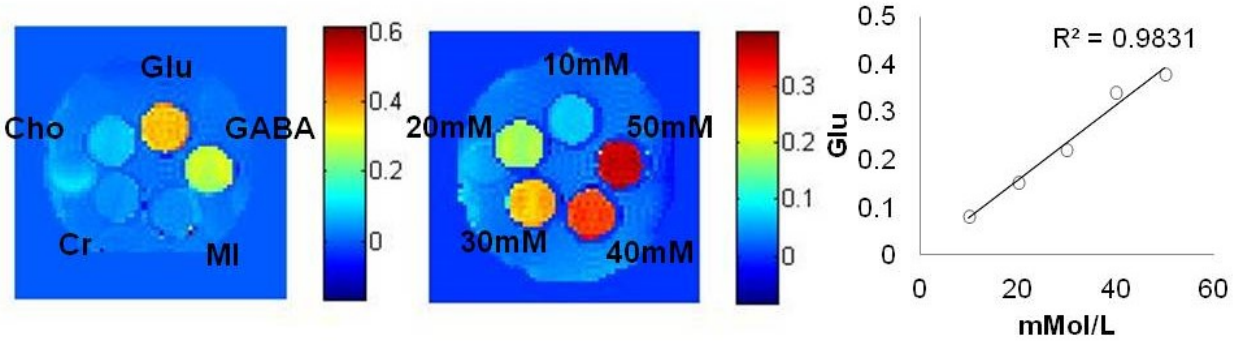

Figure 3. 4 CEST images of phantoms with different glutamate concentration (Middle) and different neuro metabolites at pH of 7.0 (Left). Our results proved that the signal intensity of the glutamate image is strictly related to glutamate concentration, and linear regression analysis of the glutamate CEST effect versus the concentration shows R^2 = 0.98 (Right). Meanwhile, the other common neuro metabolites, including MI, Cr, and Cho, contribute negligible glutamate CEST effects. At the same concentration, the signal intensity of GABA is approximately half that of Glutamate.

3.3.3 MRI of schizophrenia models

There were no lesions in the brain of schizophrenia model in T2-weighted images. (Fig 3.5) The glutamate CEST image could delineate the glutamate concentration in different subtle structures of the brain (Fig 3.6), including hippocampal region (HIP), caudoputamen (CP), cerebral cortex (CTX), lateral ventricle (VL), and thalamus (THA). In the normal brain, the glutamate signal intensity of the gray matter is higher than that of white matter. Compared to controls, glutamate signals of prodromal schizophrenic models increased in the whole brain, especially in the cerebral cortex, hippocampus and thalamus, which were further verified by MRS. In MRS (Water suppression $\geqslant$ 98% and linewidth < 10 Hz), the glutamate concentrations were 6.06 ±

0.28 mmol/L and 5.09 ± 0.43 mmol/L in the prodromal schizophrenia and normal controls, respectively.

Compared to controls, glutamate signals of prodromal schizophrenic models increased in the cerebral cortex (CTX), hippocampus (HIP) and thalamus (TH), and the differences are statistically significant (Fig3.6) ($P < 0.05$). The signal intensity of caudoputamen (CP) is higher in the early stage of schizophrenia but not statistically significant ($P = 0.08$). There is no difference in signal intensity in the lateral ventricle (VL). Linear regression analysis (Fig3.7) shows the glutamate image has excellent correlation with MRS ($R^2 = 0.84$). Pearson correlation coefficient was 0.92 ($P < 0.05$).

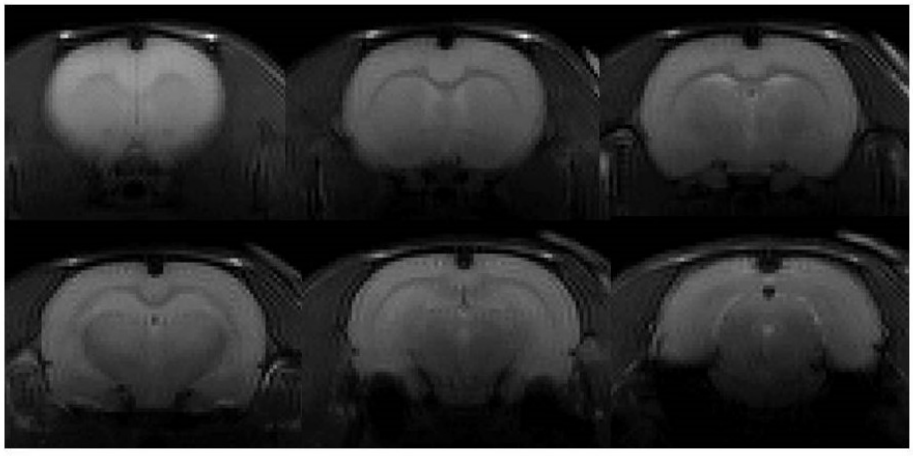

Figure 3. 5 T2 weighted imaging in the whole brain of in early stage of schizophrenia models. Anatomical structures, such as hippocampal region, corpus callosum, and thalamus, etc., are displayed well, but no lesions are diagnosed in the brain.

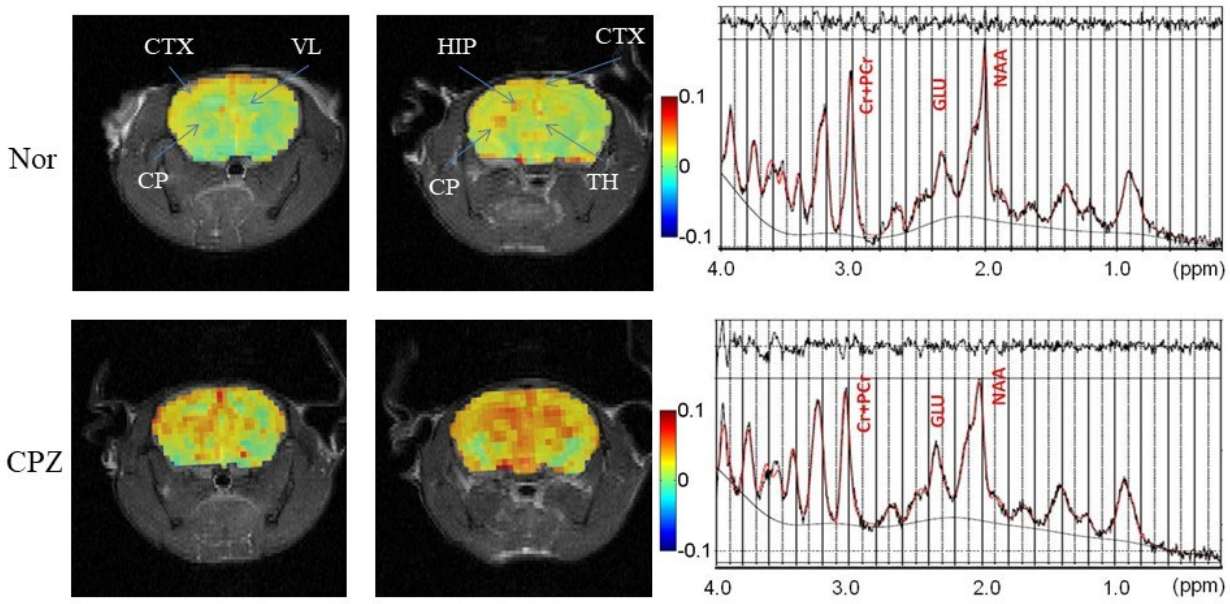

Figure 3. 6 Glutamate image and magnetic resonance spectroscopy (MRS) both in schizophrenia models (Below) and normal control groups (Above). The glutamate CEST image can delineate the glutamate concentration in different subtle structures of the brain, including hippocampal region (HIP), caudoputamen (CP), cerebral cortex (CTX), lateral ventricle (VL), and thalamus (THA). In the control brain, the glutamate signal intensity of the gray matter is higher than that of white matter. Compared to controls, glutamate signals of prodromal schizophrenic models increased in the whole brain, especially in the cerebral cortex, hippocampus and thalamus, which were further verified by MRS. In MRS, the glutamate concentrations were 6.06 ± 0.28 mmol/L and 5.09 ± 0.43 mmol/L in the prodromal schizophrenia and normal controls, respectively.

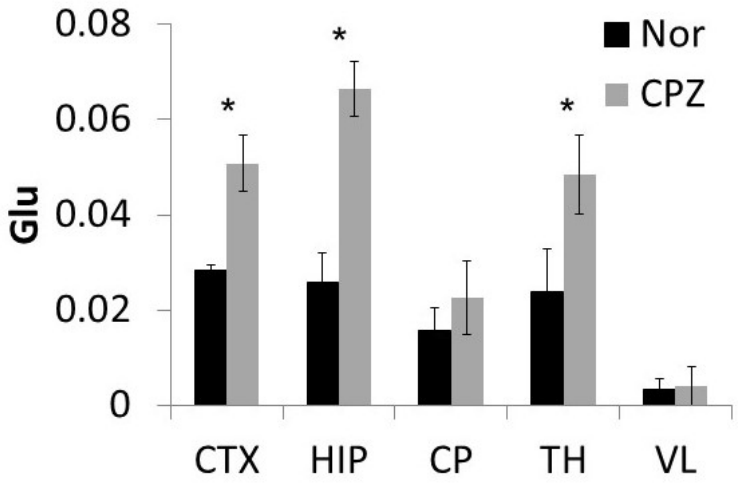

Figure 3. 7 Bar graph of glutamate image signal intensity of different regions of the brain both in schizophrenia (CPZ) and normal control groups (Nor). Compared to controls, glutamate signals of prodromal schizophrenic models increased in the cerebral cortex (CTX), hippocampus (HIP) and thalamus (TH), and the differences are statistically significant ($P < 0.05$). The signal intensity of caudoputamen (CP) is "trending" higher in the early stage of schizophrenic but not statistically significant ($P = 0.08$). There is no difference in signal intensity in the lateral ventricle (VL).

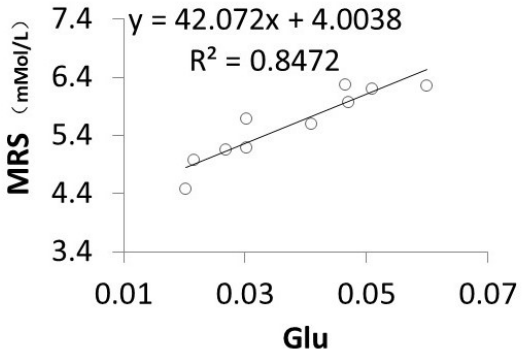

Figure 3. 8 The correlation between glutamate image signal intensity and magnetic resonance spectroscopy (MRS) in the thalamus. Linear regression analysis shows the glutamate image has excellent correlation with MRS ($R2 = 0.84$). Pearson correlation coefficient is 0.92 ($P < 0.05$).

3.4 Discussion

Our study demonstrates the glutamate effect at 3.0 ppm and verifies it using magnetic resonance spectroscopy. The optimal saturation power is critical to the glutamate imaging technique since this effect depends on the power. Increased power increases the glutamate effect, however, the specific absorption rate (SAR) will increase as well. Since SAR is severely restricted in vivo, and the glutamate effect is slowed down after 3μT, we used 3μT as the saturation power in this study, which is confirmed to be feasible by the results both in vivo and in vitro. The deceleration of the glutamate effect at high saturation power is called RF spillover in our previous studies(34, 44). The glutamate distribution in the normal brain in glutamate imaging is consistent with those of previous studies and positron emission tomography, in which the signal intensity of gray matter is higher than white matter(4, 111).

The open-field test results suggest a higher anxiety level and no locomotor activity in the CPZ group, while the Y-maze test suggests that the CPZ group has an impaired spatial working memory. These results are consistent with our previous series of studies on CPZ(107, 112-114). In these studies, we tested the evolution of schizophrenia in CPZ induced models from 1 week to 6 weeks and verified that it is an excellent schizophrenia model both in pathophysiology and behavioral results. Moreover, we also proved that antipsychotic drugs are effective in CPZ induced models (115). At the time of CPZ induction for one week, neurochemical evidence for mitochondrial dysfunction is found in brain cells, which is an essential player in schizophrenia(107). However, only an anxiety-like behavior is found in behavioral tests, but no

effect on the social interaction and spatial working memory. While at 6 weeks, all behavioral tests were abnormal and confirmed to be a mature schizophrenia model(108). Therefore, we believe that the 2-week time window is ideal for this prodromal schizophrenia model.

The escalations of glutamate are observed in the whole brain of schizophrenia models. Glutamate systems are thought to be fundamental to the pathophysiology of schizophrenia(105), which is also supported by recent genetics results(116). However, the results of previous research are not consistent, the majority of studies show increased glutamate, whereas a few report decreased or normal levels(117, 118). These differences may be relevant to the diverse stages of schizophrenia. De La et al. indicated that high glutamate level precedes the onset of schizophrenia(119), which further supports our findings in prodromal schizophrenia. A recent study conducted by Laskaris et al. suggested that the increased glutamate levels in schizophrenia may result from activated microglial cells(120). These findings provide supporting evidence for a putative role of neuroinflammation in prodromal schizophrenia.

In this study, we analyzed four major relevant structures, including hippocampal region (HIP), caudoputamen (CP), cerebral cortex (CTX), and thalamus (THA). Compared to controls, glutamate signals of prodromal schizophrenic models increased in the hippocampus, cerebral cortex, and thalamus. Hippocampus is primarily associated with memory and spatial navigation, and recent studies suppose glutamate dysfunction beginning in the CA1 region of the hippocampus as inducing attenuated psychotic symptoms(121). The cerebral cortex is reported to be involved in young relatives at risk for schizophrenia (122), so the increase of

glutamate may help explain neurocognitive deficits in prodromal stage. Furthermore, the evidence of increased glutamate in the thalamus is also found in our previous studies in full-blown schizophrenia models based on MRS technique(108), indicating thalamus disorder is continuous throughout the evolution of schizophrenia.

MRS is the most recognized technique of non-invasive detection of glutamate in vivo, before the emergence of glutamate CEST imaging, and the linear combination model (LCModel) is a powerful tool for quantifying the absolute concentration of MRS(109). Our previous works quantified the neuro metabolites during the early stage of CPZ-exposure and discover the significantly decreased levels of NAA and PCr in the thalamus and hippocampus(107). This study quantifies the glutamate concentration in thalamus, which is 6.06 ± 0.28 mmol/L in prodromal schizophrenia and 5.09 ± 0.43 mmol/L in normal controls. These results have excellent correlation with glutamate imaging results.

Although glutamate CEST imaging has gradually become a research hotspot in neuropsychiatric diseases in recent years, the correlation between glutamate imaging and MRS has not yet been explored (67, 69). Our study demonstrates the Pearson correlation coefficient is 0.92, which further verifies the reliability of the glutamate image. The non-zero y-intercept suggests a relatively low signal intensity of glutamate image, which may be due to the interference with the nuclear Overhauser effect in -3 ppm (48). However, compared to MRS, the advantage of this technique is the simultaneous detection of glutamate changes in multiple regions. Hence, it can provide a more comprehensive analysis of the brain.

The major limitation of this study is that the signal intensity is affected by GABA. Our previous study has proved the CEST effect of GABA in brain tumor, and other researchers also report that about 25–30% signal intensity of the glutamate image comes from Cr, GABA, and other macromolecules(4, 123). Therefore, further optimization is required in future studies. However, since the concentration of glutamate is about ten times than that of the GABA in the brain, one can be sure that the image is dominated by glutamate.

In conclusion, our study demonstrates that the glutamate image is a dependable technique and has excellent correlation with MRS. We further apply this technique in prodromal schizophrenic models and demonstrate that glutamate changes in different regions of the brain, which is expected to be a powerful indicator of the diagnosis of schizophrenia prodrome.

Reference

1. Larson MK, Walker EF, Compton MT. Early signs, diagnosis and therapeutics of the prodromal phase of schizophrenia and related psychotic disorders. Expert review of neurotherapeutics. 2010;10(8):1347-59.

2. van der Gaag M, Smit F, Bechdolf A, French P, Linszen DH, Yung AR, McGorry P, Cuijpers P. Preventing a first episode of psychosis: meta-analysis of randomized controlled prevention trials of 12 month and longer-term follow-ups. Schizophrenia research. 2013;149(1):56-62.

3. Chan MK, Krebs M, Cox D, Guest P, Yolken R, Rahmoune H, Rothermundt M, Steiner J, Leweke F, Van Beveren N. Development of a blood-based molecular biomarker test for identification of schizophrenia before disease onset. Translational psychiatry. 2015;5(7):e601.

4. Fusar-Poli P, Carpenter W, Woods S, McGlashan T. Attenuated psychosis syndrome: ready for DSM-5.1? Annual review of clinical psychology. 2014;10:155-92.

5. Cai K, Haris M, Singh A, Kogan F, Greenberg JH, Hariharan H, Detre JA, Reddy R. Magnetic resonance imaging of glutamate. Nature Medicine. 2012;18(2):302-6. doi: 10.1038/nm.2615.

6. Davis KA, Nanga RPR, Das S, Chen SH, Hadar PN, Pollard JR, Lucas TH, Shinohara RT, Litt B, Hariharan H. Glutamate imaging (GluCEST) lateralizes epileptic foci in nonlesional temporal lobe epilepsy. Science translational medicine. 2015;7(309):309ra161-309ra161.

7. Pépin J, Francelle L, Carrillo-de Sauvage M-A, de Longprez L, Gipchtein P, Cambon K, Valette J, Brouillet E, Flament J. In vivo imaging of brain glutamate defects in a knock-in mouse model of Huntington's disease. NeuroImage. 2016;139:53-64.

8. Bagga P, Crescenzi R, Krishnamoorthy G, Verma G, Nanga RPR, Reddy D, Greenberg J, Detre JA, Hariharan H, Reddy R. Mapping the alterations in glutamate with GluCEST MRI in a mouse model of dopamine deficiency. Journal of Neurochemistry. 2016;139(3):432-9.

9. Haris M, Singh A, Mohammed I, Ittyerah R, Nath K, Nanga RPR, Debrosse C, Kogan F, Cai K, Poptani H. In vivo magnetic resonance imaging of tumor protease activity. Scientific reports. 2014;4:6081.

10. Merritt K, Egerton A, Kempton MJ, Taylor MJ, McGuire PK. Nature of Glutamate Alterations in Schizophrenia: A Meta-analysis of Proton Magnetic Resonance Spectroscopy Studies. JAMA psychiatry. 2016;73(7):665-74. Epub

2016/06/16. doi: 10.1001/jamapsychiatry.2016.0442. PubMed PMID: 27304221.

11. Howes O, McCutcheon R, Stone J. Glutamate and dopamine in schizophrenia: an update for the 21st century. Journal of psychopharmacology. 2015;29(2):97-115.

12. Roalf DR, Nanga RPR, Rupert PE, Hariharan H, Quarmley M, Calkins ME, Dress E, Prabhakaran K, Elliott MA, Moberg PJ. Glutamate imaging (GluCEST) reveals lower brain GluCEST contrast in patients on the psychosis spectrum. Molecular psychiatry. 2017;22(9):1298.

13. Xuan Y, Yan G, Peng H, Wu R, Xu H. Concurrent changes in 1H MRS metabolites and antioxidant enzymes in the brain of C57BL/6 mouse short-termly exposed to cuprizone: Possible implications for schizophrenia. Neurochemistry international. 2014;69:20-7.

14. Yan G, Xuan Y, Dai Z, Shen Z, Zhang G, Xu H, Wu R. Brain metabolite changes in subcortical regions after exposure to cuprizone for 6 weeks: potential implications for schizophrenia. Neurochemical research. 2015;40(1):49-58.

15. Sun PZ, Wang Y, Dai ZZ, Xiao G, Wu RH. Quantitative chemical exchange saturation transfer (qCEST) MRI - RF spillover effect-corrected omega plot for simultaneous determination of labile proton fraction ratio and exchange rate. Contrast Media & Molecular Imaging. 2014;9(4):268-75. doi: 10.1002/cmmi.1569. PubMed PMID: WOS:000333825300002.

16. Wu R, Xiao G, Zhou IY, Ran C, Sun PZ. Quantitative chemical exchange saturation transfer (qCEST) MRI - omega plot analysis of RF-spillover-corrected inverse CEST ratio asymmetry for simultaneous determination of labile proton ratio and exchange rate. NMR Biomed. 2015;28(3):376-83.

17. Ametamey SM, Treyer V, Streffer J, Wyss MT, Schmidt M, Blagoev M, Hintermann S, Auberson Y, Gasparini F, Fischer UC. Human PET studies of metabotropic glutamate receptor subtype 5 with 11C-ABP688. Journal of Nuclear Medicine. 2007;48(2):247-52.

18. Xu H, Yang H-J, Zhang Y, Clough R, Browning R, Li X-M. Behavioral and neurobiological changes in C57BL/6 mice exposed to cuprizone. Behavioral neuroscience. 2009;123(2):418.

19. Xu H, Yang H, McConomy B, Browning RA, Li X-M. Behavioral and neurobiological changes in C57BL/6 mouse exposed to cuprizone: effects of antipsychotics. Frontiers in Behavioral Neuroscience. 2010;4:8.

20. Xu H, Yang H-J, Rose GM, Li X-M. Recovery of behavioral changes and compromised white matter in C57BL/6

mice exposed to cuprizone: effects of antipsychotic drugs. Frontiers in behavioral neuroscience. 2011;5:31.

21. Xu H, Yang H-J, Li X-M. Differential effects of antipsychotics on the development of rat oligodendrocyte precursor cells exposed to cuprizone. European archives of psychiatry and clinical neuroscience. 2014;264(2):121-9.

22. Ripke S, Neale BM, Corvin A, Walters JT, Farh K-H, Holmans PA, Lee P, Bulik-Sullivan B, Collier DA, Huang H. Biological insights from 108 schizophrenia-associated genetic loci. Nature. 2014;511(7510):421.

23. Kahn R, Sommer I. The neurobiology and treatment of first-episode schizophrenia. Molecular psychiatry. 2015;20(1):84.

24. Merritt K, McGuire P, Egerton A. Relationship between Glutamate Dysfunction and Symptoms and Cognitive Function in Psychosis. Frontiers in psychiatry. 2013;4:151. Epub 2013/12/11. doi: 10.3389/fpsyt.2013.00151. PubMed PMID: 24324444; PubMed Central PMCID: PMCPmc3840324.

25. De La Fuente-sandoval C, León-Ortiz P, Favila R, Stephano S, Mamo D, Ramírez-Bermúdez J, Graff-Guerrero A. Higher levels of glutamate in the associative-striatum of subjects with prodromal symptoms of schizophrenia and patients with first-episode psychosis. Neuropsychopharmacology. 2011;36(9):1781.

26. Laskaris L, Di Biase M, Everall I, Chana G, Christopoulos A, Skafidas E, Cropley V, Pantelis C. Microglial activation and progressive brain changes in schizophrenia. British journal of pharmacology. 2016;173(4):666-80.

27. Lieberman J, Girgis R, Brucato G, Moore H, Provenzano F, Kegeles L, Javitt D, Kantrowitz J, Wall M, Corcoran C. Hippocampal dysfunction in the pathophysiology of schizophrenia: a selective review and hypothesis for early detection and intervention. Molecular psychiatry. 2018.

28. Bhojraj TS, Sweeney JA, Prasad KM, Eack SM, Francis AN, Miewald JM, Montrose DM, Keshavan MS. Gray matter loss in young relatives at risk for schizophrenia: relation with prodromal psychopathology. Neuroimage. 2011;54:S272-S9.

29. Yang ZX, Huo SS, Cheng XF, Xu ZF, Cao Z, Zeng JX, Xiao YY, You KZ, Chen W, Liu YY, Wu RH. Quantitative multivoxel proton MR spectroscopy study of brain metabolites in patients with amnestic mild cognitive impairment: a pilot study. Neuroradiology. 2011:1-8.

30. Yan G, Zhang T, Dai Z, Yi M, Jia Y, Nie T, Zhang H, Xiao G, Wu R. A Potential Magnetic Resonance Imaging Technique Based on Chemical Exchange Saturation Transfer for In Vivo γ-Aminobutyric Acid Imaging. PloS one. 2016;11(10):e0163765.

Chapter 4

Amide proton transfer in amyotrophic lateral sclerosis: an imaging biomarker of ALS

Abstract

Amyotrophic lateral sclerosis (ALS) is a progressive, fatal disease characterized by the death of neurons controlling voluntary muscle movement. There is a lack of objective imaging indicators for ALS diagnosis and assessment. Amide proton transfer (APT) is a novel imaging technique that can detect amide metabolic changes in the brain. This study aims to explore the value of APT in ALS patients as a possible image biomarker of disease and the correlation between APT and diffusion tensor imaging (DTI). 32 participants were recruited, including 16 ALS patients and 16 healthy controls. Amide proton transfer imaging and DTI were performed of the brain at 3T. Conventional T1- and T2-weighted images as well as radiofrequency and static magnetic field maps were also obtained. Analysis of covariance for APT were calculated between patients and healthy controls, and between different regions within ALS patients. The correlations between APT and diffusion parameters were also measured. Within ALS patients, the amide peak intensity was significantly different between the motor cortex and other grey matter territories. Compared with healthy controls, the APT signal intensities in ALS were significantly reduced in motor cortex ($P < 0.001$) and corticospinal tract ($P = 0.046$), which was undetectable under routine imaging methods. There were no statistical differences in temporal cortex ($P = 0.449$) and medulla ($P = 0.342$) between patients and controls in APT values. Compared with the healthy control group, fractional anisotropy (FA) values were reduced in both the corticospinal

tract (P = 0.024) and temporal white matter (P = 0.001) in ALS patients. Apparent diffusion coefficient (ADC) was increased in motor cortex (P = 0.008), and the corticospinal tract (P = 0.013) in ALS patients. In addition, APT was negatively correlated with FA (r = -0.477, P= 0.006) and positively correlated with ADC (r = 0.629 and P < 0.001). To our knowledge, this is the first study demonstrating changes of APT in the motor cortex and corticospinal tract of ALS patients, which has the potential to be an objective imaging biomarker for ALS diagnosis. The combination of APT and DTI can simultaneously detect changes of metabolism and microstructure in ALS patients.

4.1 Introduction

Amyotrophic lateral sclerosis (ALS) is a progressive, fatal disease characterized by the death of neurons controlling voluntary muscle movement(124, 125). Symptom onset often begins with muscle weakness and the average life span is 3 to 5 years(126). Despite it first being described more than a century ago by Jean-Martin Charcot, ALS remains a condition without effective disease modifying treatment (127). The current diagnosis of ALS mainly relies on the El Escorial criteria(128), which necessitates lengthy investigations to rule out other conditions and neuromuscular disorders. ALS is difficult to diagnose early due partly to the subjective nature of the neurological assessment and a lack of objective indicators of cerebral involvement (129). Therefore, an objective imaging technique is urgently needed for the diagnosis of ALS.

Amide proton transfer (APT) is a novel imaging technique which can detect amide metabolic changes in the microenvironment(2, 40). An amide is any organic compound containing the group -NH_2, which is widely found in various proteins in vivo. The change of amide can be a critical indicator for diverse diseases such as tumor and stroke(3, 41). The theory of APT is dependent on chemical exchange saturation transfer(130, 131), in which an off-resonance irradiation pulse is used to specifically saturate the amide hydrogen, then the saturation effect will transfer to the water molecule through chemical exchange phenomenon(42). Amide metabolism can then be imaged indirectly by examining the water proton signal. Based on the cascade amplification of chemical exchange, APT images usually have excellent performance in sensitivity and spatial resolution compared to other metabolic methods such as MR spectroscopy

(43-45). Moreover, the in vivo homeostasis is not disturbed by contrast agent administration since APT relies on endogenous contrast (46).

Our hypothesis is that amide is altered due to neurodegeneration in ALS, and this alteration will be visible on APT images. This study aims to explore the value of APT in ALS patients as a possible image biomarker of disease and the correlation between APT and diffusion tensor imaging (DTI). DTI is commonly used in ALS research studies, and our previous results demonstrate that DTI can provide in vivo evidence of intracranial degeneration of the corticospinal tract in ALS(132-134). The combination of APT and DTI may simultaneously detect changes in metabolism and microstructure.

4.2 Methods

4.2.1 Subjects

This study had institutional review board approval, and written informed consent was obtained from all subjects. Thirty-two participants from July 2017 to July 2018 were recruited as part of the Canadian ALS Neuroimaging Consortium (CALSNIC), including 16 ALS patients (7 men and 9 women; mean age = 64.5 years) and 16 healthy controls (6 men and 10 women; mean age = 52.0 years). Among ALS patients, six subjects were diagnosed as possible ALS, eight were probable, and two were definite, according to the revised El Escorial criteria. Clinical details and demographics of the patients were provided in Table 1. Disease duration ranged from 7 to 47 months (mean 25.45 months, SD 11.81). Disease severity was assessed using the ALS Functional Rating Scale-Revised (ALSFRS-R)(135), and ranged from 32 to 47 (mean 38.13, SD 6.03) in the patients. The maximum score was 48, with lower scores associated with greater disability. The rate of disease progression ranged from 0.05 to 1.19 (mean 0.43 months, SD 0.31) and was calculated by the following formula: Disease progression = (48 - ALSFRS-R) / Disease duration.

4.2.2 MR imaging protocol

Brain MR imaging was performed on a 3T Siemens Prisma using a 64-channel receive head coil. Amide proton transfer imaging, diffusion tensor imaging, routine T1- and T2-weighted image, as well as the flip angle map were obtained. The APT sequence was modified from a standard

gradient echo sequence, by adding a series of specific pre-saturation pulses at the beginning of the sequence to enable APT. Saturation power was 0.8 μT. Total saturation time was 3000 ms with duty cycle = ~94%. Saturation frequency offset ranged from -10 ppm to 10 ppm with interval of 0.25 ppm. Water saturation shift reference (WASSR) images were collected from -1 to 1 ppm with interval of 0.1 ppm. The single oblique coronal slice for APT was prescribed to maximize inclusion of the corticospinal tract, using both T1-weighted and DTI trace images for reference and angling with an 8° rotation from perpendicular to the anterior-posterior commissure line. Other parameters included: TR = 5000 ms; TE = 1.31 ms; centric phase encoding; slice thickness = 6 mm; number of averages =1; FOV = 192 × 192 mm^2; matrix = 128 × 128. Parameters for DTI were: TR = 8000 ms; TE = 60 ms; slice thickness = 2 mm (no gap); number of averages =1; matrix = 128 × 128; b-value = 1000 s/mm^2; diffusion-encoding gradients applied in 30 noncollinear directions.

4.2.3 Data post-processing

All image data were processed in Matlab using in-house software. The Z-spectrum was plotted by normalizing the different offset images to the thermal-equilibrium image. A B0 map was generated and calibrated by the WASSR technique(36). We used Lorentz fitting to calculate the APT effect in the Z-spectrum. Five peaks including amide, amine, nuclear Overhauser effect (NOE), water, and magnetization transfer (MT) were fitted, and the APT image was derived by the integral area under the amide peak. For diffusion, Fractional Anisotropy (FA) and Apparent Diffusion Coefficient (ADC) maps were generated by the default processing in the scanner. FA

was calculated as the normalized variance of the three eigenvalues (λ_1, λ_2, and λ_3). The formula was as follows:

$$FA = \sqrt{\frac{1}{2}} \frac{\sqrt{(\lambda_1 - \lambda_2)^2 + (\lambda_1 - \lambda_3)^2 + (\lambda_2 - \lambda_3)^2}}{\sqrt{({\lambda_1}^2 + {\lambda_2}^2 + {\lambda_3}^2)}}$$

ADC values were calculated on a voxel-by-voxel basis as the follows: ADC = ($1/b$) × −In($S/S0$), where S0 and S were the signal intensities of each voxel obtained with b-values of 0 and 1000 s/mm^2, respectively. The anatomical structures were identified in conventional T2- and T1-weighted images.

4.2.4 Statistics

Statistical analysis was performed on SPSS 24.0 (IBM, Armonk, NY). The normal distribution test was performed on each parameter first, and all parameters were confirmed to be the normal distribution. Then, analysis of covariance (ANCOVA) was used to compare APT, FA, and ADC between patients and healthy controls, and in different regions within ALS patients. The correlation between APT and ADC, APT and FA were also measured in white matter using Pearson correlation in SPSS. The results were reported as mean ± standard deviation and p values less than 0.05 were considered statistically significant.

Table 1 The demographics and clinical profile of the participants

Variables	ALS (n=16)	Control (n=16)
Demographics		
Age (mean ± SD)	64.5±8.74	52.0±8.61
Sex (M/F)	7/9	6/10
El Escorial		
possible	6	n/a
probable	8	n/a
definite	2	n/a
Duration (months)	25.45±11.81	n/a
Progression Rate (mean ± SD)	0.43±0.31	n/a
ALSFRS-R Score (mean ± SD)	38.13±6.03	n/a

4.3 Results

Five peaks including amide, amine, nuclear Overhauser effect (NOE), water, and magnetization transfer (MT) were detected in the Z-spectrum of the motor cortex and temporal cortex (which served as a control region) in healthy controls and ALS patients, and each peak could be appropriately fitted using Lorentz fitting (Figure 4.1). The amide peak was evident at around 3.5 ppm. In ALS patients, amide peaks were significantly different between motor cortex and temporal cortex, whereas they remained unchanged in the control group.

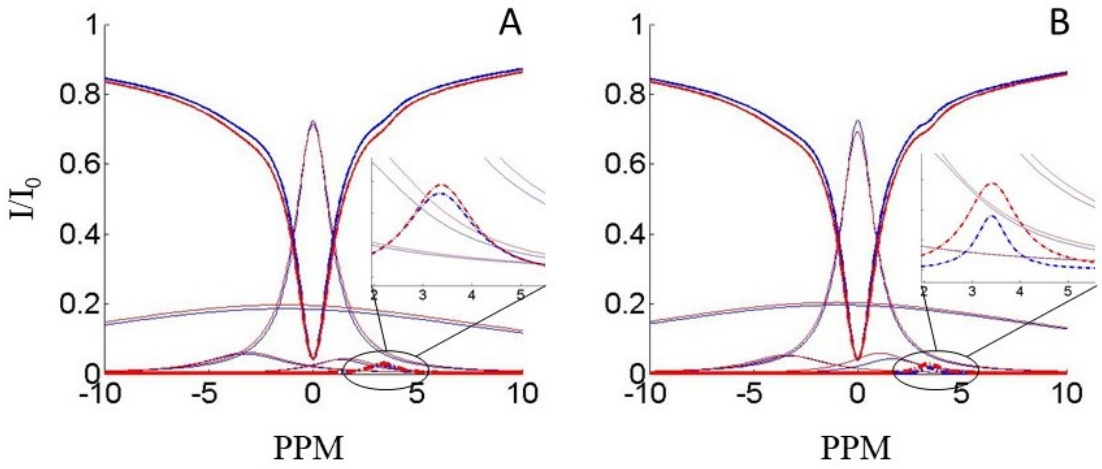

Figure 4. 1 The Z-spectrum of motor cortex (blue) and control temporal cortex (red) in the healthy control group (A) and ALS patients (B). Five peaks were detected in the Z-spectrum, and each peak could be appropriately fitted using Lorentz fitting. Amide peak was evident and detectable at around 3.5 ppm (zoomed-in region). In ALS patients (B), amide peaks were significantly different between motor cortex and control cortex, whereas they remained constant in control group (A).

The normalized images (I/I_0 images) of the oblique coronal brain slice corrected for B0 inhomogeneities are shown in Figure 4.2. At low saturation power (0.8 μT), the main contamination factor was B0 inhomogeneity, which was well corrected using WASSR methods. Comparing the normalized images before and after correction, the homogeneity of corrected image was significantly improved.

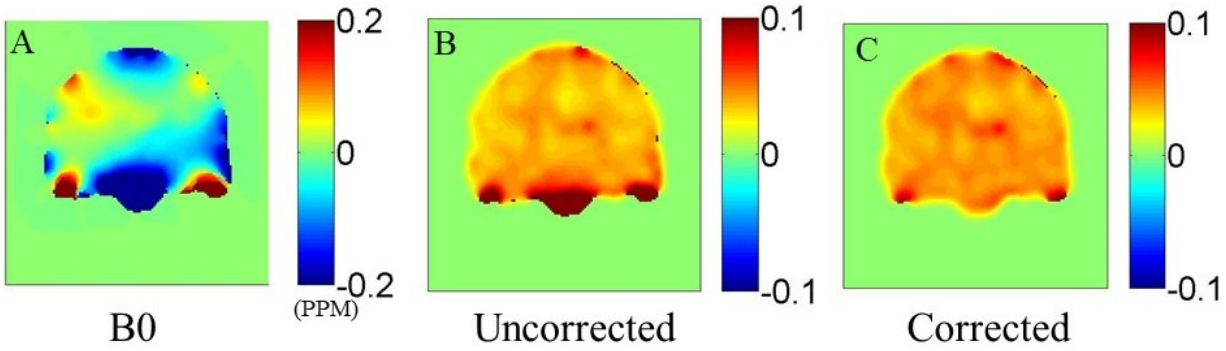

Figure 4. 2 The B0 map and the correction of normalized images. At low saturation power (0.8 μT), the main contamination factor is B0 inhomogeneity (A), which is well corrected using WASSR methods. Comparing the normalized images before (B) and after (C) correction, the homogeneity of corrected image is significantly improved.

There were no observable lesions in the ALS patients in conventional T2- and T1-weighted images, and differences between the ALS and healthy control are not visibly evident (Figure 4.3). However, in the APT images, geographic differences were noticeable both within the same ALS subject and between the ALS patient and the healthy control. The APT signal intensity of motor cortex was significantly reduced in ALS patients.

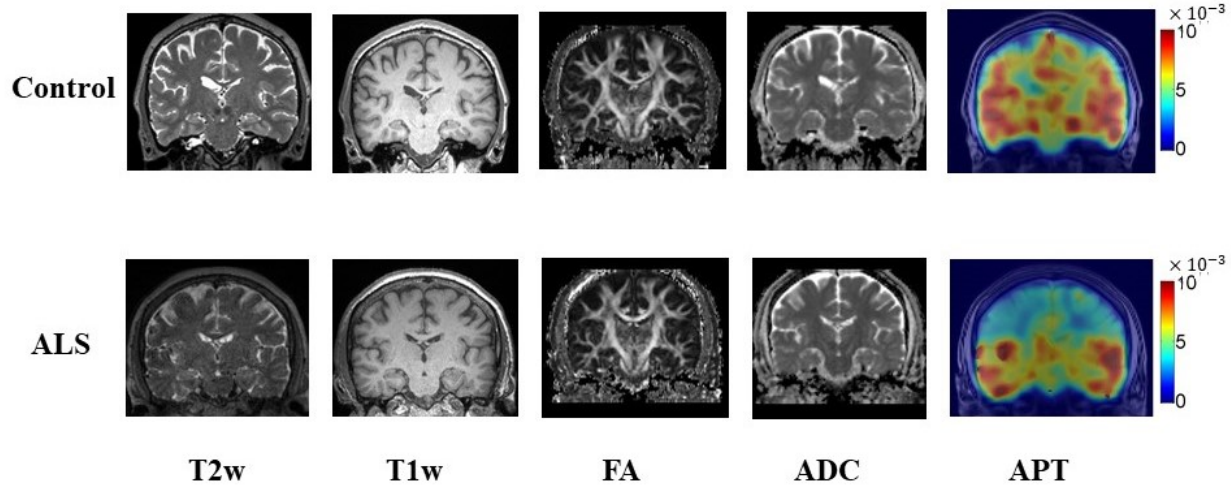

Figure 4. 3 Conventional T2- and T1-weighted images, DTI, and APT are shown in both healthy control group and ALS patients. There were no observable lesions in the ALS patient in conventional images. Even in FA and ADC images, ALS and healthy control group could not see a significant difference. However, in the APT images, the differences were noticeable both within the same ALS and between the ALS patients and the healthy controls. The APT signal intensity of motor cortex was significantly degraded in ALS patients.

Group differences in APT signal intensity in ALS and controls is shown in Figure 4.4. In the ALS group, the APT signal intensity of motor cortex (MC) was significantly reduced compared with those of the temporal cortex (TC) ($P < 0.001$). Similarly, a decrease was observed in the corticospinal tract (CT) when compared with the temporal white matter (TW) ($P < 0.001$). Compared with healthy controls, the APT signal intensities were also significantly reduced both in motor cortex ($P < 0.001$) and in corticospinal tract ($P = 0.046$). In contrast, there were no statistical differences in temporal cortex ($P = 0.449$) and temporal white matter ($P = 0.342$) between patients and controls in the APT image.

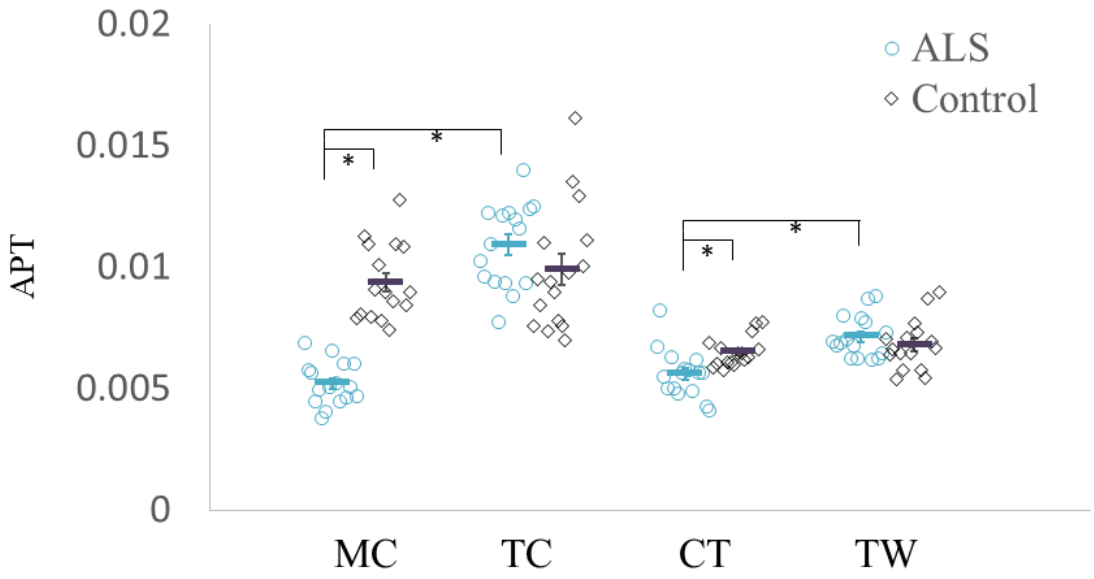

Figure 4. 4 The dot plots of APT signal intensity in ALS and controls. In the same ALS patients, the APT signal intensity of motor cortex (MC) was significantly reduced compared with those of the temporal cortex (TC) ($P < 0.001$). The consistent decrease was observed in the corticospinal tract (CT) when compared with the temporal white matter (TW) ($P < 0.001$). Compared with healthy controls, the APT signal intensities were also significantly reduced both in

motor cortex (P < 0.001) and in corticospinal tract (P = 0.046). In contrast, there were no statistical differences in temporal cortex (P = 0.449) and medulla (P = 0.342) between patients and controls in the APT image.

Figure 4.5 shows group differences in FA and ADC. Compared with the healthy control group, FA was reduced in both corticospinal tract (CT) (P = 0.024) and temporal white matter (TW) (P = 0.001) in ALS patients. Meanwhile, ADC values were increased in motor cortex (MC) (P = 0.008) and corticospinal tract (CT) (P = 0.013) in ALS patients. APT was negatively correlated with FA and positively correlated with ADC in the white matter (Figure 6). The Pearson correlation between FA and APT was -0.477, P = 0.006. There was a greater correlation between ADC and APT, with Pearson correlation of 0.629 and P < 0.001.

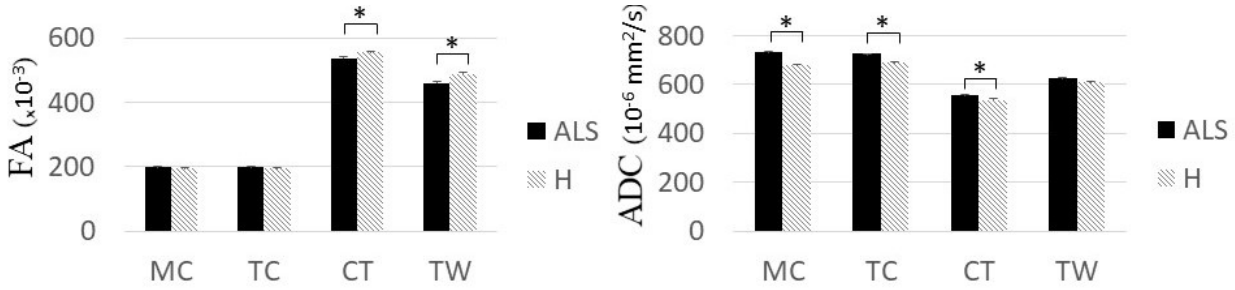

Figure 4. 5 The histogram of FA (left) and ADC (right) signal intensities in ALS and controls. Compared with the healthy control group, FA values were declined in both corticospinal tract (CT) (P = 0.024) and temporal white matter (TW) (P = 0.001) in ALS patients. Meanwhile, ADC values were increased in motor cortex (MC) (P = 0.008) and corticospinal tract (CT) (P = 0.013) in ALS patients.

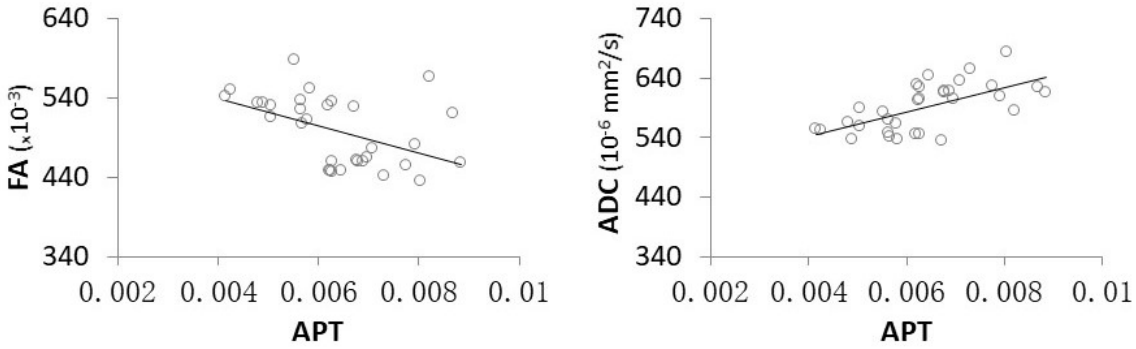

Figure 4. 6 The correlation both between APT and FA (left) and between APT and ADC (right) in the white matter. APT was negatively correlated with FA and positively correlated with ADC. The Pearson correlation between FA and APT was -0.477, P = 0.006. There was a greater correlation between ADC and APT, with Pearson correlation of 0.629 and P < 0.001.

4.4 **Discussion**

In this study, the amide proton transfer technique was applied in ALS patients. As anticipated, APT was abnormal in the motor cortex and corticospinal tract in ALS, whereas conventional structural imaging was normal. In addition, the correlation between APT and DTI was explored, revealing that APT is negatively correlated with FA and positively correlated with ADC.

The finding of a reduced amide peak in the motor cortex and corticospinal tract in ALS patients has not been previously reported. Amide proton transfer was proposed by Zhou et al., and has proven to be a versatile technique for imaging metabolic change in neurological disease(3, 40). The change of amide peak in APT usually represents the alteration of intracellular protein, which has an intimate relationship with cell activation and proliferation. This correlation is confirmed by Togao et al. who used APT imaging to predict the histopathological grades of adult diffuse gliomas(136). Park et al. also discovered that APT could be a proliferation indicator and was superior to MR spectroscopy(137). Further analysis found the positive correlation between APT and MR-spectroscopy derived choline. Since choline is a marker of cell membrane synthesis, it further supports that APT can be an indicator of cell activation. Although the actual type of amide loss caused by neuron death remains to be determined, previous studies supposed that it may be mediated by specific signaling pathways such as programmed cell death(138).

The alteration of amide may also be due to the metabolic reprogramming in ALS. Szelechowski et al recently found that a total of 206 proteins in the SODG93A ALS model were inhibited in motor neurons in contrast to wild-type mice(139), which may account for the amide decrease in APT. Two major effector proteins of necroptosis are receptor-interacting serine/threonine-protein kinase 1 (RIPK1) and mixed-lineage kinase domain–like (MLKL), and RIPK1 mediates axonal degeneration was observed in ALS patients(140, 141). Therefore, further specific protein research in APT might uncover the exact mechanisms in ALS. In addition, protein folding, which is reported to be perturbed in ALS-associated SOD1 mutants(142, 143), is also described to affect the signal of Z-spectrum(144).

The cerebral pathologic hallmark of ALS is the loss of upper motor neurons in the motor cortex, axonal degeneration of the corticospinal tract and lower motor neurons in the brain stem(145). In agreement with pathologic findings and previous DTI studies, the decrease of FA and increase of ADC were found in the corticospinal tract in ALS patients(129, 146). Both the reduction of FA and increase in ADC reflect damage of axons and/or myelin of white matter fiber tracts. We also detected FA decrease in temporal white matter, which supports the view of widespread involvement of the cerebral white matter in ALS(147). In the motor cortex, ADC values increase significantly in ALS, while FA values remained essentially unchanged. This phenomenon is consistent with APT results and demonstrate the loss of giant pyramidal Betz cells and astrogliosis in motor cortex in ALS patients. Mutual confirmations are provided by motor cortex thinning in voxel-based morphometry(148) and reduced N-acetylaspartate in MR spectroscopy(149). Conventional T2-weighted image and T1-weighted image are negative which may be contributed by the low sensitivity(150).

Another important finding is the correlation between APT and DTI. We observed a negative correlation between APT and FA and positive correlation between APT and ADC. Previous studies indicate that ADC correlated with disease duration while FA correlated with disease severity in ALS patients(149). Since APT is more closely related to ADC, the results may prompt that APT is more relevant to disease duration. Moreover, multimodality imaging can leverage full features of these two imaging techniques. The combination of APT and DTI may provide a unique tool to detect neurochemical and microstructure simultaneously.

Note that the post-processing of APT is different to previous studies, which using an MTR asymmetry method to represent APT. Although MTR asymmetry is commonly used in APT studies, it has some intrinsic defects that will affect its accuracy(151). First, the MTR asymmetry analysis is based on the assumption that the MT effect is symmetric on both sides of the water, which has been proved to be untrue in many studies (152). Second, the Nuclear Overhauser effect is evident in vivo and will contaminate the APT signal intensity in MTR asymmetry analysis(48). The advantage of Lorentz fitting is overcoming all the above problems(31), and even further excluding the interference of other metabolites in vivo, to more accurately reflect changes in amide.

There are some limitations in our study and some expectations for future research. First, we only explored the APT performance in a single disease. Further comparison of different diseases with similar symptoms to ALS such as primary lateral sclerosis, progressive bulbar palsy, and disease

mimics is useful and necessary. Patients with early disease and suspected ALS will need to be studied to determine if APT can aid in early diagnosis. In addition, the sample size is relatively small, and some significances may have been overestimated. Finally, methodologies related to DTI can be improved. Due to the bending and intersection of fiber bundles, the assumption of Gaussian distribution in DTI is imprecise in the human brain (153). In contrast, new diffusion techniques such as diffusion kurtosis imaging provide a more objective and accurate quantification of the microstructure using a model of diffusional non-Gaussianity(154).

In conclusion, changes in the motor cortex and corticospinal tract in ALS were detected using APT imaging for the first time, which may have the potential to be an objective imaging biomarker for ALS diagnosis. The combination of APT and DTI can simultaneously detect changes of metabolism and microstructure in ALS patients.

4.5 Acknowledgment

Grateful acknowledgment is made to Dr. Mark D Pagel from MD Anderson Cancer Center and Dr. Edward A. Randtke from University of Arizona for technical assistance with pulse sequence implementation. This study was supported in part by grants from Canadian Institutes of Health, the ALS Society of Canada and Brain Canada, the Natural Science Foundation of China (NSFC 81471730, 31870981), and the Natural Science Foundation of Guangdong Province (2018A030307057).

References

1. Kiernan MC, Vucic S, Cheah BC, Turner MR, Eisen A, Hardiman O, Burrell JR, Zoing MC. Amyotrophic lateral sclerosis. The Lancet. 2011;377(9769):942-55.

2. Peters OM, Ghasemi M, Brown RH. Emerging mechanisms of molecular pathology in ALS. The Journal of clinical investigation. 2015;125(5):1767-79.

3. McCampbell A, Cole T, Wegener AJ, Tomassy GS, Setnicka A, Farley BJ, Schoch KM, Hoye ML, Shabsovich M, Sun L. Antisense oligonucleotides extend survival and reverse decrement in muscle response in ALS models. Journal of Clinical Investigation. 2018;128(8):3558-67.

4. Scott A. Drug therapy: On the treatment trail for ALS. Nature. 2017;550(7676):S120-s1. Epub 2017/10/19. doi: 10.1038/550S120a. PubMed PMID: 29045376.

5. Ludolph A, Drory V, Hardiman O, Nakano I, Ravits J, Robberecht W, Shefner J. A revision of the El Escorial criteria-2015. Amyotroph Lateral Scler Frontotemporal Degener. 2015;16(5-6):291-2.

6. Menke RA, Agosta F, Grosskreutz J, Filippi M, Turner MR. Neuroimaging endpoints in amyotrophic lateral sclerosis. Neurotherapeutics. 2017;14(1):11-23.

7. Zhou J, Lal B, Wilson DA, Laterra J, van Zijl P. Amide proton transfer (APT) contrast for imaging of brain tumors. Magnetic Resonance in Medicine. 2003;50(6):1120-6.

8. Zhou J, Tryggestad E, Wen Z, Lal B, Zhou T, Grossman R, Wang S, Yan K, Fu D-X, Ford E. Differentiation between glioma and radiation necrosis using molecular magnetic resonance imaging of endogenous proteins and peptides. Nature medicine. 2011;17(1):130-4.

9. Zhou J, Payen J-F, Wilson DA, Traystman RJ, van Zijl PC. Using the amide proton signals of intracellular proteins and peptides to detect pH effects in MRI. Nature medicine. 2003;9(8):1085-90.

10. Jones KM, Pollard AC, Pagel MD. Clinical applications of chemical exchange saturation transfer (CEST) MRI. Journal of Magnetic Resonance Imaging. 2018;47(1):11-27.

11. Lokesh N, Seegerer A, Hioe J, Gschwind RM. Chemical Exchange Saturation Transfer in Chemical Reactions: A Mechanistic Tool for NMR Detection and Characterization of Transient Intermediates. Journal of the American Chemical Society. 2018;140(5):1855-62.

12. Liu G, Liang Y, Bar-Shir A, Chan KWY, Galpoththawela CS, Bernard SM, Tse T, Yadav NN, Walczak P, McMahon MT. Monitoring enzyme activity using a diamagnetic chemical exchange saturation transfer MRI contrast agent. Journal of the American Chemical Society. 2011.

13. van Zijl PCM, Yadav NN. Chemical exchange saturation transfer (CEST): What is in a name and what isn't? Magnetic Resonance in Medicine. 2011;65(4):927-48. doi: 10.1002/mrm.22761.

14. Sun PZ, Xiao G, Zhou IY, Guo Y, Wu R. A method for accurate pH mapping with chemical exchange saturation transfer (CEST) MRI. Contrast Media Mol Imaging. 2016;11(3):195-202. doi: 10.1002/cmmi.1680. PubMed PMID: 26689424.

15. Wu R, Xiao G, Zhou IY, Ran C, Sun PZ. Quantitative chemical exchange saturation transfer (qCEST) MRI - omega plot analysis of RF-spillover-corrected inverse CEST ratio asymmetry for simultaneous determination of labile proton ratio and exchange rate. NMR Biomed. 2015;28(3):376-83. doi: 10.1002/nbm.3257. PubMed PMID: 25615718; PubMed Central PMCID: PMC4339459.

16. Dai Z, Ji J, Xiao G, Yan G, Li S, Zhang G, Lin Y, Shen Z, Wu R. Magnetization Transfer Prepared Gradient Echo MRI for CEST Imaging. PloS one. 2014;9(11):e112219.

17. Sun PZ, Xiao G, Zhou IY, Guo Y, Wu R. A method for accurate pH mapping with chemical exchange saturation transfer (CEST) MRI. Contrast media & molecular imaging. 2016;11(3):195-202.

18. Pyra T, Hui B, Hanstock C, Concha L, Wong JC, Beaulieu C, Johnston W, Kalra S. Combined structural and neurochemical evaluation of the corticospinal tract in amyotrophic lateral sclerosis. Amyotrophic Lateral Sclerosis. 2010;11(1-2):157-65.

19. Wong JC, Concha L, Beaulieu C, Johnston W, Allen PS, Kalra S. Spatial profiling of the corticospinal tract in amyotrophic lateral sclerosis using diffusion tensor imaging. Journal of Neuroimaging. 2007;17(3):234-40.

20. Wu R, Bruening R. Comparison of Diffusion-Weighted MR Imaging and T2-Weighted MR Imaging in Patients with Amyotrophic Lateral Sclerosis. The neuroradiology journal. 2006;19(6):705-10.

21. Togao O, Yoshiura T, Keupp J, Hiwatashi A, Yamashita K, Kikuchi K, Suzuki Y, Suzuki SO, Iwaki T, Hata N. Amide proton transfer imaging of adult diffuse gliomas: correlation with histopathological grades. Neuro-oncology. 2013;16(3):441-8.

22. Park JE, Kim HS, Park KJ, Kim SJ, Kim JH, Smith SA. Pre-and posttreatment glioma: comparison of amide proton

transfer imaging with MR spectroscopy for biomarkers of tumor proliferation. Radiology. 2015;278(2):514-23.

23. Guégan C, Przedborski S. Programmed cell death in amyotrophic lateral sclerosis. The Journal of clinical investigation. 2003;111(2):153-61.

24. Szelechowski M, Amoedo N, Obre E, Léger C, Allard L, Bonneu M, Claverol S, Lacombe D, Oliet S, Chevallier S. Metabolic Reprogramming in Amyotrophic Lateral Sclerosis. Scientific reports. 2018;8(1):3953.

25. Chitnis T, Weiner HL. CNS inflammation and neurodegeneration. The Journal of clinical investigation. 2017;127(10):3577-87.

26. Ito Y, Ofengeim D, Najafov A, Das S, Saberi S, Li Y, Hitomi J, Zhu H, Chen H, Mayo L. RIPK1 mediates axonal degeneration by promoting inflammation and necroptosis in ALS. Science. 2016;353(6299):603-8.

27. Lindberg MJ, Byström R, Boknäs N, Andersen PM, Oliveberg M. Systematically perturbed folding patterns of amyotrophic lateral sclerosis (ALS)-associated SOD1 mutants. Proceedings of the National Academy of Sciences of the United States of America. 2005;102(28):9754-9.

28. Danielsson J, Inomata K, Murayama S, Tochio H, Lang L, Shirakawa M, Oliveberg M. Pruning the ALS-associated protein SOD1 for in-cell NMR. Journal of the American Chemical Society. 2013;135(28):10266-9.

29. Zaiss M, Kunz P, Goerke S, Radbruch A, Bachert P. MR imaging of protein foldingin vitroemploying Nuclear-Overhauser-mediated saturation transfer. NMR in Biomedicine. 2013;26(12):1815-22. doi: 10.1002/nbm.3021.

30. Hughes J. Pathology of amyotrophic lateral sclerosis. Advances in neurology. 1982;36:61-74.

31. Zhang F, Chen G, He M, Dai J, Shang H, Gong Q, Jia Z. Altered white matter microarchitecture in amyotrophic lateral sclerosis: A voxel-based meta-analysis of diffusion tensor imaging. NeuroImage: Clinical. 2018;19:122-9.

32. Senda J, Ito M, Watanabe H, Atsuta N, Kawai Y, Katsuno M, Tanaka F, Naganawa S, Fukatsu H, Sobue G. Correlation between pyramidal tract degeneration and widespread white matter involvement in amyotrophic lateral sclerosis: a study with tractography and diffusion-tensor imaging. Amyotrophic Lateral Sclerosis. 2009;10(5-6):288-94.

33. Roccatagliata L, Bonzano L, Mancardi G, Canepa C, Caponnetto C. Detection of motor cortex thinning and corticospinal tract involvement by quantitative MRI in amyotrophic lateral sclerosis. Amyotrophic Lateral Sclerosis. 2009;10(1):47-52.

34. Wang S, Poptani H, Woo JH, Desiderio LM, Elman LB, McCluskey LF, Krejza J, Melhem ER. Amyotrophic lateral sclerosis: diffusion-tensor and chemical shift MR imaging at 3.0 T. Radiology. 2006;239(3):831-8.

35. Hecht M, Fellner F, Fellner C, Hilz M, Heuss D, Neundörfer B. MRI-FLAIR images of the head show corticospinal tract alterations in ALS patients more frequently than T2-, T1-and proton-density-weighted images. Journal of the neurological sciences. 2001;186(1):37-44.

36. Ji Y, Zhou IY, Qiu B, Sun PZ. Progress toward quantitative in vivo chemical exchange saturation transfer (CEST) MRI. Israel Journal of Chemistry. 2017.

37. Wu B, Warnock G, Zaiss M, Lin C, Chen M, Zhou Z, Mu L, Nanz D, Tuura R, Delso G. An overview of CEST MRI for non-MR physicists. EJNMMI physics. 2016;3(1):19.

38. Tang X, Dai Z, Xiao G, Yan G, Shen Z, Zhang T, Zhang G, Zhuang Z, Shen Y, Zhang Z, Hu W, Wu R. Nuclear Overhauser Enhancement-Mediated Magnetization Transfer Imaging in Glioma with Different Progression at 7 T. ACS chemical neuroscience. 2017;8(1):60-6.

39. Cai K, Singh A, Poptani H, Li W, Yang S, Lu Y, Hariharan H, Zhou XJ, Reddy R. CEST signal at 2 ppm (CEST@ 2ppm) from Z-spectral fitting correlates with creatine distribution in brain tumor. NMR in biomedicine. 2015;28(1):1-8.

40. Guo YL, Li SJ, Zhang ZP, Shen ZW, Zhang GS, Yan G, Wang YT, Rao HB, Zheng WB, Wu RH. Parameters of diffusional kurtosis imaging for the diagnosis of acute cerebral infarction in different brain regions. Experimental and therapeutic medicine. 2016;12(2):933-8. Epub 2016/07/23. doi: 10.3892/etm.2016.3390. PubMed PMID: 27446298; PubMed Central PMCID: PMCPmc4950828.

41. Guo YL, Zhang ZP, Zhang GS, Kong LM, Rao HB, Chen W, Wang GW, Shen ZW, Zheng WB, Wu RH. Evaluation of mean diffusion and kurtosis MRI mismatch in subacute ischemic stroke: Comparison with NIHSS score. Brain Res. 2016;1644:231-9. Epub 2016/05/22. doi: 10.1016/j.brainres.2016.05.020. PubMed PMID: 27208488.

42. Cedarbaum JM, Stambler N, Malta E, Fuller C, Hilt D, Thurmond B, Nakanishi A, Group BAS, Group AclotBS. The ALSFRS-R: a revised ALS functional rating scale that incorporates assessments of respiratory function. Journal of the neurological sciences. 1999;169(1-2):13-21.

43. Kim M, Gillen J, Landman BA, Zhou J, van Zijl PCM. Water saturation shift referencing (WASSR) for chemical exchange saturation transfer (CEST) experiments. Magnetic Resonance in Medicine. 2009;61(6):1441-50.

Chapter 5

pH Measurement using CEST, Validation and Application

This chapter is based on two published ISMRM abstracts.

” Zhuozhi Dai , Phillip Zhe Sun , Gang Xiao , Gen Yan , Yanlong Jia , Zhiwei Shen , Alan H. Wilman , and Renhua Wu. Quantitative pH using chemical exchange saturation transfer and phosphorous spectroscopy. ISMRM 2016.”

” Zhuozhi Dai, Yanlong Jia, Gen Yan, Fei Duan, Gang Xiao, Zhiwei Shen, Hongfu Sun, Alan H. Wilman, and Renhua Wu, pH-weighted imaging in diabetes mellitus suffering acute cerebral ischemic stroke, ISMRM 2015.”

Abstract

In this chapter, CEST imaging is applied to pH measurement at 7.0 T in rat brain. CEST was compared to phosphorous spectroscopy for computing pH and a strong correlation between pH from the two methods was found (Pearson’s correlation 0.82 $P < 0.01$). pH imaging was then applied to distinguish diabetic from non-diabetic stroke in an animal model. A significant pH decreases in the ischemic lesion in diabetes compared with non-diabetic stroke was found ($P < 0.01$). However, no distinction in contralateral normal regions both of diabetic and non-diabetic models ($P = 0.14$). In addition, the signal intensities were significantly decreased in ischemic lesions compared to the contralateral normal regions both within diabetic stroke models ($P < 0.01$) and non-diabetic stroke models ($P < 0.01$). In conclusion, our study established a strong correlation of pH between CEST and 31P-MRS in vivo. Moreover, we applied pH-weighted imaging using CEST to examine diabetic stroke. We obtained a significant pH decrease in the

ischemic lesion in diabetes compared with non-diabetes in vivo, which may provide a marker of specificity of diabetic stroke.

5.1 Introduction

pH is a very important biochemical property that changes in many pathological states, such as tumor, stroke etc(3, 57, 155, 156). Monitoring pH is of significance in early diagnosis and treatment therapy(157, 158). However, there is lack of non-invasive methods to image pH in vivo effectively. This short chapter examines the use of CEST imaging to quantify the pH value. First, a CEST method of measuring pH is validated against phosphorous spectroscopy (31P-MRS) in rat brain. Next, pH-weighted imaging is applied to distinguish the type of stroke. The presence of diabetes increases the risk and severity of stroke(159). Diabetic stroke has poorer functional outcomes and higher mortality rates than non-diabetic stroke(160), but conventional MRI examinations cannot distinguish between diabetic and non-diabetic stroke. The purpose of our study was to determine the specificity to diabetic stroke of amide proton transfer (3, 40), a novel pH-weighted imaging method.

5.2 Materials and Methods

5.2.1 pH Validation of CEST versus Phosphorous Spectroscopy

MRI: Data were collected at 7.0 T on an animal MRI system using a standard ^{1}H body coil (63 mm internal diameter) and 31P surface coil for RF pulse transmitting and receiving. Image sequences included Z-spectrum, T1 map, T2 map and 31P-MRS. For CEST, we used a continuous wave as the pre-saturation component, saturation time=3 s, saturation power=0.75 μT, 1 μT and 2 μT respectively, amino proton frequency offset=3.5ppm, reference offset=-3.5 ppm. For Z-spectrum, we serially altered the frequency offset from -5.6 ppm to 5.6 ppm, in steps of 0.2 ppm. We used a Point Resolved Spectroscopy (PRESS) sequence as a readout component to

obtain the Z-spectrum. Seven water spectrum were acquired for T1 measurement using a PRESS sequence with different TR, ranging from 1.1 s to 6 s. Six water spectrum were obtained for T2 measurement with TEs from 6.5 to 70 ms. After 1H-imaging, the body coil was detuned and 31P-MRS were tuned to obtain the spectrum in the same voxel.

Animal models: Brains of five normal adult male Sprague-Dawley (SD) rats were scanned in vivo. The animals were euthanized with overdose of Phenobarbital by intravenous injection after the first scanning to create whole brain stroke models, which were scanned immediately in the first 3 hours after stroke.

Analysis: All data were post-processed in Matlab and SPSS. Quantitative pH was calculated by fitting Z spectrum and by 31P-MRS. Both the standard two pools quantifying exchange rates in chemical exchange saturation transfer agents using saturation power dependencies (QUESP)(161) and a homemade Nuclear Overhauser Effect including constrained nonlinear multivariable (NICN) fitting methods were using to calculate the quantitative pH value. The NOE pool was taken into account in the next method. 31P-MRS used the chemical shift difference between pH-dependent inorganic phosphate and phosphocreatine to calculate the pH value. Assessment of the correlation between CEST pH and 31P-MRS pH was performed via Pearson correlation analysis. Means and standard variance in each method were calculated and analysed with one-way ANOVA to compare the mean differences, $p < 0.01$ was considered as statistically significant.

5.2.2 pH-weighted imaging in Diabetes Mellitus suffering Acute Cerebral Ischemic Stroke

Animal models: Diabetes models were produced in four adult male Sprague-Dawley (SD) rats by intraperitoneal injection of streptozotocin. Animals were fed with a normal diet for three months, while blood sugar was monitored every five days to ensure levels of ~ 30 mM. After 3 months, permanent middle cerebral artery occlusion (MCAO) was produced using thread embolism on the diabetic group and on an age and sex matched healthy control group.

MRI: Data were collected in the first 3 hours after occlusion at 7.0 T on an animal MRI system using a standard body coil for RF pulse transmitting and receiving. Image sequences included pH-weighted imaging, Z-spectrum, diffusion-weighted imaging, T1-weighted imaging and T2-weighted imaging. We used a continuous wave as the presaturated component, saturation time 5 s, saturation power 0.75 μT, amino proton frequency offset 3.5ppm, reference offset -3.5 ppm. For Z-spectrum, we serially altered the frequency offset from -4.7 ppm to 4.7 ppm, in steps of 0.2 ppm. We used single-shot echo planar imaging (EPI) as a readout component to obtain images and Point Resolved Spectroscopy sequence to obtain the Z-spectrum. Others parameters for EPI were set as follows: TR 6000 ms, TE 6ms, number of average 32, bandwidth 50 kHz, imaging matrix 64 × 64.

Analysis: All the data were post-processed using in-house programs in Matlab. MTR asymmetric analysis methods were used to calculate pH-weighted images(11). Regions of interest (ROIs) were drawn on the ischemic lesions and contralateral normal regions both in diabetes and non-diabetes. Assessment of the contrast between the diabetes and non-diabetes was performed

via one-way ANOVA. Values were presented as mean ± SD, and $p < 0.01$ was considered as statistically significant.

5.3 Results and discussion

5.3.1 CEST versus Phosphorous spectroscopy

The quantitative pH values from CEST effect and from 31P-MRS are shown in Figure 5.1. Statistical results indicated strong correlation, Pearson correlation factor is 0.82, $P < 0.01$ (Fig. 5.2). Moreover, ANOVA results show $F = 23.2$, which was significant ($P < 0.01$), the effect size is 81.2%. The pH difference between normal brain tissues and stroke brain lesions was significant ($P < 0.01$). Comparing the two CEST fitting methods, the standard two pools QUESP method could not fit the in vivo data well because of the existing NOE effect, while our NICN method had a superior fitting both at CEST effect and NOE sides of the spectrum. Therefore, we used the NICN method to quantify the pH value and compared it with 31P-MRS. The difference between CEST and 31P-MRS methods was insignificant ($P = 0.95$ for stroke and $P = 0.90$ for normal tissues) (Fig. 5.1).

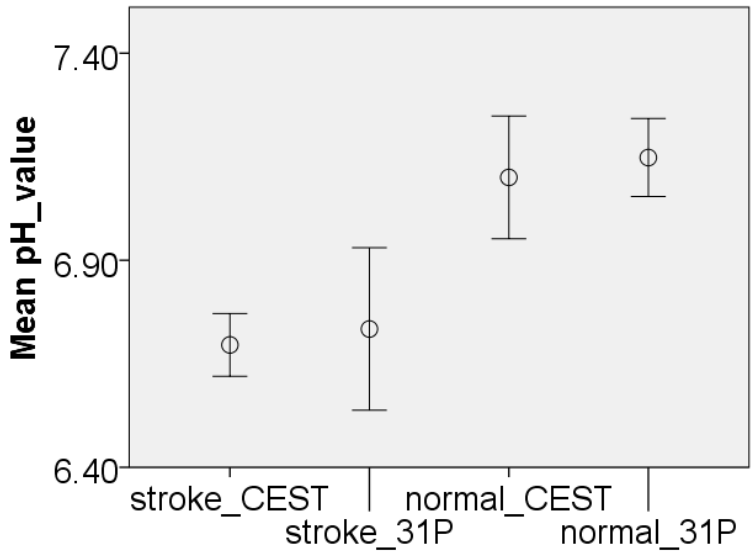

Figure 5.1 The pH difference between normal brain tissues and stroke brain lesions was significant ($P < 0.01$). The difference between CEST and 31P-MRS methods was insignificant ($P = 0.95$ for stroke and $P = 0.90$ for normal tissues).

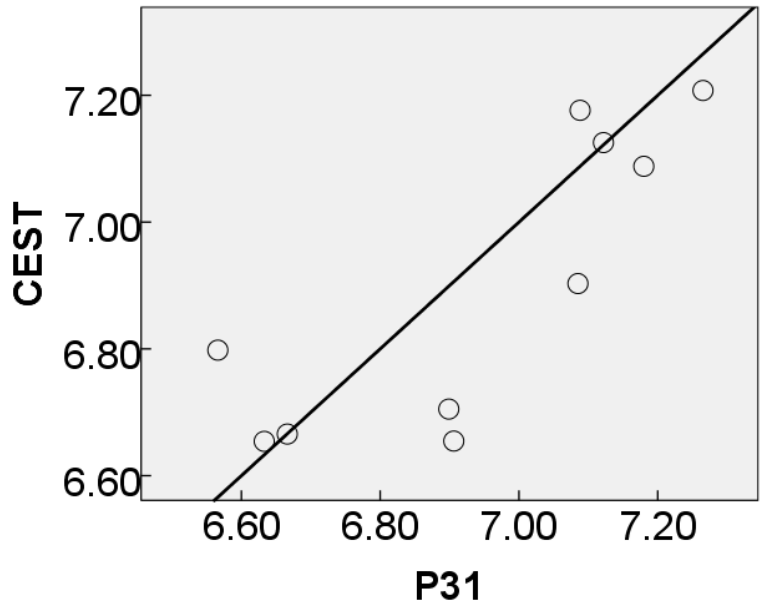

Figure 5.2 Correlation between CEST and from 31P-MRS, Pearson correlation factor is 0.82, $P < 0.01$.

5.3.2 pH-weighted imaging in diabetes mellitus suffering acute cerebral ischemic stroke

As expected, there was no visible difference between the diabetic (DM) and non-diabetic (N-DM) MCAO models in routine MRI. In pH-weighted imaging (Figs. 5.3, 5.4), the signal in the ischemic lesion in DM was significantly lower than that in N-DM ($p < 0.01$), which indicated a more substantial decrease in pH in DM after occlusion. However, the signals in the contralateral normal regions in DM and N-DM were essentially identical, meaning the pH values were not correlative with the level of blood sugar under normal supply of blood and oxygen. In the Z spectrum (Fig. 5.5), there is clear distinction at about 3.5 ppm between the DM lesion, N-DM lesion and normal region, which further verifies our pH-weighted imaging results, because the amide proton concentration was constant in the first three hours after occlusion.

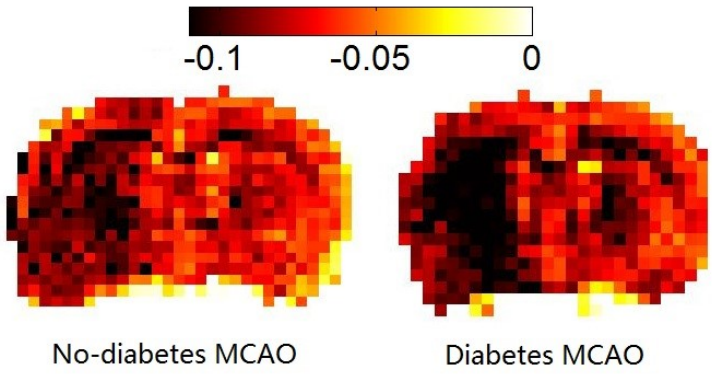

Figure 5. 3 pH-weighted imaging in diabetic and non-diabetic MCAO. The signal intensity in diabetic ischemic lesion was significantly decreased.

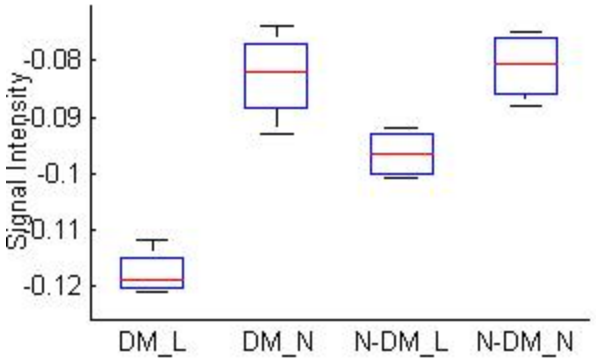

Figure 5. 4 MTR asymmetry signal intensity of different regions using ROI analysis. There was a significant distinction in the ischemic lesions between diabetic (DM_L) and non-diabetic MCAO (N-DM_L) ($P < 0.01$), but no distinction in contralateral normal regions both of diabetic (DM_N) and non-diabetic models(N-DM_N) ($P = 0.14$). The signal intensities were significantly decreased in ischemic lesions compared to the contralateral normal regions both within diabetic stroke models ($P < 0.01$) and non-diabetic stroke models ($P < 0.01$).

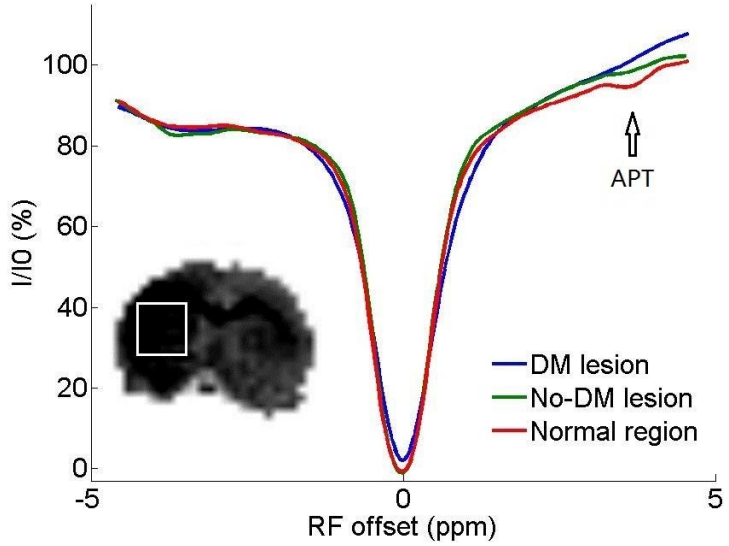

Figure 5. 5 Z-spectrum of diabetic ischemic lesion, Non-diabetic ischemic lesion and contralateral normal region. there was clear distinction at about 3.5 ppm.

5.4 Conclusion

Our study established a strong correlation of pH between CEST and 31P-MRS in vivo. Because CEST imaging has superior spatial resolution to 31P-MRS, CEST may provide an alternative, straightforward, and effective way to obtain quantitative pH images in vivo. We applied ph-weighted imaging using CEST to examine diabetic stroke. To our knowledge this is the first report on pH-weighted imaging in diabetic stroke models. We obtained a significant pH decrease in the ischemic lesion in diabetes compared with non-diabetes in vivo, which may provide a marker of specificity of diabetic stroke. Overall, this short chapter has demonstrated the value of pH imaging using CEST.

References

1. Chen LQ, Pagel MD. Evaluating pH in the Extracellular Tumor Microenvironment Using CEST MRI and Other Imaging Methods. Advances in Radiology. 2015;2015.

2. Sun PZ, Xiao G, Zhou IY, Guo YK, Wu RH. A method for accurate pH mapping with chemical exchange saturation transfer (CEST) MRI. Contrast Media & Molecular Imaging. 2016;11(3):195-202. doi: 10.1002/cmmi.1680. PubMed PMID: WOS:000378426700003.

3. Zhou J, Payen J-F, Wilson DA, Traystman RJ, van Zijl PC. Using the amide proton signals of intracellular proteins and peptides to detect pH effects in MRI. Nature medicine. 2003;9(8):1085-90.

4. McVicar N, Li AX, Goncalves DF, Bellyou M, Meakin SO, Prado MA, Bartha R. Quantitative tissue pH measurement during cerebral ischemia using amine and amide concentration-independent detection (AACID) with MRI. Journal of Cerebral Blood Flow & Metabolism. 2014;34(4):690-8.

5. Gillies RJ, Raghunand N, Garcia-Martin ML, Gatenby RA. pH imaging. Engineering in Medicine and Biology Magazine, IEEE. 2004;23(5):57-64.

6. Dai Z, Jia Y, Yan G, Duan F, Xiao G, Shen Z, Sun H, Wilman AH, Wu R. pH-weighted imaging in diabetes mellitus suffering acute cerebral ischemic stroke. International Society of Magnetic Resonance in Medicine 23rd Annual Meeting. 2015.

7. Shambesh MKA, Emahbes TM, Kama F, Saleh Z, Shambesh IM. Diabetes Mellitus and Cerebrovascular Accident among North African Population (Libya) Community Based Survey. International Journal of TROPICAL DISEASE & Health. 2015;10(2):1-9.

8. Tziomalos K, Spanou M, Bouziana SD, Papadopoulou M, Giampatzis V, Kostaki S, Dourliou V, Tsopozidi M, Savopoulos C, Hatzitolios AI. Type 2 diabetes is associated with a worse functional outcome of ischemic stroke. World journal of diabetes. 2014;5(6):939.

9. Zhou J, Tryggestad E, Wen Z, Lal B, Zhou T, Grossman R, Wang S, Yan K, Fu D-X, Ford E. Differentiation between glioma and radiation necrosis using molecular magnetic resonance imaging of endogenous proteins and peptides. Nature medicine. 2011;17(1):130-4.

10. McMahon MT, Gilad AA, Zhou J, Sun PZ, Bulte JWM, van Zijl PCM. Quantifying exchange rates in chemical

exchange saturation transfer agents using the saturation time and saturation power dependencies of the magnetization transfer effect on the magnetic resonance imaging signal (QUEST and QUESP): Ph calibration for poly-L-lysine and a starburst dendrimer. Magnetic Resonance in Medicine. 2006;55(4):836-47. doi: 10.1002/mrm.20818.

11. Zhou J, Zijl PCMv. Chemical exchange saturation transfer imaging and spectroscopy. Progress in Nuclear Magnetic Resonance Spectroscopy. 2006;48(2-3):109-36. doi: 10.1016/j.pnmrs.2006.01.001.

Chapter 6

Conclusions

6.1 Conclusions

In this thesis, we optimized and applied chemical exchange saturation transfer imaging technique at 3T, 4.7T, and 7T. It is a multidisciplinary program. In these studies, we have proposed a CEST sequence with good clinical hardware compatibility, expanded the application of CEST in animal models such as pH-weighted imaging in stroke, glutamate imaging in schizophrenia etc., and then performed the clinical translation in the patients with amyotrophic lateral sclerosis using amide proton transfer imaging. These findings help improve the CEST technique, prompt its application, and more importantly better understanding of the diseases.

In Chapter 1, the brief introduction of CEST was presented, including the theory, sequence, post procession, and relevant applications. CEST is a novel MRI technology that is able to detect and quantify specific components that are not imaged in routine MRI methods, enabling the detection of metabolic changes, potentially in the early stages of the disease. However, the CEST sequence is not a standard sequence in clinical MRI, the implementation of CEST needs a special sequence and the corresponding post-processing program, which required further optimization and improvement. In previous heuristic researches, CEST MRI has been shown capable of detecting a host of biomolecules including amide, glutamate, glucose as well as pH and temperature, etc. It will have broad prospects with its application in different diseases to be explored.

Sequence developments were presented in chapter 1 and chapter 2. In which we compared the conventional CEST sequences and proposed a new sequence called magnetization transfer (MT) prepared gradient echo (GRE) MRI for CEST imaging. Since the routine CEST MRI have a long RF saturation pulse, it usually has high specific absorption rate and limited spatial resolution. In addition, echo planar imaging (EPI)-based fast image readout is prone to image distortion, particularly severe at high field. To address these limitations, we evaluated magnetization transfer (MT) prepared gradient echo (GRE) MRI for CEST imaging. We proved the feasibility using numerical simulations and experiments in vitro and in vivo. Then we optimized the sequence by serially evaluating the effects of the number of saturation steps, MT saturation power (B1), GRE readout flip angle (FA), and repetition time (TR) upon the CEST MRI, and further demonstrated the endogenous amide proton CEST imaging in rat brains that underwent permanent middle cerebral artery occlusion.

The applications of CEST in animal models were presented in in chapter 3 and chapter 5. In chapter 3, we applied a glutamate imaging technique in schizophrenic models and demonstrated that glutamate changes in different regions of the brain at an early stage, which may provide a powerful indicator of the diagnosis of schizophrenia prodrome. The diagnosis of schizophrenia prodrome is of significance since early intervention may prevent the development of full-blown schizophrenia. Increasing evidence indicates that glutamate is involved in the incidence of schizophrenia. Our previous studies demonstrated that the cuprizone-induced C57BL/6 mouse showed behavioral changes and has been employed to examine the brain metabolite alterations in

various stages of schizophrenia. In this program, we further examine glutamate variation in different brain regions in an early schizophrenia model using glutamate imaging technique. Our results proved that the signal intensity of glutamate image was strictly related to glutamate concentration, and the other neuro metabolites contribute negligible glutamate CEST effects. Compared to healthy controls, glutamate signals of schizophrenic models increased in the whole brain, especially in the cerebral cortex, hippocampus, and thalamus. In addition, the glutamate CEST image has excellent correlation with spectroscopy.

We also established a strong correlation of pH between CEST and 31P-MRS in vivo in chapter 5. Because CEST imaging has superior spatial resolution to 31P-MRS, CEST may provide an alternative, straightforward, and effective way to obtain quantitative pH images in vivo. Further exploration found a significant pH decrease in the ischemic lesion in diabetes compared with non-diabetes in vivo, which may provide a marker of specificity of diabetic stroke.

For clinical translation, we applied the amide proton transfer (APT) imaging in patients with amyotrophic lateral sclerosis (ALS) at 3 T. Amyotrophic lateral sclerosis (ALS) is a progressive, fatal disease characterized by the death of neurons controlling voluntary muscle movement. There is lack of objective imaging indicators for ALS diagnosis and assessment. This part aims to explore the value of APT in ALS patients and the correlation between APT and diffusion tensor imaging (DTI). Our results demonstrated the changes of APT in the motor cortex and corticospinal tract of ALS patients, which has the potential to be an objective imaging biomarker

for ALS diagnosis. The combination of APT and DTI can simultaneously detect changes of metabolism and microstructure in ALS patients.

6.2 Limitations

A major limitation of these studies is the diversity of diseases studied. Although it is beneficial to the exploration of CEST application, this inconsistency limits the in-depth study of a specific disease. Part of this limitation is because these experiments were performed in different laboratories and have unique characteristics. A coherent study in the future of one disease beginning from the molecular mechanisms, to cellular levels, animal models and to patients could help reveal more detailed disease specific findings.

In this thesis, we covered several branches of CEST technology, including APT, pH-weighted imaging, and glutamate imaging. The sequences were different between these experiments. For example, continuous wave pre-saturation was used in animal studies, but it was not suitable for human studies. Also, the post-processing methods kept improving throughout the thesis. Lorentz fitting was not introduced in the early experiments. These factors complicated the comparison of the results.

Another limitation is that the signal intensity may be affected by other neuro metabolite effects. Our previous study has proved the CEST effect of GABA in brain tumor, and other researchers also report that about 25–30% signal intensity of glutamate image comes from Cr, GABA, and

other macromolecules. Therefore, further optimization is required in future studies. The APT imaging also has similar saturation frequency with glutamate, 3.5 ppm vs. 3 ppm, respectively. However, APT has a lower exchange rate, so the saturation power is usually much lower (~1.3 μT) and the signal intensity is more susceptible to contamination of nuclear Overhauser effect. Therefore, Lorentz fitting is more suitable to APT imaging.

Specific to APT studies, there are some limitations in our study and some expectations for future research. First, we only explored the APT performance in a single disease. Further comparison of different diseases with similar symptoms to ALS such as primary lateral sclerosis, progressive bulbar palsy, etc. is useful and necessary. Whether APT is able to provide early detection is also critical in the diagnosis of ALS, future study should take this into account. In addition, the sample size is relatively small, and some significances may have been overestimated.

6.3 Future Directions

To summarize, CEST is a promising technique with broad application prospects. There are several future directions of CEST, including unification, interdisciplinary integration, and multi-modality experiments. Since CEST sequences vary from lab to lab and the barriers between different commercial scanners, it is difficult to have a uniform technique presently. This factor weakens the comparisons between different experiments and limits its range of applications. Future improvement will be the unification of sequences and post-processing, and to propose an optimal protocol across different field strengths. Better interdisciplinary integration is another area for improvement. Not merely a combination of multiple technologies, effective

integration and teamwork will help improve the quality of CEST technique, and more importantly, its application in clinical studies.

Multimodality image is a trend for medical imaging diagnosis, which takes advantage of the strength of different imaging modalities to provide a more comprehensive picture of the disease. CEST may be a critical and competitive part that has a particular niche in the detection of metabolism. As no contrast agents were used in CEST, it may reflect true pathological changes, which will be more easily depicted at higher strength magnetic fields such as 7 Tesla. The combination of CEST and DTI will provide a phenomenal tool to detect neurochemical and microstructure simultaneously. By leveraging full features of advanced imaging techniques, one can increase the diagnostic accuracy and sensitivity.

References:

1. K. M. Ward AHA, and R. S. Balaban. A New Class of Contrast Agents for MRI Based on Proton Chemical Exchange Dependent Saturation Transfer (CEST). Journal of Magnetic Resonance. 2000;143(1):79-87. doi: 10.1006/jmre.1999.1956.
2. Zhou J, Lal B, Wilson DA, Laterra J, van Zijl P. Amide proton transfer (APT) contrast for imaging of brain tumors. Magnetic Resonance in Medicine. 2003;50(6):1120-6.
3. Zhou J, Payen J-F, Wilson DA, Traystman RJ, van Zijl PC. Using the amide proton signals of intracellular proteins and peptides to detect pH effects in MRI. Nature medicine. 2003;9(8):1085-90.
4. Cai K, Haris M, Singh A, Kogan F, Greenberg JH, Hariharan H, Detre JA, Reddy R. Magnetic resonance imaging of glutamate. Nature Medicine. 2012;18(2):302-6. doi: 10.1038/nm.2615.
5. Nasrallah FA, Pagès G, Kuchel PW, Golay X, Chuang K-H. Imaging brain deoxyglucose uptake and metabolism by glucoCEST MRI. Journal of Cerebral Blood Flow & Metabolism. 2013;33(8):1270-8. doi: 10.1038/jcbfm.2013.79.
6. Haris M, Cai K, Singh A, Hariharan H, Reddy R. In vivo mapping of brain myo-inositol. NeuroImage. 2011;54(3):2079-85. doi: 10.1016/j.neuroimage.2010.10.017.
7. Dai Z, Zhang T, Jia Y, Yan G, Xiao G, Zhang G, Shen Z, Wu R. Glutamate and GABA Imaging at 7 Tesla. International Society of Magnetic Resonance in Medicine 22nd annual meeting. 2014.
8. Hancu I, Dixon WT, Woods M, Vinogradov E, Sherry AD, Lenkinski RE. CEST and PARACEST MR contrast agents. Acta Radiologica. 2010;51(8):910-23. doi: 10.3109/02841851.2010.502126.
9. Suchý M, Li AX, Liu Y, Feng Q, Bartha R, Hudson RH. Preliminary evaluation of PARACEST MRI agents for the detection of nitric oxide synthase. Canadian Journal of Chemistry. 2016;94(8):715-22.
10. Zhou J, Wilson DA, Sun PZ, Klaus JA, van Zijl PCM. Quantitative description of proton exchange processes between water and endogenous and exogenous agents for WEX, CEST, and APT experiments. Magnetic Resonance in Medicine. 2004;51(5):945-52. doi: 10.1002/mrm.20048.
11. Zhou J, Zijl PCMv. Chemical exchange saturation transfer imaging and spectroscopy. Progress in Nuclear Magnetic Resonance Spectroscopy. 2006;48(2-3):109-36. doi: 10.1016/j.pnmrs.2006.01.001.
12. Schröder L, Lowery TJ, Hilty C, Wemmer DE, Pines A. Molecular imaging using a targeted magnetic resonance hyperpolarized biosensor. Science. 2006;314(5798):446-9.
13. Togao O, Kessinger CW, Huang G, Soesbe TC, Sagiyama K, Dimitrov I, Sherry AD, Gao J, Takahashi M. Characterization of Lung Cancer by Amide Proton Transfer (APT) Imaging: An In-Vivo Study in an Orthotopic Mouse Model. PloS one. 2013;8(10):e77019.
14. Kunth M, Witte C, Schröder L. Continuous-wave saturation considerations for efficient xenon depolarization. NMR in Biomedicine. 2015;28(6):601-6.
15. Sun PZ, Benner T, Kumar A, Sorensen AG. Investigation of optimizing and translating pH-sensitive pulsed-chemical exchange saturation transfer (CEST) imaging to a 3T clinical scanner. Magnetic Resonance in Medicine. 2008;60(4):834-41. doi: 10.1002/mrm.21714.
16. Zu Z, Li K, Janve VA, Does MD, Gochberg DF. Optimizing pulsed-chemical exchange saturation transfer imaging sequences. Magn Reson Med. 2011;66(4):1100-8. doi: 10.1002/mrm.22884. PubMed PMID: 21432903; PubMed Central PMCID: PMC3151337.
17. Schmitt B, Zaiß M, Zhou J, Bachert P. Optimization of pulse train presaturation for CEST imaging in clinical scanners. Magnetic Resonance in Medicine. 2011;65(6):1620-9. doi: 10.1002/mrm.22750.
18. Sun PZ, Lu J, Wu Y, Xiao G, Wu RH. Evaluation of the dependence of CEST-EPI measurement on repetition time, RF irradiation duty cycle and imaging flip angle for enhanced pH sensitivity. Physics in Medicine and Biology. 2013;58(17):N229-N40. doi: 10.1088/0031-9155/58/17/n229. PubMed PMID: WOS:000323517700001.
19. Longo DL, Dastrù W, Digilio G, Keupp J, Langereis S, Lanzardo S, Prestigio S, Steinbach O, Terreno E, Uggeri F, Aime S. Iopamidol as a responsive MRI-chemical exchange saturation transfer contrast agent for pH mapping of kidneys: In vivo studies in mice at 7 T. Magnetic Resonance in Medicine. 2010:n/a-n/a. doi: 10.1002/mrm.22608.
20. Zu Z, Janve VA, Xu J, Does MD, Gore JC, Gochberg DF. A new method for detecting exchanging amide protons using chemical exchange rotation transfer. Magnetic Resonance in Medicine. 2013;69(3):637-47. doi: 10.1002/mrm.24284.
21. Zu Z, Xu J, Li H, Chekmenev EY, Quarles CC, Does MD, Gore JC, Gochberg DF. Imaging amide proton transfer

and nuclear overhauser enhancement using chemical exchange rotation transfer (CERT). Magnetic resonance in medicine. 2014;72(2):471-6.
22. Lin EC, Li H, Zu Z, Louie EA, Lankford CL, Dortch RD, Does MD, Gore JC, Gochberg DF. Chemical exchange rotation transfer (CERT) on human brain at 3 Tesla. Magnetic resonance in medicine. 2018.
23. Scheidegger R, Vinogradov E, Alsop DC. Amide proton transfer imaging with improved robustness to magnetic field inhomogeneity and magnetization transfer asymmetry using saturation with frequency alternating RF irradiation. Magnetic Resonance in Medicine. 2011;66(5):1275-85. doi: 10.1002/mrm.22912.
24. Xu X, Lee J-S, Jerschow A. Ultrafast Scanning of Exchangeable Sites by NMR Spectroscopy. Angewandte Chemie International Edition. 2013;52(32):8281-4. doi: 10.1002/anie.201303255.
25. Xu X, Yadav NN, Song X, McMahon MT, Jerschow A, Van Zijl PC, Xu J. Screening CEST contrast agents using ultrafast CEST imaging. Journal of magnetic resonance. 2016;265:224-9.
26. Jin T, Autio J, Obata T, Kim SG. Spin-locking versus chemical exchange saturation transfer MRI for investigating chemical exchange process between water and labile metabolite protons. Magnetic Resonance in Medicine. 2011;65(5):1448-60.
27. Friedman JI, McMahon MT, Stivers JT, Van Zijl PCM. Indirect detection of labile solute proton spectra via the water signal using frequency-labeled exchange (FLEX) transfer. Journal of the American Chemical Society. 2010;132(6):1813-5.
28. Hua J, Jones CK, Blakeley J, Smith SA, Van Zijl PC, Zhou J. Quantitative description of the asymmetry in magnetization transfer effects around the water resonance in the human brain. Magnetic Resonance in Medicine: An Official Journal of the International Society for Magnetic Resonance in Medicine. 2007;58(4):786-93.
29. Zaiss M, Schmitt B, Bachert P. Quantitative separation of CEST effect from magnetization transfer and spillover effects by Lorentzian-line-fit analysis of z-spectra. Journal of magnetic resonance. 2011;211(2):149-55.
30. Desmond KL, Moosvi F, Stanisz GJ. Mapping of amide, amine, and aliphatic peaks in the CEST spectra of murine xenografts at 7 T. Magnetic resonance in medicine. 2014;71(5):1841-53.
31. Cai K, Singh A, Poptani H, Li W, Yang S, Lu Y, Hariharan H, Zhou XJ, Reddy R. CEST signal at 2 ppm (CEST@ 2ppm) from Z-spectral fitting correlates with creatine distribution in brain tumor. NMR in biomedicine. 2015;28(1):1-8.
32. Dixon WT, Ren J, Lubag AJ, Ratnakar J, Vinogradov E, Hancu I, Lenkinski RE, Sherry AD. A concentration-independent method to measure exchange rates in PARACEST agents. Magnetic Resonance in Medicine. 2010;63(3):625-32.
33. Wu RH, Xiao G, Zhou IY, Ran CZ, Sun PZ. Quantitative chemical exchange saturation transfer (qCEST) MRI - omega plot analysis of RF-spillover-corrected inverse CEST ratio asymmetry for simultaneous determination of labile proton ratio and exchange rate. Nmr in Biomedicine. 2015;28(3):376-83. doi: 10.1002/nbm.3257. PubMed PMID: WOS:000350139800011.
34. Sun PZ, Wang Y, Dai ZZ, Xiao G, Wu RH. Quantitative chemical exchange saturation transfer (qCEST) MRI - RF spillover effect-corrected omega plot for simultaneous determination of labile proton fraction ratio and exchange rate. Contrast Media & Molecular Imaging. 2014;9(4):268-75. doi: 10.1002/cmmi.1569. PubMed PMID: WOS:000333825300002.
35. Randtke EA, Chen LQ, Corrales LR, Pagel MD. The Hanes-Woolf linear QUESP method improves the measurements of fast chemical exchange rates with CEST MRI. Magnetic resonance in medicine. 2014;71(4):1603-12.
36. Kim M, Gillen J, Landman BA, Zhou J, van Zijl PCM. Water saturation shift referencing (WASSR) for chemical exchange saturation transfer (CEST) experiments. Magnetic Resonance in Medicine. 2009;61(6):1441-50. doi: 10.1002/mrm.21873.
37. Sun PZ, Farrar CT, Sorensen AG. Correction for artifacts induced by B0 and B1 field inhomogeneities in pH sensitive chemical exchange saturation transfer (CEST) imaging. Magnetic Resonance in Medicine. 2007;58(6):1207-15.
38. Stancanello J, Terreno E, Castelli DD, Cabella C, Uggeri F, Aime S. Development and validation of a smoothing-splines-based correction method for improving the analysis of CEST-MR images. Contrast Media & Molecular Imaging. 2008;3(4):136-49. doi: 10.1002/cmmi.240.
39. Schuenke P, Windschuh J, Roeloffs V, Ladd ME, Bachert P, Zaiss M. Simultaneous mapping of water shift and B1 (WASABI)—Application to field-Inhomogeneity correction of CEST MRI data. Magnetic resonance in medicine. 2017;77(2):571-80.

40. Zhou J, Tryggestad E, Wen Z, Lal B, Zhou T, Grossman R, Wang S, Yan K, Fu D-X, Ford E. Differentiation between glioma and radiation necrosis using molecular magnetic resonance imaging of endogenous proteins and peptides. Nature medicine. 2011;17(1):130-4.
41. Jones KM, Pollard AC, Pagel MD. Clinical applications of chemical exchange saturation transfer (CEST) MRI. Journal of Magnetic Resonance Imaging. 2018;47(1):11-27.
42. van Zijl PCM, Yadav NN. Chemical exchange saturation transfer (CEST): What is in a name and what isn't? Magnetic Resonance in Medicine. 2011;65(4):927-48. doi: 10.1002/mrm.22761.
43. Sun PZ, Xiao G, Zhou IY, Guo Y, Wu R. A method for accurate pH mapping with chemical exchange saturation transfer (CEST) MRI. Contrast Media Mol Imaging. 2016;11(3):195-202. doi: 10.1002/cmmi.1680. PubMed PMID: 26689424.
44. Wu R, Xiao G, Zhou IY, Ran C, Sun PZ. Quantitative chemical exchange saturation transfer (qCEST) MRI - omega plot analysis of RF-spillover-corrected inverse CEST ratio asymmetry for simultaneous determination of labile proton ratio and exchange rate. NMR Biomed. 2015;28(3):376-83. doi: 10.1002/nbm.3257. PubMed PMID: 25615718; PubMed Central PMCID: PMC4339459.
45. Dai Z, Ji J, Xiao G, Yan G, Li S, Zhang G, Lin Y, Shen Z, Wu R. Magnetization Transfer Prepared Gradient Echo MRI for CEST Imaging. PloS one. 2014;9(11):e112219.
46. Sun PZ, Xiao G, Zhou IY, Guo Y, Wu R. A method for accurate pH mapping with chemical exchange saturation transfer (CEST) MRI. Contrast media & molecular imaging. 2016;11(3):195-202.
47. Wen Z, Hu S, Huang F, Wang X, Guo L, Quan X, Wang S, Zhou J. MR imaging of high-grade brain tumors using endogenous protein and peptide-based contrast. NeuroImage. 2010;51(2):616-22. doi: 10.1016/j.neuroimage.2010.02.050.
48. Tang X, Dai Z, Xiao G, Yan G, Shen Z, Zhang T, Zhang G, Zhuang Z, Shen Y, Zhang Z, Hu W, Wu R. Nuclear Overhauser Enhancement-Mediated Magnetization Transfer Imaging in Glioma with Different Progression at 7 T. ACS chemical neuroscience. 2017;8(1):60-6.
49. Donahue MJ, Donahue PC, Rane S, Thompson CR, Strother MK, Scott AO, Smith SA. Assessment of lymphatic impairment and interstitial protein accumulation in patients with breast cancer treatment‐related lymphedema using CEST MRI. Magnetic resonance in medicine. 2016;75(1):345-55.
50. Wells JA, O'Callaghan JM, Holmes HE, Powell NM, Johnson RA, Siow B, Torrealdea F, Ismail O, Walker-Samuel S, Golay X. In vivo imaging of tau pathology using multi-parametric quantitative MRI. Neuroimage. 2015;111:369-78.
51. Bates RG. Determination of pH: theory and practice. Determination of pH: theory and practice. 1964.
52. Sun PZ, Zhou J, Sun W, Huang J, van Zijl PCM. Detection of the ischemic penumbra using pH-weighted MRI. Journal of Cerebral Blood Flow & Metabolism. 2006;27(6):1129-36. doi: 10.1038/sj.jcbfm.9600424.
53. Sun PZ, Benner T, Copen WA, Sorensen AG. Early Experience of Translating pH-Weighted MRI to Image Human Subjects at 3 Tesla. Stroke. 2010;41(10, Supple 1):S147-S51. doi: 10.1161/strokeaha.110.595777.
54. Sun PZ, Wang E, Cheung JS. Imaging acute ischemic tissue acidosis with pH-sensitive endogenous amide proton transfer (APT) MRI—Correction of tissue relaxation and concomitant RF irradiation effects toward mapping quantitative cerebral tissue pH. NeuroImage. 2012;60(1):1-6. doi: 10.1016/j.neuroimage.2011.11.091.
55. Wu RH LC, Liu PK, Sun PZ. Improved measurement of labile proton concentration-weighted chemical exchange rate (kws) with experimental factor-compensated and T1-normalized quantitative chemical exchange saturation transfer (CEST) MRI. Contrast Media & Molecular Imaging. 2012;in press.
56. Phillip Zhe Sun YW, Gang Xiao, Renhua Wu. Simultaneous determination of labile proton fraction ratio and exchange rate with irradiation radio frequency (RF) power dependent quantitative CEST MRI analysis. Contrast Media and Molecular Imaging. 2012;Accepted.
57. McVicar N, Li AX, Goncalves DF, Bellyou M, Meakin SO, Prado MA, Bartha R. Quantitative tissue pH measurement during cerebral ischemia using amine and amide concentration-independent detection (AACID) with MRI. Journal of Cerebral Blood Flow & Metabolism. 2014;34(4):690-8.
58. Albatany M, Li A, Meakin S, Bartha R. Dichloroacetate induced intracellular acidification in glioblastoma: in vivo detection using AACID-CEST MRI at 9.4 Tesla. Journal of neuro-oncology. 2018;136(2):255-62.
59. Marathe K, McVicar N, Li A, Bellyou M, Meakin S, Bartha R. Topiramate induces acute intracellular acidification in glioblastoma. Journal of neuro-oncology. 2016;130(3):465-72.
60. Liu G, Li Y, Sheth VR, Pagel MD. Imaging in vivo extracellular pH with a single paramagnetic chemical exchange saturation transfer magnetic resonance imaging contrast agent. Molecular imaging. 2012;11(1):7290.2011. 00026.

61. Longo DL, Sun PZ, Consolino L, Michelotti FC, Uggeri F, Aime S. A general MRI-CEST ratiometric approach for pH imaging: demonstration of in vivo pH mapping with iobitridol. Journal of the American Chemical Society. 2014;136(41):14333-6.
62. Chen LQ, Howison CM, Jeffery JJ, Robey IF, Kuo PH, Pagel MD. Evaluations of extracellular pH within in vivo tumors using acidoCEST MRI. Magnetic resonance in medicine. 2014;72(5):1408-17.
63. Javitt DC, Carter CS, Krystal JH, Kantrowitz JT, Girgis RR, Kegeles LS, Ragland JD, Maddock RJ, Lesh TA, Tanase C, Corlett PR, Rothman DL, Mason G, Qiu M, Robinson J, Potter WZ, Carlson M, Wall MM, Choo TH, Grinband J, Lieberman JA. Utility of Imaging-Based Biomarkers for Glutamate-Targeted Drug Development in Psychotic Disorders: A Randomized Clinical Trial. JAMA psychiatry. 2018;75(1):11-9. Epub 2017/11/24. doi: 10.1001/jamapsychiatry.2017.3572. PubMed PMID: 29167877; PubMed Central PMCID: PMCPmc5833531.
64. Andrabi SA, Kang HC, Haince JF, Lee YI, Zhang J, Chi Z, West AB, Koehler RC, Poirier GG, Dawson TM. Iduna protects the brain from glutamate excitotoxicity and stroke by interfering with poly (ADP-ribose) polymer-induced cell death. Nature Medicine. 2011;17(6):692-9.
65. Yu L, Wall BA, Wangari-Talbot J, Chen S. Metabotropic glutamate receptors in cancer. Neuropharmacology. 2017;115:193-202.
66. Huberfeld G, Vecht CJ. Seizures and gliomas [mdash] towards a single therapeutic approach. Nature Reviews Neurology. 2016;12(4):204-16.
67. Davis KA, Nanga RPR, Das S, Chen SH, Hadar PN, Pollard JR, Lucas TH, Shinohara RT, Litt B, Hariharan H. Glutamate imaging (GluCEST) lateralizes epileptic foci in nonlesional temporal lobe epilepsy. Science translational medicine. 2015;7(309):309ra161-309ra161.
68. Goryawala MZ, Sheriff S, Maudsley AA. Regional distributions of brain glutamate and glutamine in normal subjects. NMR in Biomedicine. 2016;29(8):1108-16.
69. Roalf DR, Nanga RPR, Rupert PE, Hariharan H, Quarmley M, Calkins ME, Dress E, Prabhakaran K, Elliott MA, Moberg PJ. Glutamate imaging (GluCEST) reveals lower brain GluCEST contrast in patients on the psychosis spectrum. Molecular psychiatry. 2017;22(9):1298.
70. Pépin J, Francelle L, Carrillo-de Sauvage M-A, de Longprez L, Gipchtein P, Cambon K, Valette J, Brouillet E, Flament J. In vivo imaging of brain glutamate defects in a knock-in mouse model of Huntington's disease. NeuroImage. 2016;139:53-64.
71. Dai Z, Zhang T, Yan G, Jia Y, Gen K, Xiao G, Zhang G, Shen Z, Wu R. Glutamate imaging. Contrast Media & Molecular Imaging. 2014;9(6):429.
72. Cai K, Tain R-W, Zhou XJ, Damen FC, Scotti AM, Hariharan H, Poptani H, Reddy R. Creatine CEST MRI for differentiating gliomas with different degrees of aggressiveness. Molecular Imaging and Biology. 2017;19(2):225-32.
73. Walker-Samuel S, Ramasawmy R, Torrealdea F, Rega M, Rajkumar V, Johnson SP, Richardson S, Gonçalves M, Parkes HG, Årstad E. In vivo imaging of glucose uptake and metabolism in tumors. Nature medicine. 2013;19(8):1067-72.
74. Ward K, Balaban R. Determination of pH using water protons and chemical exchange dependent saturation transfer (CEST). Magnetic Resonance in Medicine. 2000;44(5):799-802.
75. van Zijl PCM, Jones CK, Ren J, Malloy CR, Sherry AD. MRI detection of glycogen in vivo by using chemical exchange saturation transfer imaging (glycoCEST). Proceedings of the National Academy of Sciences. 2007;104(11):4359-64. doi: 10.1073/pnas.0700281104.
76. Zhang S, Trokowski R, Sherry AD. A paramagnetic CEST agent for imaging glucose by MRI. Journal of the American Chemical Society. 2003;125(50):15288-9.
77. Ling W, Regatte RR, Navon G, Jerschow A. Assessment of glycosaminoglycan concentration in vivo by chemical exchange-dependent saturation transfer (gagCEST). Proceedings of the National Academy of Sciences. 2008;105(7):2266-70. doi: 10.1073/pnas.0707666105.
78. Li Y, Sheth VR, Liu G, Pagel MD. A self-calibrating PARACEST MRI contrast agent that detects esterase enzyme activity. Contrast Media Mol Imaging. 2011;6(4):219-28. Epub 2011/08/24. doi: 10.1002/cmmi.421. PubMed PMID: 21861282; PubMed Central PMCID: PMCPmc4879975.
79. Gilad AA, McMahon MT, Walczak P, Winnard PT, Raman V, van Laarhoven HWM, Skoglund CM, Bulte JWM, van Zijl PCM. Artificial reporter gene providing MRI contrast based on proton exchange. Nature biotechnology. 2007;25(2):217-9. doi: 10.1038/nbt1277.
80. MB Wei ZS, G Xiao, QC Qiu, YW Chen, RH Wu. Imaging pH Phantoms Using Magnetization Transfer Technology

at 1.5 Tesla. The 4th International Conference on Biomedical Engineering and Informatics (BMEI)2011. p. 329-32.
81. Sun PZ, Cheung JS, Wang E, Lo EH. Association between pH-weighted endogenous amide proton chemical exchange saturation transfer MRI and tissue lactic acidosis during acute ischemic stroke. Journal of Cerebral Blood Flow & Metabolism. 2011.
82. Longo DL, Dastru W, Digilio G, Keupp J, Langereis S, Lanzardo S, Prestigio S, Steinbach O, Terreno E, Uggeri F, Aime S. Iopamidol as a Responsive MRI-Chemical Exchange Saturation Transfer Contrast Agent for pH Mapping of Kidneys: In Vivo Studies in Mice at 7 T. Magnetic Resonance in Medicine. 2011;65(1):202-11. doi: 10.1002/mrm.22608. PubMed PMID: WOS:000285963500023.
83. Opina ACL, Ghaghada KB, Zhao P, Kiefer G, Annapragada A, Sherry AD. TmDOTA-tetraglycinate encapsulated liposomes as pH-sensitive lipoCEST agents. PloS one. 2011;6(11):e27370.
84. Terreno E, Castelli DD, Viale A, Aime S. Challenges for molecular magnetic resonance imaging. Chem Rev. 2010;110(5):3019-42.
85. Sun PZ, Wang E, Cheung JS, Zhang X, Benner T, Sorensen AG. Simulation and optimization of pulsed radio frequency irradiation scheme for chemical exchange saturation transfer (CEST) MRI-demonstration of pH-weighted pulsed-amide proton CEST MRI in an animal model of acute cerebral ischemia. Magnetic Resonance in Medicine. 2011:n/a-n/a. doi: 10.1002/mrm.22894.
86. Wu R, Liu CM, Liu PK, Sun PZ. Improved measurement of labile proton concentration-weighted chemical exchange rate (kws) with experimental factor-compensated and T1-normalized quantitative chemical exchange saturation transfer (CEST) MRI. Contrast Media & Molecular Imaging. 2012;7(4):384-9.
87. Sun PZ, Wang Y, Xiao G, Wu R. Simultaneous experimental determination of labile proton fraction ratio and exchange rate with irradiation radio frequency power-dependent quantitative CEST MRI analysis. Contrast Media & Molecular Imaging. 2013;8(3):246-51.
88. Sun PZ, Lu J, Wu Y, Xiao G, Wu R. Evaluation of the dependence of CEST-EPI measurement on repetition time, RF irradiation duty cycle and imaging flip angle for enhanced pH sensitivity. Physics in Medicine and Biology. 2013;58(17):N229-N40. doi: 10.1088/0031-9155/58/17/n229.
89. Zhou J, Blakeley JO, Hua J, Kim M, Laterra J, Pomper MG, van Zijl PCM. Practical data acquisition method for human brain tumor amide proton transfer (APT) imaging. Magnetic Resonance in Medicine. 2008;60(4):842-9. doi: 10.1002/mrm.21712.
90. Shah T, Lu L, Dell KM, Pagel MD, Griswold MA, Flask CA. CEST-FISP: A novel technique for rapid chemical exchange saturation transfer MRI at 7 T. Magnetic Resonance in Medicine. 2011;65(2):432-7. doi: 10.1002/mrm.22637.
91. Jones CK, Polders D, Hua J, Zhu H, Hoogduin HJ, Zhou J, Luijten P, van Zijl PC. In vivo three-dimensional whole-brain pulsed steady-state chemical exchange saturation transfer at 7 T. Magn Reson Med. 2012;67(6):1579-89. Epub 2011/11/16. doi: 10.1002/mrm.23141. PubMed PMID: 22083645; PubMed Central PMCID: PMCPmc3291747.
92. Dixon WT, Hancu I, Ratnakar SJ, Sherry AD, Lenkinski RE, Alsop DC. A multislice gradient echo pulse sequence for CEST imaging. Magnetic Resonance in Medicine. 2009:NA-NA. doi: 10.1002/mrm.22193.
93. Sun PZ, Zhou J, Huang J, van Zijl P. Simplified quantitative description of amide proton transfer (APT) imaging during acute ischemia. Magnetic Resonance in Medicine. 2007;57(2):405-10. doi: 10.1002/mrm.21151.
94. Terreno E, Stancanello J, Longo D, Castelli DD, Milone L, Sanders HM, Kok MB, Uggeri F, Aime S. Methods for an improved detection of the MRI-CEST effect. Contrast Media Mol Imaging. 2009;4(5):237-47. Epub 2009/10/20. doi: 10.1002/cmmi.290. PubMed PMID: 19839029.
95. Singh A, Haris M, Cai K, Kassey VB, Kogan F, Reddy D, Hariharan H, Reddy R. Chemical exchange saturation transfer magnetic resonance imaging of human knee cartilage at 3 T and 7 T. Magn Reson Med. 2012;68(2):588-94. Epub 2012/01/04. doi: 10.1002/mrm.23250. PubMed PMID: 22213239; PubMed Central PMCID: PMCPmc4067761.
96. Dula AN, Asche EM, Landman BA, Welch EB, Pawate S, Sriram S, Gore JC, Smith SA. Development of chemical exchange saturation transfer at 7T. Magnetic Resonance in Medicine. 2011;66(3):831-8. doi: 10.1002/mrm.22862.
97. Sun PZ, Murata Y, Lu J, Wang X, Lo EH, Sorensen AG. Relaxation-compensated fast multislice amide proton transfer (APT) imaging of acute ischemic stroke. Magnetic Resonance in Medicine. 2008;59(5):1175-82. doi: 10.1002/mrm.21591.
98. Jokivarsi KT, Gröhn HI, Gröhn OH, Kauppinen RA. Proton transfer ratio, lactate, and intracellular pH in acute cerebral ischemia. Magnetic Resonance in Medicine. 2007;57(4):647-53. doi: 10.1002/mrm.21181.

99. Larson MK, Walker EF, Compton MT. Early signs, diagnosis and therapeutics of the prodromal phase of schizophrenia and related psychotic disorders. Expert review of neurotherapeutics. 2010;10(8):1347-59.
100. van der Gaag M, Smit F, Bechdolf A, French P, Linszen DH, Yung AR, McGorry P, Cuijpers P. Preventing a first episode of psychosis: meta-analysis of randomized controlled prevention trials of 12 month and longer-term follow-ups. Schizophrenia research. 2013;149(1):56-62.
101. Chan MK, Krebs M, Cox D, Guest P, Yolken R, Rahmoune H, Rothermundt M, Steiner J, Leweke F, Van Beveren N. Development of a blood-based molecular biomarker test for identification of schizophrenia before disease onset. Translational psychiatry. 2015;5(7):e601.
102. Fusar-Poli P, Carpenter W, Woods S, McGlashan T. Attenuated psychosis syndrome: ready for DSM-5.1? Annual review of clinical psychology. 2014;10:155-92.
103. Bagga P, Crescenzi R, Krishnamoorthy G, Verma G, Nanga RPR, Reddy D, Greenberg J, Detre JA, Hariharan H, Reddy R. Mapping the alterations in glutamate with GluCEST MRI in a mouse model of dopamine deficiency. Journal of Neurochemistry. 2016;139(3):432-9.
104. Haris M, Singh A, Mohammed I, Ittyerah R, Nath K, Nanga RPR, Debrosse C, Kogan F, Cai K, Poptani H. In vivo magnetic resonance imaging of tumor protease activity. Scientific reports. 2014;4:6081.
105. Merritt K, Egerton A, Kempton MJ, Taylor MJ, McGuire PK. Nature of Glutamate Alterations in Schizophrenia: A Meta-analysis of Proton Magnetic Resonance Spectroscopy Studies. JAMA psychiatry. 2016;73(7):665-74. Epub 2016/06/16. doi: 10.1001/jamapsychiatry.2016.0442. PubMed PMID: 27304221.
106. Howes O, McCutcheon R, Stone J. Glutamate and dopamine in schizophrenia: an update for the 21st century. Journal of psychopharmacology. 2015;29(2):97-115.
107. Xuan Y, Yan G, Peng H, Wu R, Xu H. Concurrent changes in 1H MRS metabolites and antioxidant enzymes in the brain of C57BL/6 mouse short-termly exposed to cuprizone: Possible implications for schizophrenia. Neurochemistry international. 2014;69:20-7.
108. Yan G, Xuan Y, Dai Z, Shen Z, Zhang G, Xu H, Wu R. Brain metabolite changes in subcortical regions after exposure to cuprizone for 6 weeks: potential implications for schizophrenia. Neurochemical research. 2015;40(1):49-58.
109. Yang ZX, Huo SS, Cheng XF, Xu ZF, Cao Z, Zeng JX, Xiao YY, You KZ, Chen W, Liu YY, Wu RH. Quantitative multivoxel proton MR spectroscopy study of brain metabolites in patients with amnestic mild cognitive impairment: a pilot study. Neuroradiology. 2011:1-8.
110. Zhang Z, Wang Y, Shen Z, Yang Z, Li L, Chen D, Yan G, Cheng X, Shen Y, Tang X, Hu W, Wu R. The Neurochemical and Microstructural Changes in the Brain of Systemic Lupus Erythematosus Patients: A Multimodal MRI Study. Scientific reports. 2016;6:19026.
111. Ametamey SM, Treyer V, Streffer J, Wyss MT, Schmidt M, Blagoev M, Hintermann S, Auberson Y, Gasparini F, Fischer UC. Human PET studies of metabotropic glutamate receptor subtype 5 with 11C-ABP688. Journal of Nuclear Medicine. 2007;48(2):247-52.
112. Xu H, Yang H-J, Zhang Y, Clough R, Browning R, Li X-M. Behavioral and neurobiological changes in C57BL/6 mice exposed to cuprizone. Behavioral neuroscience. 2009;123(2):418.
113. Xu H, Yang H, McConomy B, Browning RA, Li X-M. Behavioral and neurobiological changes in C57BL/6 mouse exposed to cuprizone: effects of antipsychotics. Frontiers in Behavioral Neuroscience. 2010;4:8.
114. Xu H, Yang H-J, Rose GM, Li X-M. Recovery of behavioral changes and compromised white matter in C57BL/6 mice exposed to cuprizone: effects of antipsychotic drugs. Frontiers in behavioral neuroscience. 2011;5:31.
115. Xu H, Yang H-J, Li X-M. Differential effects of antipsychotics on the development of rat oligodendrocyte precursor cells exposed to cuprizone. European archives of psychiatry and clinical neuroscience. 2014;264(2):121-9.
116. Ripke S, Neale BM, Corvin A, Walters JT, Farh K-H, Holmans PA, Lee P, Bulik-Sullivan B, Collier DA, Huang H. Biological insights from 108 schizophrenia-associated genetic loci. Nature. 2014;511(7510):421.
117. Kahn R, Sommer I. The neurobiology and treatment of first-episode schizophrenia. Molecular psychiatry. 2015;20(1):84.
118. Merritt K, McGuire P, Egerton A. Relationship between Glutamate Dysfunction and Symptoms and Cognitive Function in Psychosis. Frontiers in psychiatry. 2013;4:151. Epub 2013/12/11. doi: 10.3389/fpsyt.2013.00151. PubMed PMID: 24324444; PubMed Central PMCID: PMCPmc3840324.
119. De La Fuente-sandoval C, León-Ortiz P, Favila R, Stephano S, Mamo D, Ramírez-Bermúdez J, Graff-Guerrero A. Higher levels of glutamate in the associative-striatum of subjects with prodromal symptoms of schizophrenia and

patients with first-episode psychosis. Neuropsychopharmacology. 2011;36(9):1781.
120. Laskaris L, Di Biase M, Everall I, Chana G, Christopoulos A, Skafidas E, Cropley V, Pantelis C. Microglial activation and progressive brain changes in schizophrenia. British journal of pharmacology. 2016;173(4):666-80.
121. Lieberman J, Girgis R, Brucato G, Moore H, Provenzano F, Kegeles L, Javitt D, Kantrowitz J, Wall M, Corcoran C. Hippocampal dysfunction in the pathophysiology of schizophrenia: a selective review and hypothesis for early detection and intervention. Molecular psychiatry. 2018.
122. Bhojraj TS, Sweeney JA, Prasad KM, Eack SM, Francis AN, Miewald JM, Montrose DM, Keshavan MS. Gray matter loss in young relatives at risk for schizophrenia: relation with prodromal psychopathology. Neuroimage. 2011;54:S272-S9.
123. Yan G, Zhang T, Dai Z, Yi M, Jia Y, Nie T, Zhang H, Xiao G, Wu R. A Potential Magnetic Resonance Imaging Technique Based on Chemical Exchange Saturation Transfer for In Vivo γ-Aminobutyric Acid Imaging. PloS one. 2016;11(10):e0163765.
124. Kiernan MC, Vucic S, Cheah BC, Turner MR, Eisen A, Hardiman O, Burrell JR, Zoing MC. Amyotrophic lateral sclerosis. The Lancet. 2011;377(9769):942-55.
125. Peters OM, Ghasemi M, Brown RH. Emerging mechanisms of molecular pathology in ALS. The Journal of clinical investigation. 2015;125(5):1767-79.
126. McCampbell A, Cole T, Wegener AJ, Tomassy GS, Setnicka A, Farley BJ, Schoch KM, Hoye ML, Shabsovich M, Sun L. Antisense oligonucleotides extend survival and reverse decrement in muscle response in ALS models. Journal of Clinical Investigation. 2018;128(8):3558-67.
127. Scott A. Drug therapy: On the treatment trail for ALS. Nature. 2017;550(7676):S120-s1. Epub 2017/10/19. doi: 10.1038/550S120a. PubMed PMID: 29045376.
128. Ludolph A, Drory V, Hardiman O, Nakano I, Ravits J, Robberecht W, Shefner J. A revision of the El Escorial criteria-2015. Amyotroph Lateral Scler Frontotemporal Degener. 2015;16(5-6):291-2.
129. Menke RA, Agosta F, Grosskreutz J, Filippi M, Turner MR. Neuroimaging endpoints in amyotrophic lateral sclerosis. Neurotherapeutics. 2017;14(1):11-23.
130. Lokesh N, Seegerer A, Hioe J, Gschwind RM. Chemical Exchange Saturation Transfer in Chemical Reactions: A Mechanistic Tool for NMR Detection and Characterization of Transient Intermediates. Journal of the American Chemical Society. 2018;140(5):1855-62.
131. Liu G, Liang Y, Bar-Shir A, Chan KWY, Galpoththawela CS, Bernard SM, Tse T, Yadav NN, Walczak P, McMahon MT. Monitoring enzyme activity using a diamagnetic chemical exchange saturation transfer MRI contrast agent. Journal of the American Chemical Society. 2011.
132. Pyra T, Hui B, Hanstock C, Concha L, Wong JC, Beaulieu C, Johnston W, Kalra S. Combined structural and neurochemical evaluation of the corticospinal tract in amyotrophic lateral sclerosis. Amyotrophic Lateral Sclerosis. 2010;11(1-2):157-65.
133. Wong JC, Concha L, Beaulieu C, Johnston W, Allen PS, Kalra S. Spatial profiling of the corticospinal tract in amyotrophic lateral sclerosis using diffusion tensor imaging. Journal of Neuroimaging. 2007;17(3):234-40.
134. Wu R, Bruening R. Comparison of Diffusion-Weighted MR Imaging and T2-Weighted MR Imaging in Patients with Amyotrophic Lateral Sclerosis. The neuroradiology journal. 2006;19(6):705-10.
135. Cedarbaum JM, Stambler N, Malta E, Fuller C, Hilt D, Thurmond B, Nakanishi A, Group BAS, Group AclotBS. The ALSFRS-R: a revised ALS functional rating scale that incorporates assessments of respiratory function. Journal of the neurological sciences. 1999;169(1-2):13-21.
136. Togao O, Yoshiura T, Keupp J, Hiwatashi A, Yamashita K, Kikuchi K, Suzuki Y, Suzuki SO, Iwaki T, Hata N. Amide proton transfer imaging of adult diffuse gliomas: correlation with histopathological grades. Neuro-oncology. 2013;16(3):441-8.
137. Park JE, Kim HS, Park KJ, Kim SJ, Kim JH, Smith SA. Pre-and posttreatment glioma: comparison of amide proton transfer imaging with MR spectroscopy for biomarkers of tumor proliferation. Radiology. 2015;278(2):514-23.
138. Guégan C, Przedborski S. Programmed cell death in amyotrophic lateral sclerosis. The Journal of clinical investigation. 2003;111(2):153-61.
139. Szelechowski M, Amoedo N, Obre E, Léger C, Allard L, Bonneu M, Claverol S, Lacombe D, Oliet S, Chevallier S. Metabolic Reprogramming in Amyotrophic Lateral Sclerosis. Scientific reports. 2018;8(1):3953.
140. Chitnis T, Weiner HL. CNS inflammation and neurodegeneration. The Journal of clinical investigation. 2017;127(10):3577-87.
141. Ito Y, Ofengeim D, Najafov A, Das S, Saberi S, Li Y, Hitomi J, Zhu H, Chen H, Mayo L. RIPK1 mediates axonal

degeneration by promoting inflammation and necroptosis in ALS. Science. 2016;353(6299):603-8.
142. Lindberg MJ, Byström R, Boknäs N, Andersen PM, Oliveberg M. Systematically perturbed folding patterns of amyotrophic lateral sclerosis (ALS)-associated SOD1 mutants. Proceedings of the National Academy of Sciences of the United States of America. 2005;102(28):9754-9.
143. Danielsson J, Inomata K, Murayama S, Tochio H, Lang L, Shirakawa M, Oliveberg M. Pruning the ALS-associated protein SOD1 for in-cell NMR. Journal of the American Chemical Society. 2013;135(28):10266-9.
144. Zaiss M, Kunz P, Goerke S, Radbruch A, Bachert P. MR imaging of protein foldingin vitroemploying Nuclear-Overhauser-mediated saturation transfer. NMR in Biomedicine. 2013;26(12):1815-22. doi: 10.1002/nbm.3021.
145. Hughes J. Pathology of amyotrophic lateral sclerosis. Advances in neurology. 1982;36:61-74.
146. Zhang F, Chen G, He M, Dai J, Shang H, Gong Q, Jia Z. Altered white matter microarchitecture in amyotrophic lateral sclerosis: A voxel-based meta-analysis of diffusion tensor imaging. NeuroImage: Clinical. 2018;19:122-9.
147. Senda J, Ito M, Watanabe H, Atsuta N, Kawai Y, Katsuno M, Tanaka F, Naganawa S, Fukatsu H, Sobue G. Correlation between pyramidal tract degeneration and widespread white matter involvement in amyotrophic lateral sclerosis: a study with tractography and diffusion-tensor imaging. Amyotrophic Lateral Sclerosis. 2009;10(5-6):288-94.
148. Roccatagliata L, Bonzano L, Mancardi G, Canepa C, Caponnetto C. Detection of motor cortex thinning and corticospinal tract involvement by quantitative MRI in amyotrophic lateral sclerosis. Amyotrophic Lateral Sclerosis. 2009;10(1):47-52.
149. Wang S, Poptani H, Woo JH, Desiderio LM, Elman LB, McCluskey LF, Krejza J, Melhem ER. Amyotrophic lateral sclerosis: diffusion-tensor and chemical shift MR imaging at 3.0 T. Radiology. 2006;239(3):831-8.
150. Hecht M, Fellner F, Fellner C, Hilz M, Heuss D, Neundörfer B. MRI-FLAIR images of the head show corticospinal tract alterations in ALS patients more frequently than T2-, T1-and proton-density-weighted images. Journal of the neurological sciences. 2001;186(1):37-44.
151. Ji Y, Zhou IY, Qiu B, Sun PZ. Progress toward quantitative in vivo chemical exchange saturation transfer (CEST) MRI. Israel Journal of Chemistry. 2017.
152. Wu B, Warnock G, Zaiss M, Lin C, Chen M, Zhou Z, Mu L, Nanz D, Tuura R, Delso G. An overview of CEST MRI for non-MR physicists. EJNMMI physics. 2016;3(1):19.
153. Guo YL, Li SJ, Zhang ZP, Shen ZW, Zhang GS, Yan G, Wang YT, Rao HB, Zheng WB, Wu RH. Parameters of diffusional kurtosis imaging for the diagnosis of acute cerebral infarction in different brain regions. Experimental and therapeutic medicine. 2016;12(2):933-8. Epub 2016/07/23. doi: 10.3892/etm.2016.3390. PubMed PMID: 27446298; PubMed Central PMCID: PMCPmc4950828.
154. Guo YL, Zhang ZP, Zhang GS, Kong LM, Rao HB, Chen W, Wang GW, Shen ZW, Zheng WB, Wu RH. Evaluation of mean diffusion and kurtosis MRI mismatch in subacute ischemic stroke: Comparison with NIHSS score. Brain Res. 2016;1644:231-9. Epub 2016/05/22. doi: 10.1016/j.brainres.2016.05.020. PubMed PMID: 27208488.
155. Chen LQ, Pagel MD. Evaluating pH in the Extracellular Tumor Microenvironment Using CEST MRI and Other Imaging Methods. Advances in Radiology. 2015;2015.
156. Sun PZ, Xiao G, Zhou IY, Guo YK, Wu RH. A method for accurate pH mapping with chemical exchange saturation transfer (CEST) MRI. Contrast Media & Molecular Imaging. 2016;11(3):195-202. doi: 10.1002/cmmi.1680. PubMed PMID: WOS:000378426700003.
157. Gillies RJ, Raghunand N, Garcia-Martin ML, Gatenby RA. pH imaging. Engineering in Medicine and Biology Magazine, IEEE. 2004;23(5):57-64.
158. Dai Z, Jia Y, Yan G, Duan F, Xiao G, Shen Z, Sun H, Wilman AH, Wu R. pH-weighted imaging in diabetes mellitus suffering acute cerebral ischemic stroke. International Society of Magnetic Resonance in Medicine 23rd Annual Meeting. 2015.
159. Shambesh MKA, Emahbes TM, Kama F, Saleh Z, Shambesh IM. Diabetes Mellitus and Cerebrovascular Accident among North African Population (Libya) Community Based Survey. International Journal of TROPICAL DISEASE & Health. 2015;10(2):1-9.
160. Tziomalos K, Spanou M, Bouziana SD, Papadopoulou M, Giampatzis V, Kostaki S, Dourliou V, Tsopozidi M, Savopoulos C, Hatzitolios AI. Type 2 diabetes is associated with a worse functional outcome of ischemic stroke. World journal of diabetes. 2014;5(6):939.
161. McMahon MT, Gilad AA, Zhou J, Sun PZ, Bulte JWM, van Zijl PCM. Quantifying exchange rates in chemical exchange saturation transfer agents using the saturation time and saturation power dependencies of the

magnetization transfer effect on the magnetic resonance imaging signal (QUEST and QUESP): Ph calibration for poly-L-lysine and a starburst dendrimer. Magnetic Resonance in Medicine. 2006;55(4):836-47. doi: 10.1002/mrm.20818.